Acoustic Phonon Transport at Nanostructured Interfaces

by

Huarui Sun

A dissertation submitted in partial fulfillment
of the requirements for the degree of
Doctor of Philosophy
(Mechanical Engineering)
in the University of Michigan
2013

Doctoral Committee:

Associate Professor Kevin P. Pipe, Chair
Professor Roy Clarke
Professor Karl Grosh
Professor Katsuo Kurabayashi

Acknowledgements

First and foremost, I am deeply grateful to my advisor Prof. Kevin Pipe, who has been helpful and supportive throughout my PhD. He constantly offers me sparkling research ideas; his intelligence and creativity often inspire me to examine problems from different angles. He has let me know the importance of getting out of little cubes filled with detailed challenging tasks and instead focusing on macroscopic pictures of greater significance and issues with higher priorities.

At UM I am fortunate enough to learn from many other great minds. Prof. Max Shtein has offered me generous advice and support. I have been impressed and influenced by his unique way of presenting ideas and results, like telling an intriguing story about science and nature. I appreciate Prof. Roy Clarke's helpful discussions in our collaborative work. I am also thankful to Prof. Karl Grosh and Prof. Katsuo Kurabayashi for serving on my committee and sharing their advice on my dissertation work.

Collaborations have been a dispensable part in my research, during which I received lots of help. Dr. Vladimir Stoica has offered me invaluable assistance on building the pump-probe experimental setup and trouble-shooting the ultrafast lasers. I spent numerous hours in the Randall basement taking data and discussing projects with him. Yuwei Li taught me how to create nanotracks with femtosecond laser irradiation. Yansha Jin shared her TEM and SEM images, as well as her inspiring results of thermal conductivity measurement. I would also like to thank Justin Canniff and Dr. Adam Wood for providing FIB irradiated samples for pump-probe measurements.

My labmates have been a valuable source of ideas and inspirations. I have enjoyed working together with Si Hui, Gunho Kim, Vahid Rashidi, Lei Shao, and Kejia Zhang. From their individual projects, I have learned different things and gained novel perspectives. Many people offered hands when I prepared samples in Prof. Max Shtein's lab and calibrated materials in Prof. Peter Green's lab. My thanks go to Steven Morris, Matt Sykes, Anton Li, Kanika Agrawal, Shaurjo Biswas, Mark Hendyx, and Adam Barito.

There are people who I interacted with before they left Michigan for new positions that I must acknowledge. Dr. Abhishek Yadav has been one of my best friends since I joined the lab. His breadth of knowledge and sense of humor made my stay in the lab more enjoyable and fruitful. Dr. Kwang Hyup An trained me on several instruments and I was impressed by his competency and efficiency in both experimental and theoretical work. I also want to thank Dr. Brendan O'Connor, Dr. Yiying Zhao, Dr. Jingjing Li, and Dr. Paddy Chan; although I did not have much overlap with them during their stay, I learned a great deal from them including experimental techniques and presentation skills.

PhD study is a long and sometimes frustrating process; without constant support from my family, I cannot imagine going through this all by myself. I am very lucky to have made many good friends during my stay in Ann Arbor. My special thanks go to Chinese Volleyball Club, in which I had tremendous fun playing volleyball with friends. I feel deeply blessed to have met my girlfriend Yang Lin, who has always been supportive and encouraging in my pursuit of PhD and career decisions. I thank her for bringing me countless beautiful moments and I look forward to sharing with her more exciting and wonderful days ahead.

Table of Contents

List of Figures

List of Tables

Abstract

Transport of acoustic phonons plays an important role in a number of applications, such as thermal management, terahertz phononic filters, and high-frequency mechanical resonators. At the nanoscale, interfaces affect acoustic transport through boundary scattering. The overall aim of this work is to understand how acoustic phonons interact with nanostructured interfaces.

We adopt an optical means based on ultrafast lasers to characterize dynamics of phonon (and thermal) transport through interfaces. We examine heat transfer properties of several semiconductor nanostructures using time-domain thermoreflectance and show that forming nanocrystals or nanochannels on the surface reduces the heat conduction rate because of enhanced phonon boundary scattering.

Confined acoustic phonon modes may occur in an acoustically isolated medium that is enabled by high acoustic impedance mismatch at the boundaries. We insert a compliant organic (CuPc) film at the Al/Si interface to form a supported membrane resonator. We use femtosecond laser pulses to excite multiple GHz coherent phonon modes in such a cavity. The interfacial CuPc film acts as an acoustic etalon to select certain modes out of the broadband excitation, according to its Fabry-Perot resonances. Our observations have scientific significance in understanding coherent acoustic phonon transport, and support future studies of manipulating high-frequency acoustic energy in nanostructures.

Interface irregularities such as roughness affect transport of acoustic phonons due to their short wavelengths. We develop a theoretical model based on perturbation analysis to calculate the specular and quasi-diffuse fields produced by scattering. We evaluate the effect of interface roughness on phonon mode conversion, scattered field distribution, and interface wave generation. We then estimate the performance of a coherent phonon reflector with roughened interfaces. Our findings have novel implications for the design of phononic devices; in addition, our preliminary experimental results confirm the reduction in coherent phonon reflection at roughened interfaces.

Chapter 1

Background

At temperatures above 0 K, atoms vibrate about their equilibrium positions and interact with each other through interatomic forces. These vibrations can propagate and transfer energy in the system through lattice waves. Sound at audible frequencies is carried in solids by lattice waves with relatively long wavelengths, while heat is conducted in dielectric and semiconducting solids near room temperature primarily by lattice waves with relatively short wavelengths (high frequencies). Quantum mechanical theories tell us that lattice wave energies occur at discrete levels. The term "phonon" refers to the minimum allowed energy of a quantized lattice wave.

Study of acoustic phonon transport in nanostructures and at interfaces is of fundamental interest and importance to a number of devices and applications (Chapter 1), such as nanoscale heat transfer, terahertz phononic filters and reflectors, high frequency acoustic resonators, and acoustic modulators. In this dissertation we focus on the fundamental understanding of acoustic phonon transport at interfaces, including characterization of thermal transport at nanostructured interfaces (Chapter 2), coherent control of confined acoustic phonon modes in nanostructures with interfaces between highly dissimilar materials (Chapter 3), theoretical modeling of acoustic phonon

scattering at roughened interfaces and multilayers (Chapter 4), and preliminary measurement of acoustic phonon reflection at roughened interfaces (Chapter 5).

1.1 Phonons in heat transfer

Heat transfer results from the random motion of "particles" that carry thermal energy from one place to another. These energy carriers ("particles") include electrons, atoms, and molecules in gases, liquids, and solids. In metals, the primary heat carriers are free electrons that conduct electricity as well; in dielectric solids which are electrically insulating, heat is conducted through atomic vibrations, i.e., the propagation of phonons. The discussion in this dissertation will be limited to dielectric solids wherein heat is primarily carried by acoustic phonons.

Heat is carried by phonons across a wide range of frequencies. The spectral content of phonon wave packets in solids is determined largely by the temperature. The analogy can be made to blackbody radiation; Figure 1-1 schematically illustrates Planck's distribution for phonons at different temperatures.

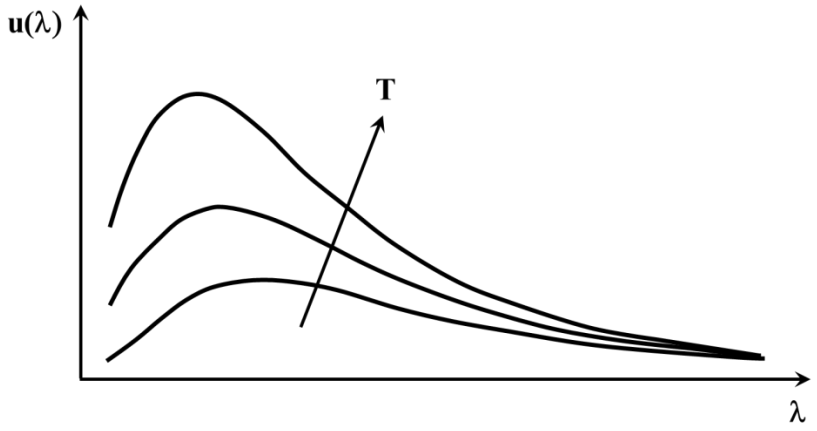

Figure 1-1 Schematic diagram of spectral emissive power u(λ) of phonons.

The dominant phonon wavelength relevant for heat transfer scales inversely with temperature [1]:

$$\lambda_{dom} \sim h v_g / k_B T \tag{1.1}$$

where h is Planck's constant, v_g is the phonon group velocity that is material dependent, k_B is the Boltzmann constant, and T is the temperature. The dominant phonon frequency is $f_{dom} = 4.25(k_B/h)T \sim (90\ \text{GHz}\cdot\text{K}^{-1})T$. As one example, the dominant phonon wavelength in silicon is ~ 0.3 nm at 300 K and ~ 1μm at 0.1 K. Meanwhile, the phonon mean free path in Si at room temperature is debated, with reported values ranging from 40 nm to a few microns [2] according to various experiments and theories. These numbers have engineering implications as the size of devices shrinks to the submicron or nanometer scale. For example, when the structure dimension becomes comparable to the phonon wavelength, modified phonon dispersion may occur and interface scattering may dominate phonon transport.

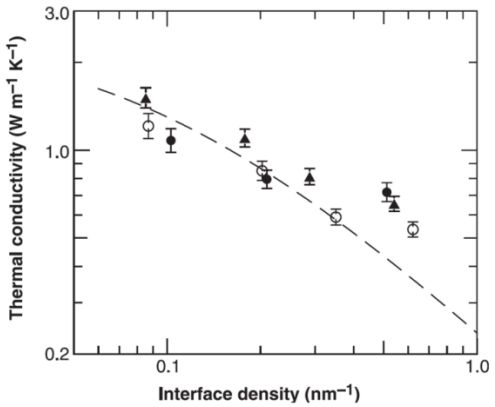

Figure 1-2 Room temperature thermal conductivity of W/Al_2O_3 thin film multilayers with different interface densities (inverse of interface spacing) fabricated by atomic layer deposition (ALD) at 300 ˚C (solid circles), 177 ˚C (open circles), and by magnetron sputtering (solid triangles). The dashed line is a fit with a thermal boundary conductance of 260 MW/m^2-K [3].

The control of phonon transport has potential for precise tuning of thermal conductivity at the nanoscale, which is fundamentally critical for heat management in micro- and nano-electronics as well as thermoelectric energy conversion. Engineered nanostructures and complex compound materials have been extensively developed to manipulate thermal transport by means of adding guest atoms or introducing phonon interface scattering. For example, Ref. 3 suggests that high interface density may introduce a significant amount of acoustic phonon scattering, strongly impeding heat transfer in thin film multilayers (Figure 1-2). Ref. 4 has reported an ultralow thermal conductivity of crystal WSe_2 thin films which is attributed to localized lattice vibrations in the disordered layered structure. Ref. 5 has demonstrated the precise control of thermal conductivity in single-crystalline SiGe through the introduction of phonon-scattering barriers (Figure 1-3).

The above-mentioned experimental observations of heat transfer in layered structures fall into the classical size regime, in which phonon transport is considered ballistic or quasi-ballistic and phonons lose their phase information through diffuse scattering at interfaces within the structure. However, recent findings [6] suggest potential control of heat transfer by engineering phonon coherence in solids. Figure 1-4 shows that the measured thermal conductivity scales linearly with the number of periods in AlAs/GaAs superlattices over a temperature range of ~ 120 K, which is predicted by coherent phonon heat transfer. In this regime, phonon phase is preserved during interface scattering in the superlattice and wave interference effects modify the dispersion, giving rise to phonon mean free paths as long as the sample length [7]. Inspired by the ideas of coherent wave thermal transport, Ref. 8 proposed a novel approach for thermal

management in crystals in which heat is guided in a manner similar to how photonic crystals guide light and phononic crystals guide sound. Figure 1-5 demonstrates a series of rationally designed conceptual devices for thermal energy management and manipulation.

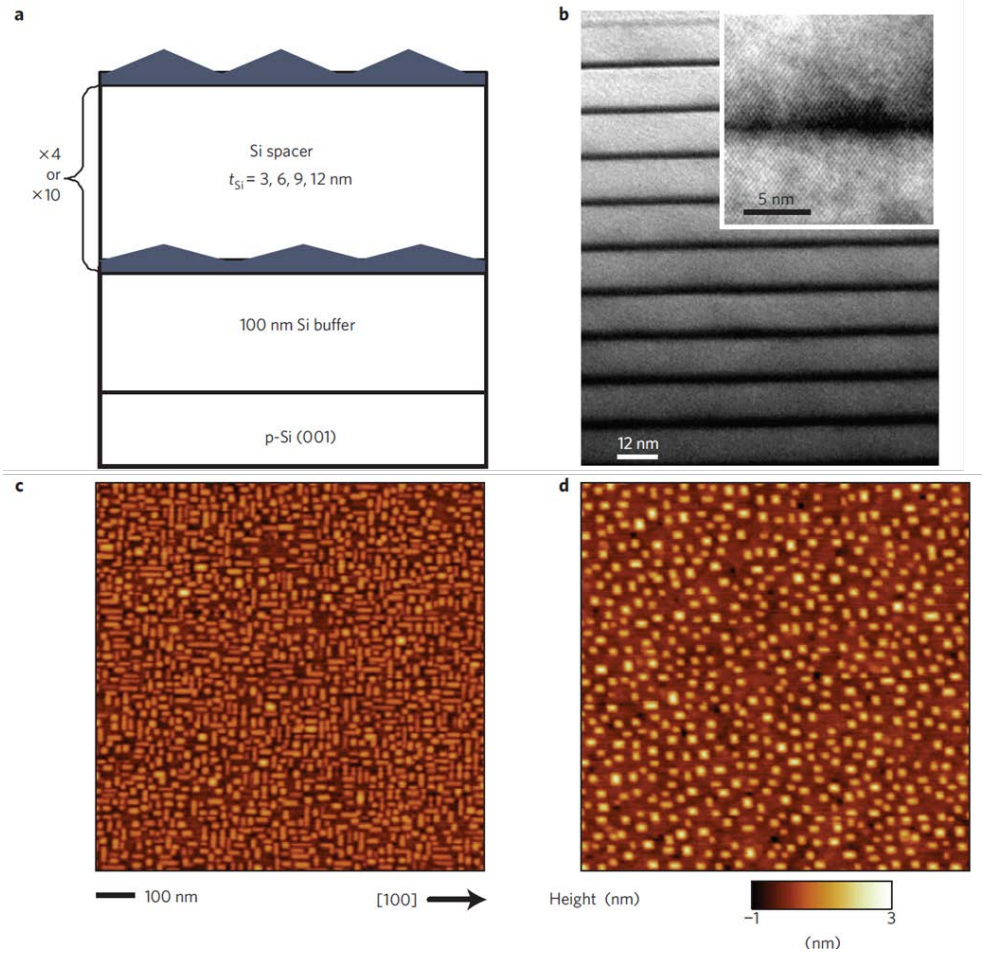

Figure 1-3 (a) Schematic of a self-assembled nanodot multilayer grown by molecular beam epitaxy (MBE). (b) Bright-field transmission electron microscopy (TEM) image of a sample with alternating Si (12 nm) and Ge layers (dark regions). The inset shows a high-resolution TEM image of a nanodot. (c) Atomic force microscopy (AFM) image of a single Ge/Si dot layer. (d) AFM image of the topmost layer [5].

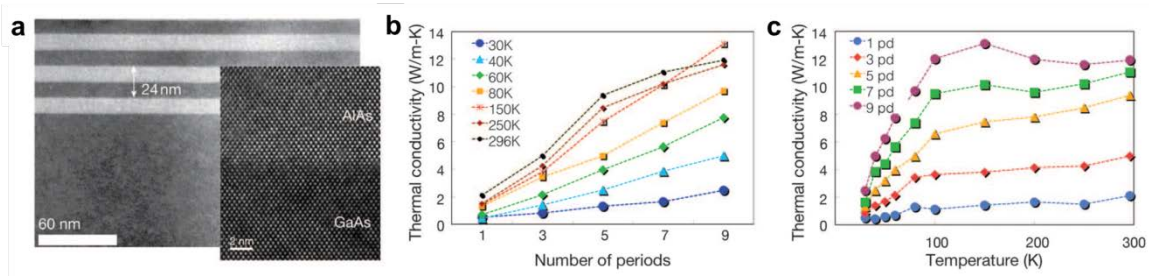

Figure 1-4 (a) Cross-sectional TEM image of a 3-period AlAs/GaAs superlattice. Inset is a high-resolution TEM image of one single interface. (b) Measured thermal conductivity of AlAs/GaAs superlattices as a function of number of periods at different tempeartures. (c) Measured thermal conductivity of AlAs/GaAs superlattices as a function of temperature with different numbers of periods [6].

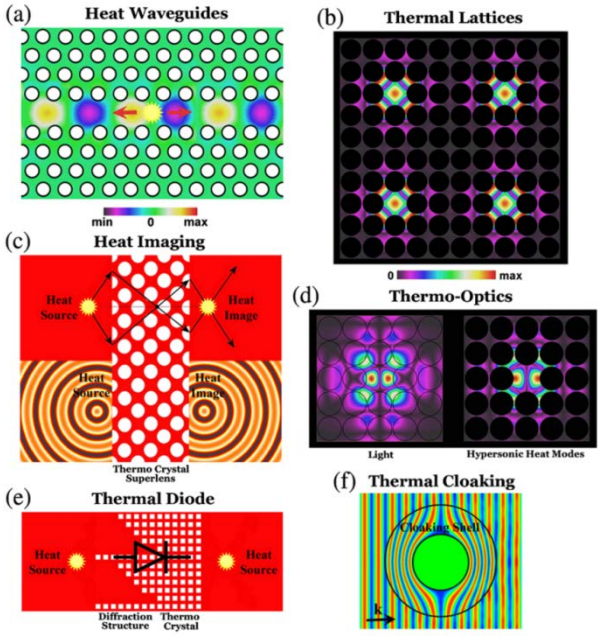

Figure 1-5 Schematics of designed thermocrystal devices and applications: (a) heat waveguides, (b) thermal lattices, (c) heat imaging, (d) thermo-optics, (e) thermal diodes, (f) thermal cloaking [8].

In addition to the potential roles of coherent phonons in thermal transport, they provide a convenient experimental tool to study heat transfer. By examining how phonons of a particular wavelength transfer energy and interact with various types of interfaces, we can predict how phonons at other wavelengths (e.g., the broad spectrum of

phonons that carry heat) likewise interact with an interface. The study of coherent phonon transport therefore affords fundamental understanding of both heat transfer and coherent acoustic applications such as phonon reflectors and acoustic resonators.

1.2 Coherent phonon reflectors

As seen in the examples in Section 1.1, with the advance of thin film techniques, near-perfect crystalline multilayer structures (e.g., superlattices) can be fabricated to achieve tuning of electronic quantum states and photon and phonon transport, to yield further control of electrical, optical, and thermal properties. A typical acoustic phonon Bragg reflector consists of repeated periods of alternating layers with different acoustic impedances. The condition for Bragg reflection requires $m\lambda = 2(d_1 + d_2)\cos\theta$, where λ is the phonon wavelength (material dependent), d_1 and d_2 are the respective thicknesses of the two materials, θ is the phonon incident angle, and m is an integer. By carefully choosing the thicknesses of each material, such superlattices can reflect or transmit certain frequencies of acoustic phonons as a result of coherent Bragg scattering. Numerous theoretical simulations and experimental measurements [7,9-13] have been conducted to demonstrate the dips or the so-called "stop bands" in frequency-dependent phonon transmission.

Early experimental explorations of phonon Bragg reflectors have used MBE-grown lattice-matched crystalline material pairs such as GaAs/AlGaAs [9] and InGaAs/AlAs [10], as well as amorphous superlattices such as vacuum-evaporated Si/SiO_2 [11] and chemical vapor deposited a-Si:H/a-SiN_x:H [11,12]. Superconducting tunnel junctions have been used to generate and detect high-frequency acoustic phonons

[9-12]. The development of ultrafast lasers offers a more convenient way to excite and monitor phonon transmission and reflection [13,14]. In this "pump-probe" technique, one "pump" laser pulse is used to generate coherent phonons and one "probe" laser pulse that is time-delayed with respect to the pump pulse is used to detect coherent phonons. Details of the pump-probe approach are discussed in Chapters 2 and 3. Figure 1-6 shows a recent experimental demonstration of GaAs/AlAs superlattices optimized for broadband phonon mirrors and acoustic "color filters" [13].

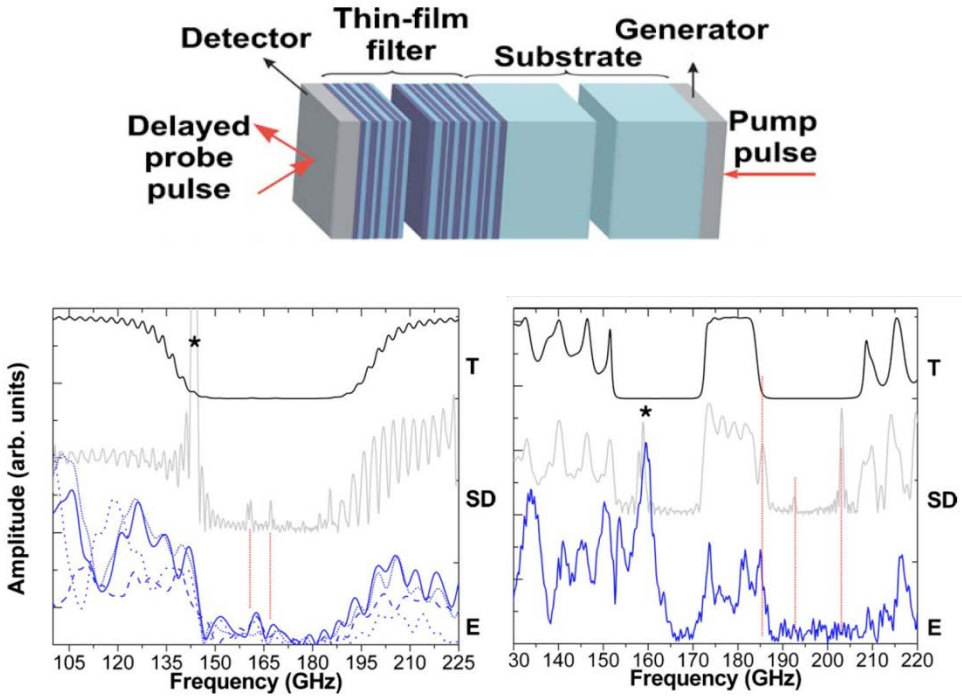

Figure 1-6 (top) Schematic diagram of a GaAs/AlAs phononic thin film filter. Acoustic phonon transmission through (bottom left) a broadband phonon mirror and (bottom right) an optimized acoustic "color filter" [13].

The propagation of acoustic phonon waves in a Bragg reflector can be modeled using elastic continuum theory and a plane wave approximation, which are discussed in Section 1.4.

1.3 Acoustic resonators

The study of acoustic phonons has attracted a great deal of attention on account of its applications in mechanical/acoustic resonators used by radio-frequency (RF) filters, gas sensors, microwave oscillators, power amplifiers, etc. Micro and nanoscale thin film structures are increasingly used to meet the increasing demand by applications of high frequency acoustic resonators. Such devices include thin film bulk acoustic resonators (FBARs) and surface acoustic wave (SAW) resonators (we will not discuss SAW resonators in this dissertation). FBARs usually consist of a piezoelectric layer sandwiched between two electrodes and acoustically isolated from the surroundings. Acoustic isolation is achieved by enclosing the piezoelectric film with end acoustic reflectors that resemble the structures presented in Section 1.2.

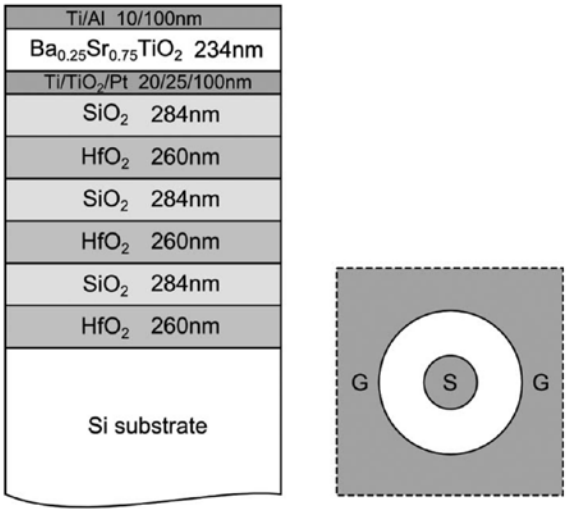

Figure 1-7 Schematics of a tunable bulk acoustic wave (BAW) resonator. (left) Cross-sectional view and (right) top view of electrodes [15].

Figure 1-7 shows schematic views of a bulk acoustic wave resonator based on a $Ba_xSr_{1-x}TiO_2$ thin film and an HfO_2/SiO_2 Bragg reflector [15]. The paraelectric-phase $Ba_xSr_{1-x}TiO_2$ film has a field-dependent piezoelectric coefficient that results in tunable

resonances with varied bias. The all-dielectric HfO_2/SiO_2 Bragg reflector design eliminates the parasitic capacitance issue that exists in metal-containing acoustic reflectors. In addition to solidly-mounted systems, suspended thin film membranes (Figure 1-8) have applications in FBARs due to their extremely high quality factors (Q) [16]. These FBARs in general have a frequency response up to ~ 10 GHz.

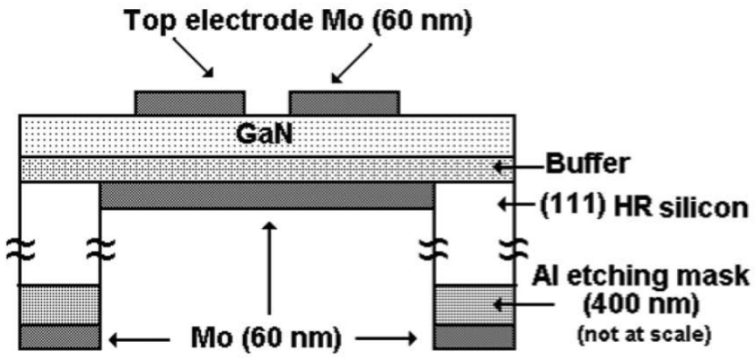

Figure 1-8 Schematic cross section of the thin GaN membrane based FBAR [16].

1.4 Mathematical descriptions of acoustic phonons

1.4.1 Plane wave approximation

The wave nature of acoustic phonons is of critical importance to transport that occurs in nanostructures and at interfaces. Phase information is a fundamental property of phonon waves; the fixed phase relationship in a coherent phonon wave results in interference and diffraction patterns that are familiar from optics.

In the long wavelength range, a condensed medium can be treated as a continuum and thus phonons can be treated as plane waves. The 1D wave equation for a plane acoustic wave propagating in the *z* direction in an isotropic solid is simply:

$$\rho \frac{\partial^2 u}{\partial t^2} = \frac{\partial \sigma}{\partial z} \tag{1.2}$$

where $u(z,t)$ is the displacement, $\sigma = C(\partial u/\partial z)$ is the stress, and C is the component of the elastic tensor in the z direction. The solution of the displacement along the z direction is then:

$$u(z,t) = \left(ae^{ikz} + be^{-ikz}\right)e^{i\omega t} \tag{1.3}$$

where a and b are the amplitudes of the -z and +z traveling waves, respectively, and ω is the angular frequency. A generalized vector representation in space, analogous to an electromagnetic wave, is

$$\mathbf{u}(\mathbf{r},t) = \mathbf{u_0}e^{i(\omega t - \mathbf{k}\cdot\mathbf{r})} \tag{1.4}$$

1.4.2 Reflection and transmission at interfaces

Like other classical waves, phonons are scattered at interfaces between two dissimilar materials. The reflection and transmission of acoustic waves can be treated in a manner similar to electromagnetic waves, except that the boundary conditions are based on continuities of both displacement (or displacement velocity) and stress at the interface ($z = z_0$):

$$\begin{cases} \mathbf{u}_1\big|_{z=z_0} = \mathbf{u}_2\big|_{z=z_0} \\ \boldsymbol{\sigma}_1\big|_{z=z_0} = \boldsymbol{\sigma}_2\big|_{z=z_0} \end{cases} \tag{1.5}$$

While continuity of stress is always required, continuity of displacement may not always stand, even in a lattice dynamics simulation. This means that atoms on the two sides of an

interface may have different displacements. Nevertheless, in the long wavelength limit, the continuum theory is a reasonable assumption, and thus Equation (1.5) is used in several calculations throughout the dissertation. In Chapter 5 we discuss the possible breakdown of the continuum assumption according to experimental observations.

As acoustic phonon waves have three different polarizations (modes), the derivation of expressions for reflection and transmission at interfaces is significantly more complex than that for electromagnetic waves. Detailed boundary conditions and mathematical derivations can be found in several classic references [17,18]. Here we only give the results of the simplest case, in which a horizontally polarized transverse wave (shear horizontal (SH) wave; see Chapter 4 for details) is incident on an interface between two isotropic solids. With no mode conversion, the output field only contains one reflected SH wave and one transmitted SH wave, and the reflection and transmission coefficients are:

$$\begin{cases} r_{SH} = \dfrac{Z_1 \cos\theta_i - Z_2 \cos\theta_t}{Z_1 \cos\theta_i + Z_2 \cos\theta_t} \\ t_{SH} = \dfrac{2Z_1 \cos\theta_i}{Z_1 \cos\theta_i + Z_2 \cos\theta_t} \end{cases} \tag{1.6}$$

where $Z = \rho v_{SH}$ is the acoustic impedance for the SH mode and v_{SH} is the transverse acoustic velocity. Z is analogous to the refractive index in optics. The incident angle θ_i and transmitted angle θ_t are linked by the acoustic Snell law that holds for all three modes:

$$\frac{\sin\theta_i}{v_1} = \frac{\sin\theta_t}{v_2} \tag{1.7}$$

The acoustic Poynting vector is used to derive the (power) reflectivity and transmissivity:

$$\begin{cases} R_{SH} = \left|r_{SH}\right|^2 \\ T_{SH} = \dfrac{Z_2}{Z_1}\dfrac{\mathrm{Re}\left(\cos\theta_t\right)}{\cos\theta_i}\left|t_{SH}\right|^2 \end{cases} \tag{1.8}$$

The real part of $\cos\theta_t$ is used in cases for which total internal reflection occurs ($v_2 > v_1$ could lead to $\sin\theta_t > 1$). The reflection and transmission coefficients for longitudinally (L) and vertically polarized transverse (shear vertical (SV)) waves in general need to be solved through matrix calculations and do not have simple explicit forms. Chapter 4 gives a more comprehensive discussion of these modes and their interconversions at interfaces, as well as acoustic evanescent waves and interface modes.

The reflection of acoustic phonon waves at an interface gives rise to a thermal resistance to heat flow; this thermal boundary resistance (TBR) can be calculated through the integration of acoustic transimissivity over incident angle and frequency given the proper phonon population distribution.

The above calculations are based on the acoustic mismatch model (AMM), which assumes fully elastic phonon transport and accurately captures heat transfer across smooth interfaces at low temperatures [19,20]. The diffuse mismatch model (DMM), on the other hand, assumes entirely diffusive phonon scattering at the interface and applies to rough boundaries at elevated temperatures [19,20]. Neither of these two primary models can be considered universally precise, but rather they serve as upper and lower limits for TBR. Measurement techniques for TBR and will be introduced in Chapter 2.

1.4.3 Wave propagation in thin films

Stacked thin films are the most common structures in numerous energy conversion devices, as shown in Sections 1.1-1.3. Multiple reflections and transmissions of phonon waves caused by the interfaces within these systems can result in interference effects. The thickness-dependent reflectivity and transmissivity are then modeled using a transfer matrix method. We again take the simplest SH wave propagation as an example. The transfer matrix for a wave incident at the interface from solid 1 is:

$$T_{\text{int},1\to 2} = \frac{1}{t_{1\to 2}} \begin{bmatrix} 1 & r_{1\to 2} \\ r_{1\to 2} & 1 \end{bmatrix} \tag{1.9}$$

The transfer matrix for wave propagation within film 1 is given by:

$$T_{prop,1} = \begin{bmatrix} e^{-jk_1 d_1} & 0 \\ 0 & e^{jk_1 d_1} \end{bmatrix} \tag{1.10}$$

The phonon wave amplitudes (a and b) in Equation (1.3) can then be obtained at any position inside the multilayer. The transfer matrix calculation is a powerful tool in deriving the dispersion relation and the reflection/transmission spectra of phonon waves. As an example, Figure 1-9 illustrates the schematics of a typical phonon Bragg reflector and its band-like reflection spectra [14].

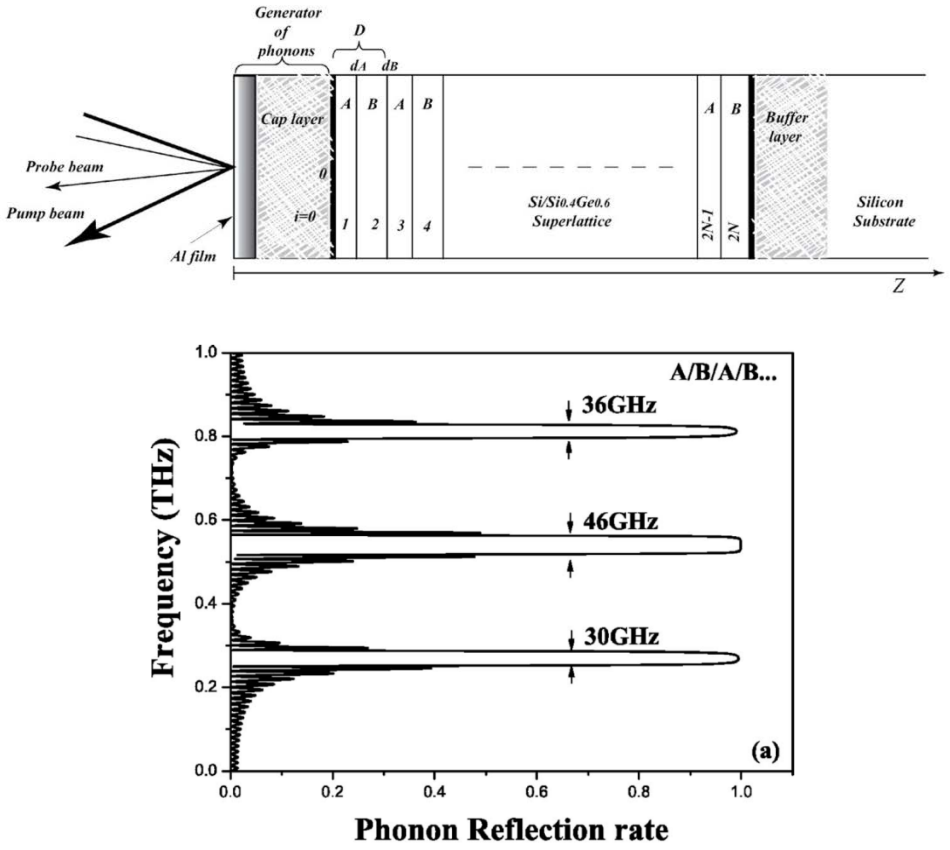

Figure 1-9 (top) Schematic diagram of an $(A/B)_N$ superlattice phonon reflector. (bottom) Calculated phonon reflection rate for the structure [14].

1.5 Overview of work

In the following chapters, we address several fundamental problems involved in acoustic phonon transport closely related to what has been discussed in Sections 1.1-1.3. In Chapter 2 we introduce measurement techniques used for characterizing acoustic phonon transport and heat transfer at interfaces: picosecond acoustics and time domain thermoreflectance (TDTR). We discuss the experimental system (optical pump-probe techniques based on ultrafast lasers) and the mathematical models for extracting phonon and thermal transport properties from measured data. We then present measured thermal conductivities of several nanostructures, including copper phthalocyanine (CuPc) thin

films, FIB-irradiated GaAs:N nanocrystals, and Sb_2Te_3 nanostructures formed by laser irradiation.

In Chapter 3 we focus on the experimental characterization of long-wavelength (tens or hundreds of nanometers) acoustic phonon waves. We construct a supported membrane resonator by inserting a compliant CuPc film at an Al/Si interface. The high acoustic impedance mismatch at organic/inorganic interfaces helps to form an acoustic cavity in which multiple GHz modes are excited by ultrafast lasers. We demonstrate that the interfacial CuPc film acts as an acoustic etalon to select certain modes out of the broadband excitation. These observations have scientific implications for coherent wave heat conduction (Section 1.1), phonon Bragg reflectors (Section 1.2), and acoustic resonators (Section 1.3).

Acoustic phonon transport at interfaces is neither entirely elastic nor completely diffusive (Section 1.4.2); rather, it is a combination. In Chapter 4 we develop a boundary perturbation approach to separate the specular and quasi-diffuse components from interface acoustic scattering. We calculate the effect of interface roughness on phonon mode conversion, scattered field distribution, and interface wave generation. We further examine coherent phonon transport in Bragg reflectors with roughened interfaces, which have technological implications for practical phononic or acoustic devices.

In Chapter 5 we present the results of measured phonon reflection at roughened interfaces that are created through chemical etching. These observations provide experimental validation for models of acoustic phonon scattering at rough interfaces. We also discuss the effect of interface stiffness on coherent phonon transport.

In Chapter 6 we summarize the present work and show preliminary results of coherent control of acoustic phonon modes in double bi-layer systems. With future endeavors, we should be able to achieve better control of these modes by carefully designing the multi-stack resonator/etalon structure. We also present preliminary results of calculated phonon reflection in a Bragg mirror with varied interface stiffness. We discuss methods to experimentally confirm these findings by performing picosecond acoustics on superlattices with van der Waals bonded interfaces (e.g., metal/organic interfaces). In addition, due to the high acoustic impedance contrast, these metal/organic multilayers are expected to have ultralow thermal conductivity.

Chapter 2

Pump-probe characterization of phonon and thermal transport

Characterization of thermal and mechanical properties of nanoscale thin films becomes increasingly important as microelectronic devices made from thin films suffer in performance from elevated temperatures or high stress. For thin films with a thickness of 100 nm, the time scales for elastic wave propagation and heat transfer depend on the specific material but are in the approximate ranges of 10 – 100 ps and 0.1 – 10 ns, respectively. Therefore, ultra high speed instrumentation is needed in order to monitor the dynamics of acoustic and thermal transport in nanostructures.

2.1 Introduction

As mentioned in Chapter 1, ultrafast laser systems can be used to generate and detect acoustic phonons with frequencies up to 200 GHz as well as thermal waves with penetration depths of a few nanometers. The short duration of the laser pulses (on the order of 100 fs) makes them ideal to monitor the acoustic and thermal properties of thin films and their interfaces. Over the past two decades, picosecond acoustics and time domain thermoreflectance (TDTR) based on the optical pump-probe technique have evolved from theory to a fully validated experimental approach that is currently a common tool for process control in semiconductor manufacturing.

The process of generating coherent acoustic phonons with a laser pulse can be summarized as follows: the laser beam (pump) is focused on an acoustic transducer (usually a metal film), and the pulse energy is absorbed within the optical penetration depth (on the order of 10 nm for most metals), creating a localized temperature rise ΔT of several degrees Kelvin in the lattice and a change in reflectivity ΔR that is proportional to ΔT (the basis of thermoreflectance). The transducer film cools down through heat diffusion into the underlying structure, resulting in a transient $\Delta R(t)$.

In addition to the thermal diffusion, the localized thermal stress launches an acoustic strain pulse that propagates into the transducer film, with a dominant wavelength on the order of tens of nanometers. When the strain pulse meets an interface, part of the energy gets transmitted while part gets reflected based on the acoustic impedance contrast of the two materials. The reflected pulse returns to the surface of the transducer and modulates the refractive index, inducing an additional change in the optical reflectivity.

The overall $\Delta R(t)$ can be detected by a probe laser pulse that is delayed with respect to the pump laser pulse. By varying the delay time through a mechanical translation stage or other techniques (which will be discussed in Section 2.2), a time-resolved pump-probe signal can be obtained.

As an example, Figure 2-1 shows $\Delta R(t)/R$ with several distinct features of an Al/Si sample. First, the point with zero time delay is the moment when the optical pump pulse strikes the Al film. The initial sharp spike is due to the heating of electrons in Al, which then rapidly lose their energy to the lattice within a picosecond. This electronic response may greatly affect the shape of the generated acoustic strain pulse as has been studied by previous works [20,21]. The electron diffusion by laser pulse excitation is an

extensive research topic and beyond the scope of this thesis, but its role in picosecond acoustics will be briefly discussed in Chapter 3. Secondly, the slowly decaying curve up to 10 ns is dominated by the thermal diffusion across Al/Si and into the Si substrate. Finally, an acoustic echo is present at a time delay of ~ 50 ps, which corresponds to the round trip time of an acoustic wave traveling within the ~ 160 nm thick Al film. This is due to the perturbation of Al reflectivity by the part of the strain pulse that is reflected from the Al/Si interface. Since Al and Si have very similar acoustic impedances, a second echo by multiple reflections is hardly visible. The details of these physical processes will be further discussed in Section 2.3, where mathematical descriptions and the extraction of important properties are presented.

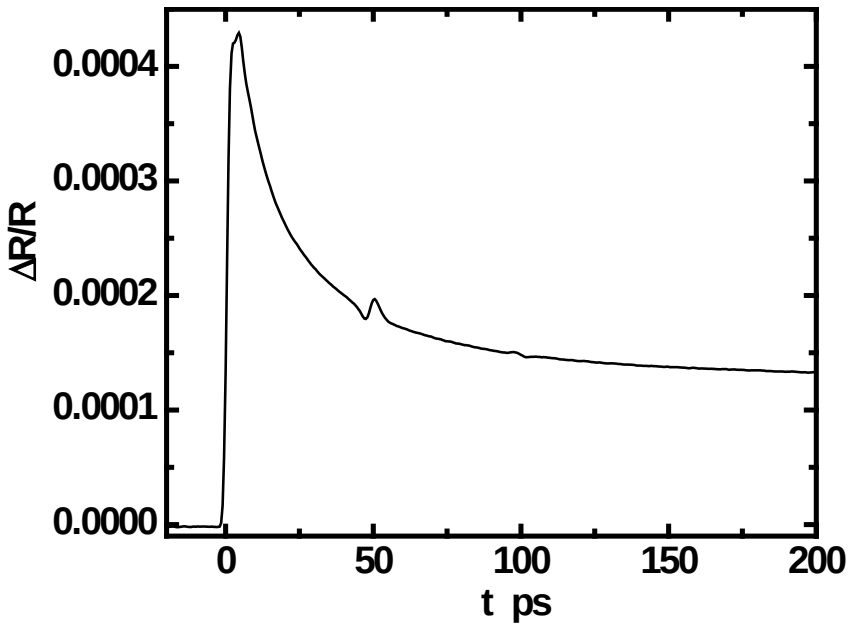

Figure 2-1 Time-resolved reflectivity change of Al-coated Si after laser pulse excitation.

2.2 Pump-probe laser setup

The time-resolved optical pump-probe technique was developed in mid-1980s when picosecond pulse lasers were readily accessible. Here we first discuss briefly the key components used in most pump-probe setups with a mechanical delay of beam paths (Section 2.2.1), and then we focus on the setup based on asynchronous optical sampling (ASOPS) used in measurements for this thesis work.

2.2.1 Mechanical delay line

Shown in Figure 2-2 [22] is a schematic of the experimental apparatus with a mechanical translation stage that is widely used for pump-probe measurements. The titanium sapphire ($Ti:Al_2O_3$) laser has been a popular choice for an ultrafast oscillator due to its ability to generate ultrashort pulses and tunability over a wide wavelength range (650 – 1100 nm), although in recent years, a growing number of other options have also drawn much attention, such as Yb:fiber, Er:fiber, Nd:glass lasers, etc. Some typical parameters for a Ti:sapphire laser pump-probe system are also listed in Figure 2-2. The laser output is split into pump and probe by a non-polarizing beam splitter. The pump beam is usually modulated by an acousto-optic or electro-optic modulator at a frequency on the order of 1 MHz. The probe beam travels through a dove prism (or retro-reflector) mounted on a mechanical translation stage to achieve variable delay with respect to the pump beam. The polarization of the probe beam is rotated by a half-wave plate by 90 degrees so that the two beams are cross-polarized. Both pump and probe beams are focused through lenses onto the same spot (~ 10–100 μm in diameter) on the sample of interest, where the intensity of the pump beam is usually greater than that of the probe

beam. The reflected (or transmitted, if a transmission configuration is utilized) pump light is filtered by a polarizer prior to the detector and the reflected probe light is incident on a high-bandwidth photodetector. As the optical delay is varied through mechanical translation, the reflectivity (or transmissivity) data is recorded using a lock-in amplifier set at the same frequency as the pump beam modulator.

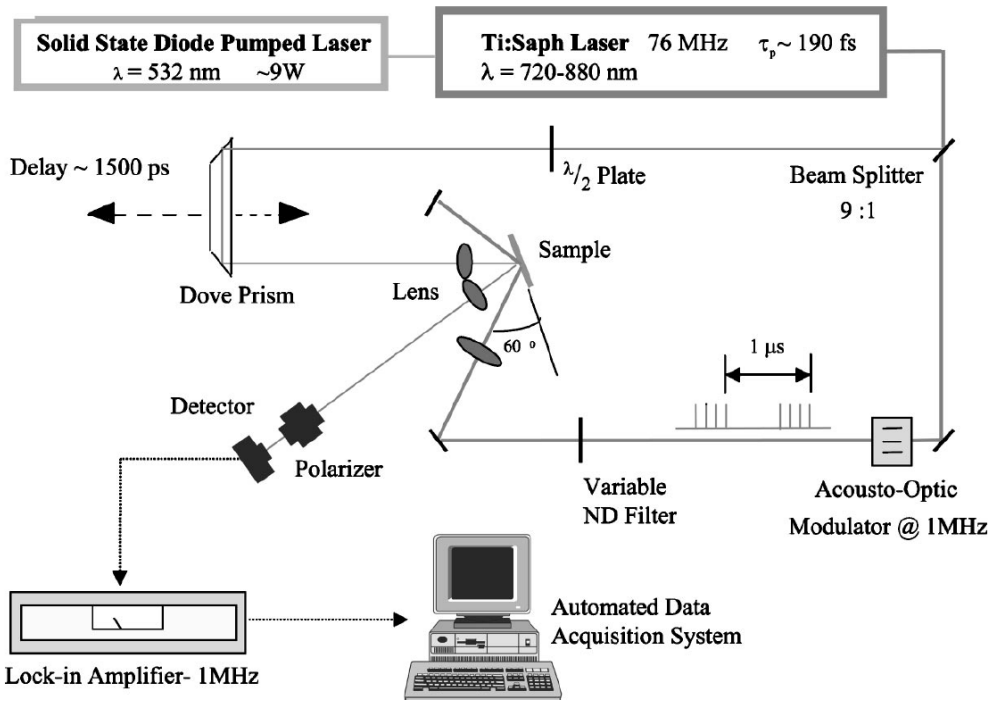

Figure 2-2 A typical optical pump-probe system with mechanical delay line [22].

One disadvantage in the conventional pump-probe system described above is that the relatively slow mechanical scanning limits the speed of data acquisition. Optical alignment could be a major challenge for long scans where slight deviation or divergence of the probe laser will affect the focusing as well as the overlap condition of the two beams. Furthermore, a very long translation stage taking much space is needed to achieve a wide time window (e.g., 1.5 m travel distance for 10 ns). Resulting systemic errors in experimental data have been discussed in several papers [23-25], including factors such

as the misalignment of pump and probe beams on the translation stage, the focal spot size or overlap condition change with varying mechanical delay, and residual pump power on the photodiode, etc.

2.2.2 Asynchronous Optical Sampling (ASOPS)

In the present study, we employ a greatly improved optical pump-probe system based on the asynchronous optical sampling (ASOPS) technique. Although the principle of the ASOPS technique could be dated back to three decades ago, it was only recently that Bartels et al. [26] demonstrated the use of ASOPS to successfully excite and detect coherent acoustic phonons. However, their ASOPS system is based on two Ti:sapphire femtosecond lasers that operate at 1 GHz repetition rate, which limits the total time window to 1 ns (inverse of 1 GHz). A significant amount of transient physics including thermal diffusion and coherent vibrational modes are not fully captured on such a short time scale.

In the ASOPS system (Clarke lab) used for our measurements [27], two erbium-doped fiber lasers are phase-locked at a repetition rate f_R = 100 MHz with a tunable slight frequency offset Δf between 0.2 and 7 kHz. This enables a continuously variable time delay between pump and probe lasers, with a total transit time of 10 ns and a time delay step (Δt) adjustable from 20 fs to 700 fs. In practice, the temporal resolution is determined by several factors including the pulse duration, frequency offset, and data acquisition bandwidth. Figure 2-3 illustrates the pump and probe pulse trains in real time as well as the corresponding time delay during the measurement scan.

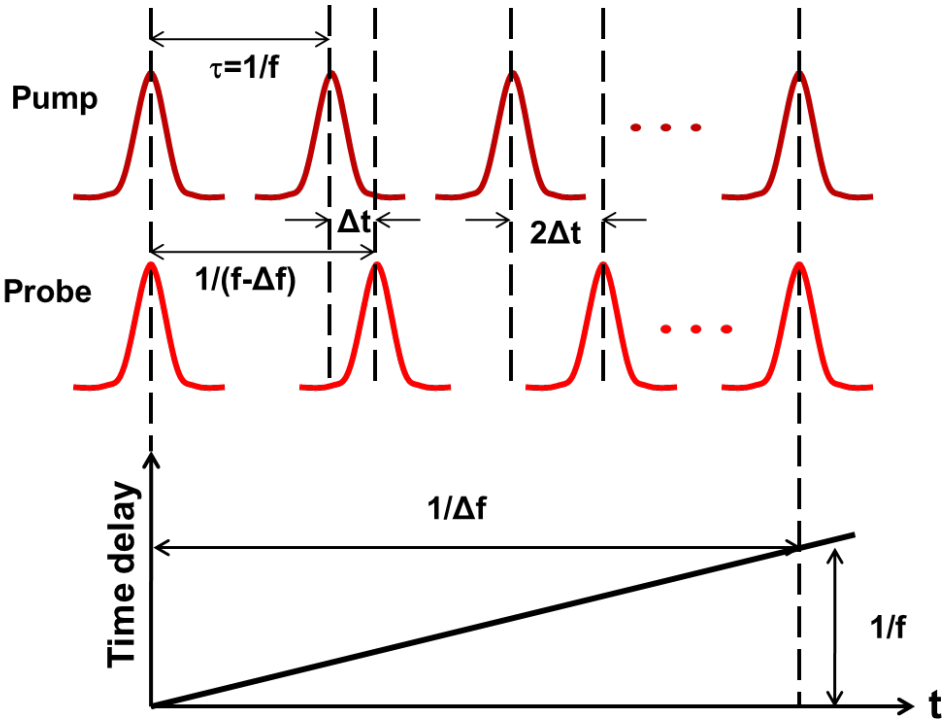

Figure 2-3 Time delay between pump and probe pulses in ASOPS.

Figure 2-4 shows a schematic of the experimental setup in the reflection configuration with major optical components. One of the lasers (B) is frequency-doubled to 780 nm from the fundamental wavelength 1560 nm. Detailed specifications of the laser beams can be found in Chapter 3. Both pump and probe laser beams are expanded first for the purpose of tighter focusing and then collimated to minimize beam divergence. In each beam's pathway there are a half-waveplate and a linear polarizer for the tuning of intensity and polarization. The two collimated beams are combined by a dichroic mirror and sent to a parabolic mirror, which focuses the beams onto the sample. In this configuration the two beams are aligned so that they are perfectly collinear; the parabolic mirror avoids the chromatic aberration that commonly exists in lens focusing. These techniques ensure a concentric overlap of the pump and probe focal spots on the surface

of the sample. The pump and probe wavelengths are readily interchangeable by varying the expansion ratio of each beam and thus the respective focal spot size.

The probe beam reflected by the sample is monitored on a balanced amplified differential photodetector with the reference arm partly split from the original probe beam; the reflected pump beam is either blocked by a color filter or outside the detection wavelength range of the photodetector. The differential reflectivity is recorded by a computer-based 14-bit PCI digitizer card that is capable of averaging over several thousand temporal traces to achieve a signal-to-noise ratio above 10^7. The combination of the differential detection and hardware averaging fosters efficient data acquisition, eliminating the need for a lock-in amplifier.

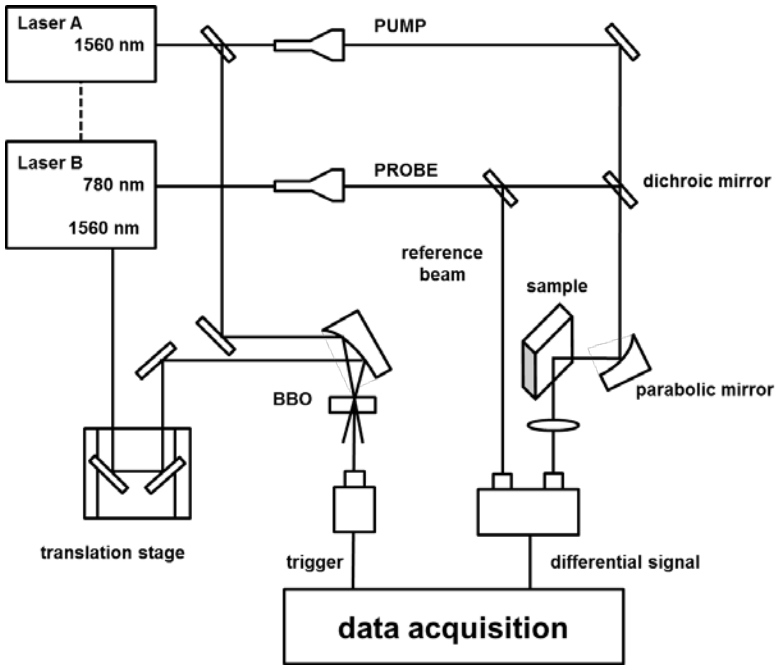

Figure 2-4 ASOPS system for optical pump-probe measurements.

To minimize time jitter and optimize temporal resolution, a cross-correlation signal between the two laser pulse trains is used as a real-time optical trigger for data acquisition. A small portion of the 1560 nm beam from each laser is focused by another parabolic mirror onto a beta barium borate (BBO) crystal, and the nonlinear sum frequency generated 780 nm light is collected as the cross-correlation trigger signal.

2.3 Mathematical descriptions

In this section we present mathematical models [28,29] that are widely adopted to describe the generation and detection of acoustic waves by ultrafast laser pulses. The model for extracting thermal transport properties as well as corrections for the ASOPS system will be discussed in Section 2.4.

We first assume a laser pulse with energy Q is deposited onto the surface of a metal transducer within the laser penetration depth ζ. The laser spot radius r is assumed to be significantly larger than the film thickness d, whereas ζ is small compared to d. Therefore, the temperature and thermal stress in the metal only vary in the direction of z, i.e., the depth into the metal film. Instantaneously, the one-dimensional profile of temperature rise is

$$\Delta T(z) = (1 - R)\frac{Q}{CA\zeta}e^{-z/\zeta} \tag{2.1}$$

where R is the optical reflectivity, C is the volumetric specific heat, and A is the laser-illuminated area. The initial thermal stress generated by this temperature profile is then:

$$\sigma_{zz} = 3\frac{1-\nu}{1+\nu}B\eta_{zz} - 3B\beta\Delta T(z) \tag{2.2}$$

where ν is the Poisson's ratio, β is the linear expansion coefficient, and B is the bulk modulus. Note that the stress is only a function of z, and thus η_{zz} becomes the only non-vanishing component of the elastic strain tensor. The wave equation of acoustic propagation is simply:

$$\rho \frac{\partial^2 u_z}{\partial t^2} = \frac{\partial \sigma_{zz}}{\partial z} \tag{2.3}$$

where u_z is the instant z-direction displacement and ρ is the density, with the relation between displacement and strain being:

$$\eta_{zz} = \frac{\partial u_z}{\partial z} \tag{2.4}$$

The initial condition for solving Equations (2.2) - (2.4) is zero strain throughout the film; the boundary condition requires that the surface is stress-free. If we assume the film is infinitely thick and the thermal diffusion process is slow compared to strain propagation, the solution of the strain field is found to be [28,29]:

$$\eta_{zz}(z,t) = \eta_0 \left[e^{-z/\zeta} - \frac{1}{2} e^{-(z+vt)/\zeta} - \frac{1}{2} e^{-|z-vt|/\zeta} sgn(z-vt) \right] \tag{2.5}$$

where $\eta_0 = (1-R)\frac{3Q\beta}{CA\zeta}\frac{1+\nu}{1-\nu}$ is a constant strain determined only by the laser pulse energy and the material properties. The strain profile in a laser-excited Al film is plotted in Figure 2-5 at different times as a function of spatial depth. The bi-polar shape of the strain pulse originates from the π-phase shift induced by the initial acoustic reflection at the air/Al interface. Reflections at each interface will influence the acoustic echoes as seen in Figure 2-1, which is discussed in detail in Chapter 5.

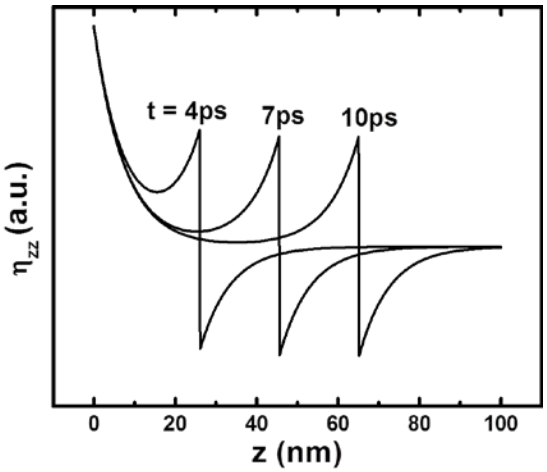

Figure 2-5 Laser-excited strain profile in Al.

Accounting for heat transfer during strain wave propagation is a significantly more complex problem, and is covered in Refs. 28 and 29. Consider a strain pulse propagating in a laser-excited Al film on a sapphire substrate; when the strain wave reaches the Al/sapphire interface, reflection and transmission occur according to the acoustic impedances of the two materials. Figure 2-6 illustrates the strain intensity within the system as a function of time and space. The slope of the line represents the sound velocity, and the reduced intensity upon each reflection is a result of energy transmitted to the substrate or lost through scattering.

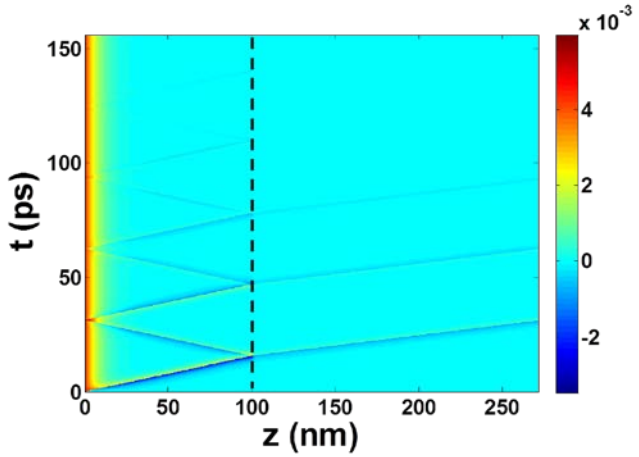

Figure 2-6 Propagation of laser-excited strain in a 100 nm Al film on a sapphire substrate.

The temperature change and acoustic strain can each modulate the refractive index and induce an optical response that is detected by the probe pulse. The detection mechanism alone has been a subject of study that is beyond the scope of the dissertation, and can be found in numerous references [28,29]. From the detected acoustic transient, we can obtain information such as acoustic phonon reflection coefficient at the interface and elasticity of the material.

2.4 TDTR with ASOPS

The samples used in TDTR measurements are usually coated with an aluminum transducer film ~80–120 nm in thickness. The heat dissipation in aluminum takes less than 100 ps, which is significantly faster than the diffusion into the underlying layer, which occurs on the time scale of nanoseconds. Therefore, it is often assumed that the Al film gets an initial instantaneous temperature rise and maintains a spatially uniform temperature. Because there is assumed to be negligible temperature gradient within Al, T_{Al} is only a function of time in the TDTR calculation model. As mentioned in Section 2.3, since the dimension of the laser spot on the sample is much greater than the heat penetration depth, thermal transport can be described using a simple one-dimensional heat diffusion model:

$$\kappa_s \left.\frac{\partial T_s(z,t)}{\partial z}\right|_{z=0} = C_{Al} d_{Al} \frac{\partial T_{Al}(t)}{\partial t} \tag{2.6}$$

$$\kappa_s \frac{\partial^2 T_s(z,t)}{\partial z^2} = C_s \frac{\partial T_s(z,t)}{\partial t} \tag{2.7}$$

$$\kappa_s \left.\frac{\partial T_s(z,t)}{\partial z}\right|_{z=0} = -\sigma_K \left[T_{Al}(t) - T_s(0,t)\right] \tag{2.8}$$

where κ_s is the thermal conductivity of the sample and σ_K is the Kapitza conductance (thermal boundary conductance) at the Al/sample interface. The subscript *s* denotes the sample that is covered by Al. All the given temperatures are relative to the steady state temperature. The set of equations can be solved analytically through Laplace transforms [29] or numerically using a finite difference method. Here the physical properties of interest κ_s and σ_K can be extracted by comparing the calculated temperature $\Delta T_{Al}(t)$ with the measured time domain reflectivity change $\Delta R(t)$.

Researchers have established systematic data analysis tools for TDTR on systems with a mechanical delay line [23-25]. The ASOPS systems are immune to the errors caused by misalignment or beam size variation during the scan. However, due to the high repetition rate (100 MHz in our case), the heating caused by accumulated absorption of multiple laser pulses must be taken into account. Shown below is a schematic (Figure 2-7) of the temperature profile with heating from a train of pulses.

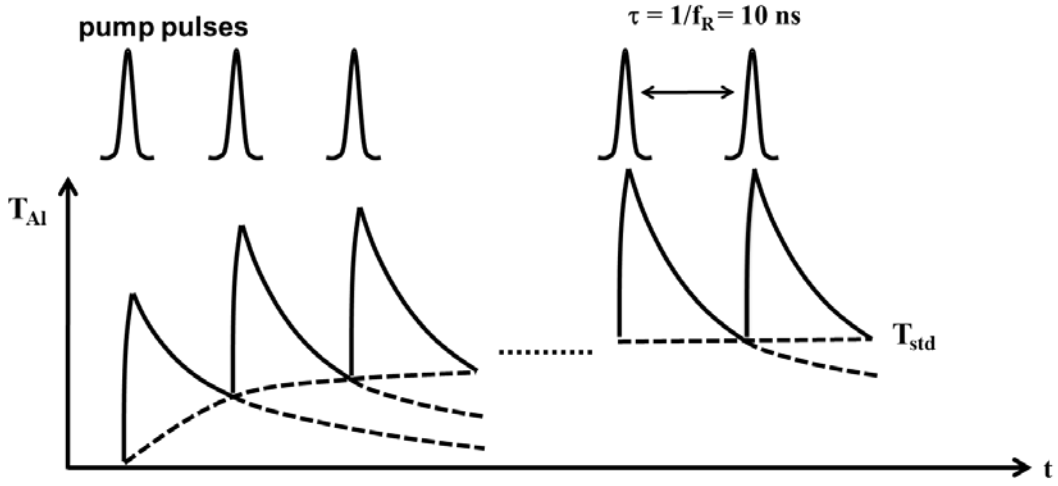

Figure 2-7 Cumulative heating by multiple pulses.

The Al temperature rise induced by a single pump pulse, after solving Equations (2.6), (2.7), and (2.8), can be written as $\Delta T_p(t)$. The cumulative temperature rise can then be expressed as a summation over the pulse number N:

$$\Delta T_{Al}(t) = \sum_{N} \Delta T_p\left(t - N \cdot \tau\right) \tag{2.9}$$

The steady state temperature T_{std} can be calculated in a similar manner and further subtracted from $T_{Al}(t)$. Thermal transport properties are usually treated as fitting parameters for comparison with the measured trace.

For calibration, a silicon substrate coated with 100 nm Al is first measured. The extracted values for the thermal conductivity κ_{Si} and thermal boundary conductance σ_K between Al and Si are ~150 W/m-K and ~2×10^8 W/m^2-K, respectively, which agree well with literature values [22,30]. In this particular case, we note that the thermal accumulation effect is not very significant as heat dissipates quickly in Al/Si and the 10 ns time window is sufficient for thermal relaxation (Figure 2-1).

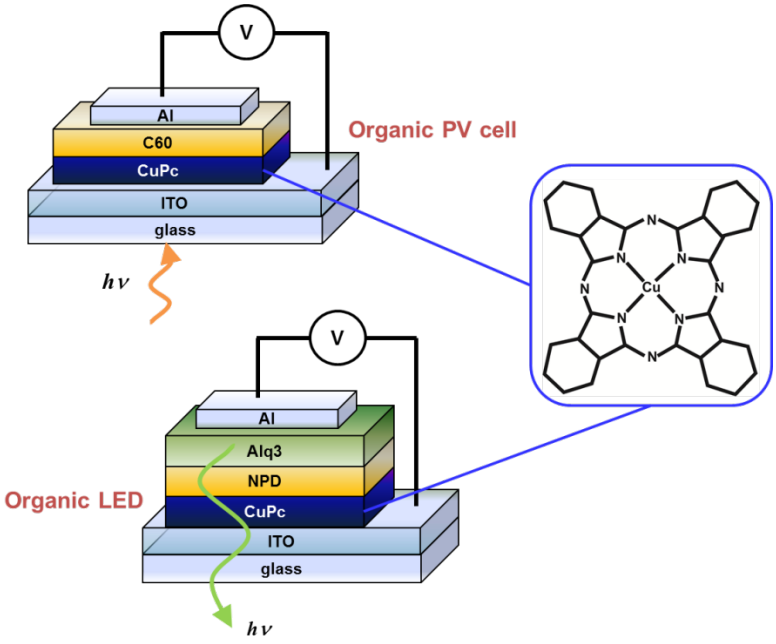

Figure 2-8 CuPc in organic optoelectronic devices.

As another example, a copper phthalocyanine (CuPc) thin film coated with 100 nm Al is measured using the above-mentioned method. CuPc is a small molecule semiconductor widely used in organic optoelectronic devices such as photovoltaics and light-emitting diodes. Schematics of layered device structures are shown in Figure 2-8.

With shrinking dimensions and increasing performance demands, the larger current density in these devices requires efficient removal of heat during operation. Device failures or low efficiency related to overheating or hot spots have been reported [31-33]. For these reasons, characterization and fundamental understanding of thermal transport in functional thin films such as CuPc are much needed. While thermal properties of conventional inorganic semiconductors (e.g., Si, GaAs, etc.) have been well characterized, studies of organic materials are relatively scarce. Organic compounds, due to their complex structures and versatile forms, are expected to have unique thermal and elastic characteristics. In general they have low densities (ρ) and sound velocities (v) and thus small acoustic impedances ($Z = \rho v$). Metal/organic interfaces (Figures 2-8 and 2-9) are commonly present in organic optoelectronic devices; these two types of materials are largely different in properties relevant to heat transfer (Table 2-1).

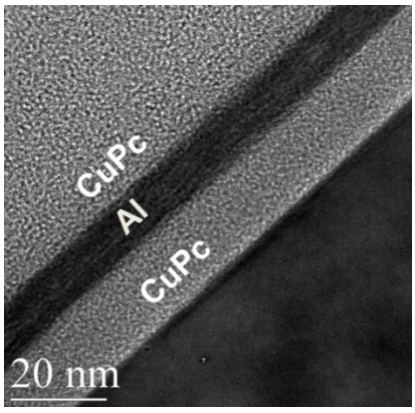

Figure 2-9 TEM image of Al and CuPc thin films in a layered structure (taken by Dr. Kai Sun, EMAL, University of Michigan).

	Lattice spacing	Bond type	Bond energy	Heat carriers
Al	4 Å	metallic	1.5 – 2 eV	free electrons and phonons
CuPc	5 ~ 20 Å	van der Waals	0.03 – 0.1 eV	phonons

Table 2-1 Properties of Al and CuPc.

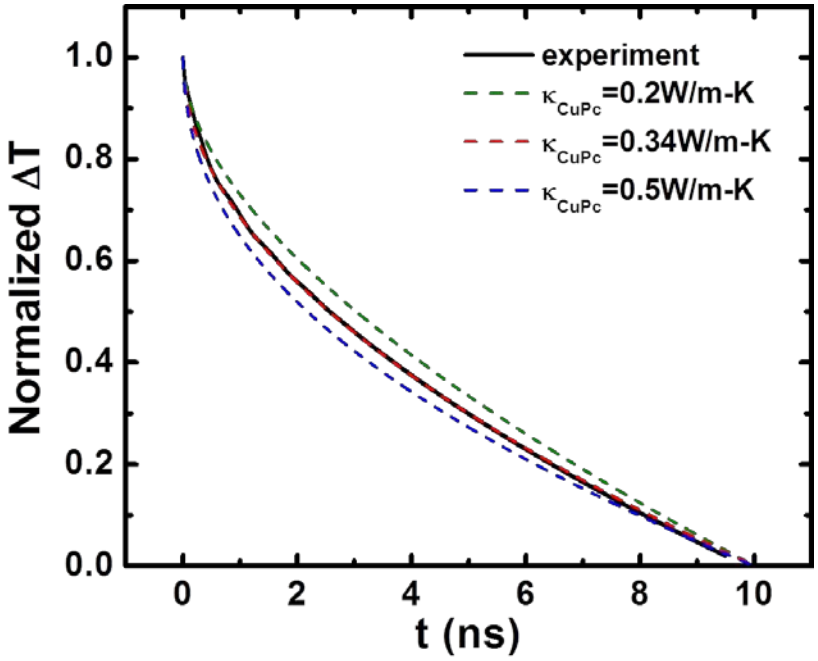

Figure 2-10 Measured (solid black curve) and simulated (dashed curves) transient temperature. The numerical simulation gives a best fit to the experiment with κ_{CuPc} = 0.34 W/m-K (dashed red curve).

Figure 2-10 plots the normalized temperature $\Delta T_{Al}(t)$ for both the TDTR measurement and the simulation with Equations (2.6) through (2.9). The curve fitting is very sensitive to κ_{CuPc}, and the extracted thermal conductivity κ_{CuPc} is 0.34 ± 0.1 W/m-K, given the uncertainty in the specific heat of CuPc. Here we have neglected the thermal boundary conductances at the Al/CuPc and CuPc/Si interfaces, as CuPc is a fairly poor

thermal conductor. A dimensionless Biot number can be used to characterize the heat transfer process, which is defined as the ratio of thermal conductances at the interface and across the bulk film. In this particular case,

$$Bi = \frac{\sigma_K d_{Al}}{\kappa_{CuPc}} \tag{2.10}$$

σ_K is generally on the order of 10^8 for metal/dielectric and metal/semiconductor interfaces, and *Bi* is thus much greater than 10. This indicates that the heat diffuses much faster at the Al/CuPc interface than inside the CuPc film, the latter dominating the thermal resistance.

A large Biot number reduces the calculated $\Delta T_p(t)$ to a simple analytical form [29]:

$$\Delta T_p(t) = (1 - R_{Al}) \frac{Q}{C_{Al} A d_{Al}} \exp\left(\frac{\kappa_s C_s}{d_{Al}^2 C_{Al}^2} t \right) \operatorname{erfc}\left(\sqrt{\frac{\kappa_s C_s}{d_{Al}^2 C_{Al}^2} t} \right) \tag{2.11}$$

where the decay constant can be written as $\tau_s = d_{Al}^2 C_{Al}^2 / (\kappa_s C_s)$.

Similarly, for a small Biot number when the interface resistance is dominant:

$$\Delta T_p(t) = (1 - R_{Al}) \frac{Q}{C_{Al} A d_{Al}} \exp\left(-\frac{\sigma_K}{d_{Al} C_{Al}} t \right) \tag{2.12}$$

and the decay constant becomes $\tau_K = d_{Al} C_{Al} / \sigma_K$.

Our collaborative work [34] reports a value of 0.39 W/m-K for κ_{CuPc} measured using the 3-omega technique [35,36]. The thermal conductivity for such organic thin films (including polymers) usually ranges from 0.2 to 1.0 W/m-K [37-39]. Ref. 34 has also estimated the thermal boundary conductance at the Al/CuPc interface to be 5×10^7 W/m^2-K. Using these values, the Biot number in Equation (2.10) is calculated to be 12.8,

which again justifies the assumption made in the TDTR calculation. Some other collaborations involving TDTR measurements include focused ion beam (FIB) irradiated gallium arsenide (GaAs:N) [40] and femtosecond laser treated antimony telluride (Sb_2Te_3) [41].

As illustrated in Figure 2-11, nitrogen is first implanted into GaAs substrates at different ion energies to form supersaturated "amorphous" GaAsN. FIB irradiation is then employed to create arrays of nucleation sites. Subsequent rapid thermal annealing results in GaAs:N with arrays of GaN nanocrystals.

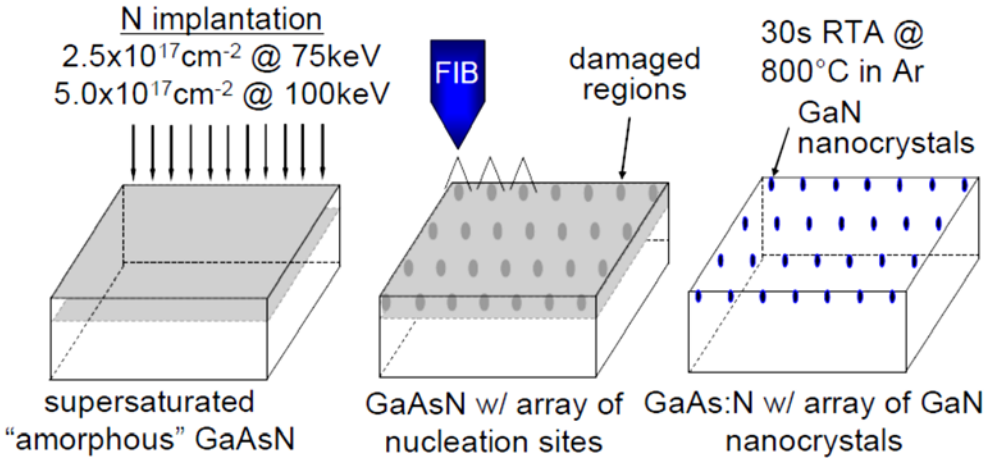

Figure 2-11 GaAs:N nanocrystal formation with FIB irradiations [40].

Figure 2-12 plots the extracted effective thermal conductivity of GaAs:N samples with different processing conditions. All three samples have exhibited significantly lower thermal conductivity than that of bulk GaAs crystals (55 W/m-K), which could be attributed to the formation of an amorphous layer on the sample surface. The annealed GaAs:N sample is slightly more conductive than the other two due to the removal of

supersaturated amorphous GaAsN at the surface as well as the formation of GaN nanocrystals.

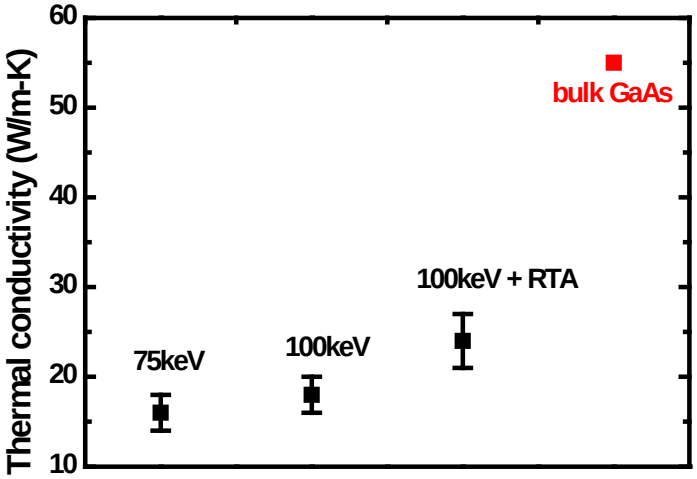

Figure 2-12 Effective thermal conductivity of nitrogen implanted GaAs.

Femtosecond lasers are known to be capable of forming semiconductor nanostructures [42-44]. A 1580 nm laser has been used to create nanotracks on the surface of Sb_2Te_3, as shown in Figure 2-13 [41]. The TDTR-measured thermal conductivity of 0.59 W/m-K for the laser-irradiated regions is smaller than that measured by TDTR for the non-irradiated regions (0.62 W/m-K) [45]. The reduction in thermal conductivity for ion- or laser-treated nano-materials suggests potential applications such as thermoelectrics.

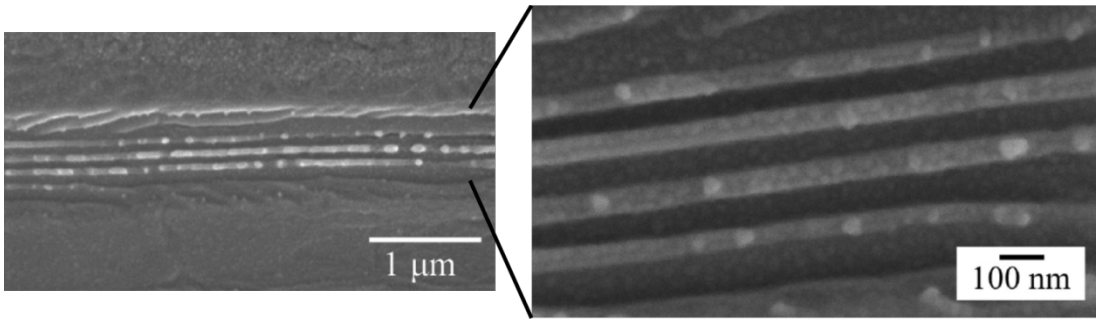

Figure 2-13 SEM image of nanotracks formed on Sb_2Te_3 by a 1580 nm femtosecond laser [41].

2.5 Conclusion

Pump-probe techniques based on ultrafast lasers provide a powerful means to characterize phonon and thermal transport. ASOPS provides unique advantages in fast scanning and wide temporal dynamic range as well as the elimination of errors caused by mechanical delay. We have measured the thermal conductivities of several samples with nanostructured interfaces. We have shown that nanostracks or nanocrystals formed at the interface greatly reduce thermal conductivity because of enhanced phonon boundary scattering. We have also found that metal/organic interfaces, which are common in organic semiconductor devices, have especially high thermal boundary resistance.

Chapter 3

Coherent confined acoustic phonon modes in metal-organic thin films

With picosecond acoustics, we are able to measure important properties including the thickness and elasticity of a thin film as well as the bonding strength at an interface between two materials. In addition, the time-resolved nature of this technique allows us to probe other fundamentally critical characteristics such as coherent phonon modes of a nanostructure and life times of these modes.

Acoustic phonons may be confined in an acoustically isolated medium enclosed by boundaries with high acoustic impedance mismatches. In this chapter we insert a compliant organic (CuPc) film at an Al/Si interface to form an acoustic cavity. We employ picosecond acoustics to study the dynamics of coherent acoustic phonons excited by femtosecond lasers and discuss the role of the CuPc film from novel perspectives [46].

3.1 Previous work and inspirations

Coherent acoustic control has been examined in recent work related to optoexcited micromechanical resonators, which present interesting behavior associated with the coupling of light with high frequency acoustic vibrational modes [47-50].

Similar to mode control in optics, acoustic waves can be regulated using both active (excitation-based) and passive (structure-based) techniques. Among these, optical actuation affords a great number of possibilities for active coherent control of vibrational dynamics [51,52]. For example, timing of optical driving pulses [53] and tuning of optical field strength [47] have each been demonstrated as an effective approach for the selective strengthening or suppression of multiple resonant modes within a given acoustic spectrum. Meanwhile, passive means that utilize free-space optical cavities [54] or structure modification can likewise provide coherent acoustic control. Some examples include optical [55] and acoustic [56] distributed Bragg reflectors integrated within a resonator structure, which have each been used to enhance a transduced acoustic mode.

Inspirations of this work partly come from free-standing membrane structures that have recently been considered for high-frequency (10+ GHz) acoustic resonator applications. Femtosecond laser pulses are known to be able to simultaneously excite a membrane's resonant longitudinal acoustic modes up to the 15^{th} harmonic (285 GHz) [57,58].

As discussed in Chapter 2, the absorption of a femtosecond optical pulse by a transducer typically leads to broadband impulsive strain with a spectral width greater than 100 GHz [20]. It is common in optics to employ coherent control techniques for mode selection from a broadband comb of excited cavity modes. One example is the use of a Fabry-Pérot etalon, which is typically a transparent plate with two reflecting surfaces (Figure 3-1(a)) that exhibits peaks in its transmission spectrum (as a function of wavelength) corresponding to its Fabry-Pérot resonances. In solid state lasers, optical etalons are used to achieve tunable single mode operation by suppressing longitudinal

modes that are adjacent to a selected frequency [59,60] (Figure 3-1(b)). Here, using the same philosophy, we propose and demonstrate an integrated acoustic etalon as a passive means to selectively strengthen or suppress multiple resonances within an acoustic cavity.

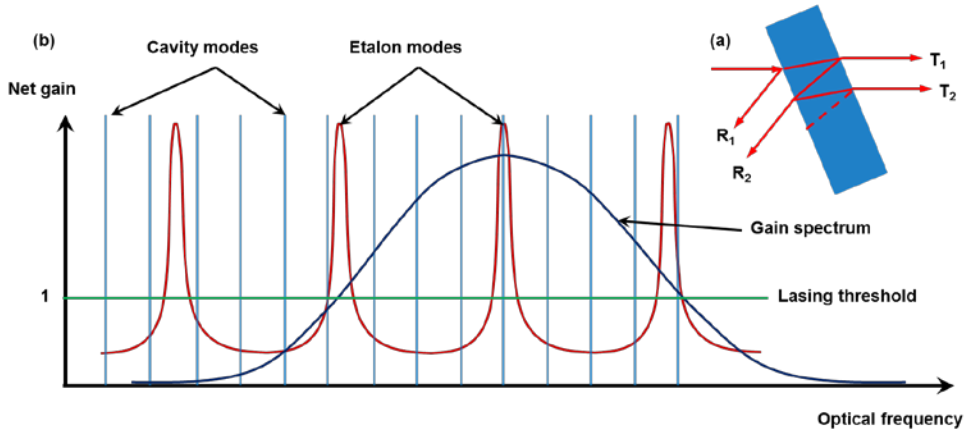

Figure 3-1 (a) Intracavity etalon and (b) its use for line selection in realizing a single-mode HeNe laser.

Suspended membrane resonators are limited in that they cannot couple energy to external media. We there consider a supported membrane resonator. Several recent studies have focused on the laser-excited acoustic dynamics of supported thin films [53,61-65]. When a metal transducer with thickness much greater than the optical penetration depth [54,61] is in contact with a hard (high elastic modulus) material such as silicon or sapphire, the absorption of laser pulses by the transducer is known to result in a train of acoustic echoes rather than resonant vibrations of the film. If the transducer thickness is reduced to the order of the optical penetration depth, the first resonant vibrational mode of the transducer is excited as energy directly couples from the laser pulse to this mode. However, due to the limited film thickness in this case, higher-order modes (harmonics) are typically beyond the spectral range of the transduced acoustic pulse and thus either absent or only very weakly excited [62,66,67].

In this work we will show that multiple vibrational modes can be strongly optoexcited in a relatively thick metallic resonator by inserting a compliant organic supporting film at the interface. The organic film can further be employed as the acoustic equivalent of an optical etalon to control the resulting mode spectrum within the acoustic cavity. Like its optical analog, the acoustic etalon is placed within the cavity and mode control is accomplished by utilizing its Fabry-Pérot transmission maxima (at which wavelengths the cavity field is concentrated within the etalon [60]) or its reflection maxima (where the etalon acts as a resonant reflector [60]). In either operating regime, desired cavity modes are retained or rejected. For the particular acoustic etalon described here, multiple transmission and reflection peaks fall within the bandwidth of excited acoustic modes. The etalon therefore acts as a resonant transmitter for certain modes and a resonant reflector for other modes; it can thereby be used to select a certain resonant mode, tune the frequency of a resonant mode, or introduce additional resonances into the system.

3.2 Experimental procedures

The resonant vibrational modes of a thin film occur at frequencies with a spacing of $v/2d$, where v is the acoustic velocity and d is the film thickness. The peak frequency of the laser-excited initial strain wave is $v/2\pi\zeta$, where ζ is the optical penetration depth and aluminum has a ζ value of approximately 8 nm for the λ=1560 nm pump light. To significantly excite a range of resonator modes (for example, up to the 4^{th} harmonic), an aluminum thickness $d > 4\pi\zeta \sim 100$ nm is required. As hot electron diffusion may cause

the thermal stress to extend significantly beyond the optical penetration depth [20,21], we choose a conservative aluminum thickness of 200 nm.

A vacuum thermal evaporator (Angstrom Engineering Inc.) is used for depositions of a film of copper phthalocyanine (CuPc) and a 200 nm aluminum film onto a (100) silicon substrate (Figure 3-2). CuPc is a small molecule semiconductor that is widely used in organic optoelectronic devices. The compliant CuPc film is sandwiched between the Al and Si, allowing the Al membrane to vibrate at its fundamental and harmonic modes. The strong acoustic impedance mismatches at the Al/air and CuPc/Si interface forms a cavity that confines acoustic waves. The interfacial CuPc layer acts as a Fabry-Pérot etalon for these waves as discussed in Section 3.2. To demonstrate the coherent mode control afforded by the CuPc etalon, a series of samples is prepared in which the etalon thickness is varied from 0 nm to 77 nm. A schematic of the sample preparation and picosecond acoustics measurement configuration is illustrated in Figure 3-2.

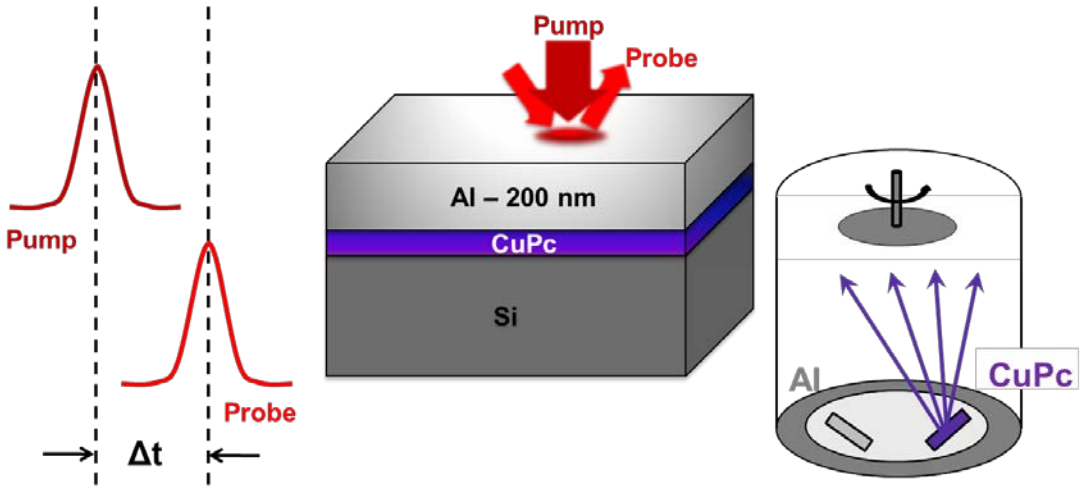

Figure 3-2 Sample preparation and pump-probe measurement configuration.

The resonator is then excited and measured using an ultrafast pump-probe setup (see Chapter 2 for more details). The λ = 1560 nm laser is used as the pump beam and focused on the sample with a spot diameter of approximately 4 μm, and the frequency doubled λ = 780 nm laser (a separate unit phase-locked to the pump laser) is used as the probe beam and focused on the same area with a smaller diameter of approximately 3 μm. The pump laser has a pulse width of ~ 100 fs, and the probe pulse has a pulse width of ~ 150 fs. The pump beam power is tuned to 13 mW (0.13 nJ pulse energy) to avoid sample damage while retaining a significant excitation. The probe beam has a power of approximately 300 μW (3 pJ pulse energy), making its absorption negligible compared to that of the pump beam. An amplified balanced photodetector (Thorlabs, PDB210A) with common mode rejection is used to record the differential signal between the probe and reference beams. 300 μW is just sufficient to saturate a single diode of the detector (when not balanced), ensuring a high signal-to-noise ratio without causing nonlinear effects at the detector.

3.3 Results and discussion

3.3.1 Acoustic transients and modes

The pump laser pulse deposits its energy into the aluminum film within a highly localized region (~ 8 nm penetration depth), with heated electrons rapidly diffusing deeper into the film [21]. The generated thermal stress subsequently launches an acoustic strain wavepacket with frequency content in the range of 0-200 GHz, where the peak frequency is determined by the hot electron diffusion length in the Al film [20]. This broadband strain pulse propagates within the structure, coupling to its resonant acoustic

modes. The resulting acoustic dynamics are captured by the time variation in optical reflectivity, $\Delta R(t)$; the amplitude of the strain on the Al surface is known to scale with $\Delta R/R$.

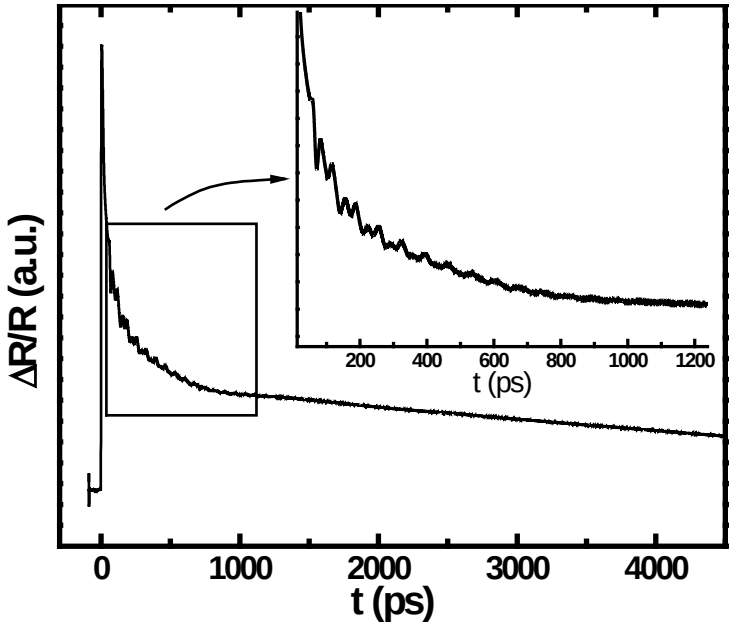

Figure 3-3 Transient reflectivity change of the Al/CuPc (77 nm)/Si sample.

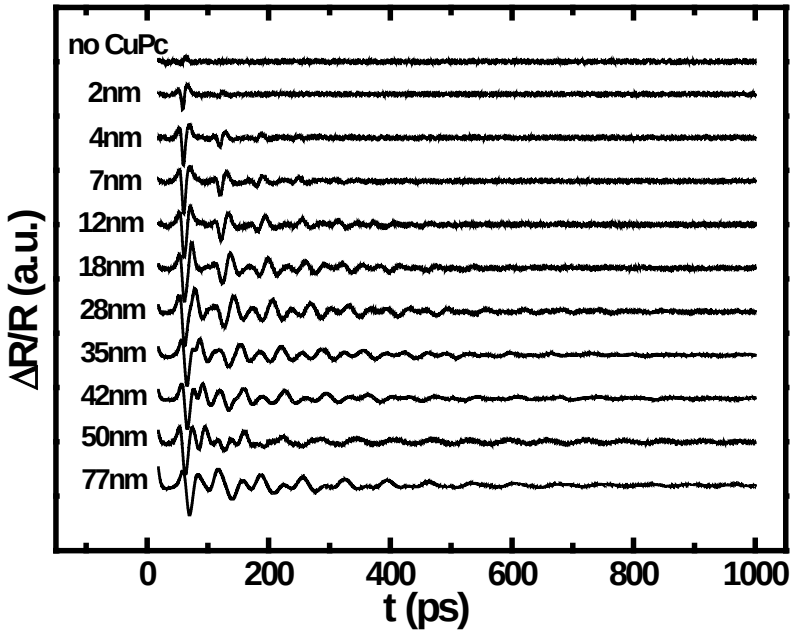

Figure 3-4 Acoustic transients of Al/CuPc films on Si with varied CuPc thickness [46].

Figure 3-3 displays a typical transient reflectivity change of an Al/CuPc/Si (77 nm CuPc in this case), where acoustic features overlay on top of the thermal decay as discussed in Chapter 2. By subtracting the electronic and thermal decay, acoustic transients for all samples are obtained and plotted in Figure 3-4.

With no CuPc at the interface, only one tiny acoustic echo is seen because Al and Si have very similar acoustic impedances. As the CuPc thickness increases, a series of echoes starts to appear and grows in intensity due to increasing acoustic impedance contrast. For small values of the CuPc thickness ($d_{\mathrm{CuPc}} < 7$ nm), the Al membrane is insufficiently decoupled from the Si substrate for resonant membrane modes to be excited, and the echo pattern still dominates the resulting time dynamics. For CuPc thicknesses of 7 nm and greater, the acoustic transients predominantly exhibit superimposed damped oscillations from excitation of resonant membrane modes. Fast Fourier transforms (FFT) reveal the concurrent excitation of up to five resonant modes (i.e., harmonics up to the 5^{th} order) in these samples. For example, Figure 3-5 shows the FFT for the samples with 18 nm, 50 nm and 77 nm CuPc thickness (from top to bottom), where *m* denotes the mode number. The physical nature of these modes will be discussed in later context.

There is a transition in acoustic dynamics from an echo regime to a resonant vibration regime as the CuPc thickness is increased beyond 7 nm. Two effects contribute to this transition: first, a thicker CuPc film presents a larger effective mismatch in acoustic impedance at the interface and hence results in enhanced acoustic confinement within the Al resonator; second, it has been observed that in the thin film limit, the stiffness of a compliant organic (or polymer) layer scales inversely with its thickness [68-70].

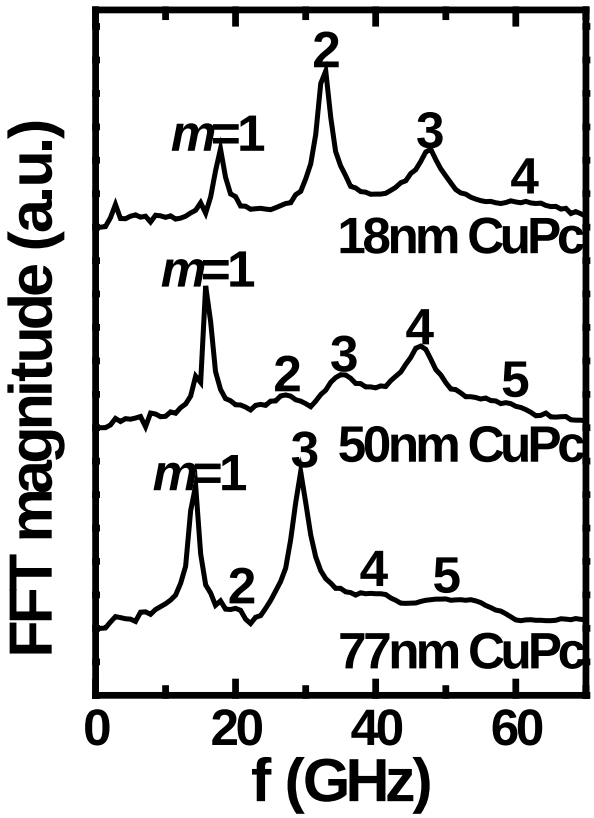

Figure 3-5 Fourier spectra of acoustic transients for samples with 18, 50, and 77 nm thick CuPc layers [46].

To interpret the influence of the CuPc layer on the frequencies and magnitudes of the observed resonant modes, we first examine the acoustic eigen-problem for layered structures. The longitudinal (LA) modes of a free-standing membrane have displacements in the direction normal to the film plane and zero stress on both surfaces. The membrane's quantized LA eigenmodes have frequencies at $f_m = mv/2d$, where m is an integer representing the mode order number, v is the speed of sound, and d is the film thickness (Figure 3-6(a)). Similarly, supported films when acoustically decoupled from their surroundings have discrete LA modes at $f_n = nv/4d$. The mode order number n can be odd or even, depending on the ratio of the acoustic impedances (Z_f/Z_s) of the film and

its supporting material [63,71]: the resonator exhibits even-order modes when $Z_f/Z_s > 1$ (Figure 3-6(b)) and odd-order modes when $Z_f/Z_s < 1$ (Figure 3-6(c)). These two types of elastic structures and their resonant modes are often referred to as "open-pipe" and "closed-pipe" systems and modes, respectively, with analogies drawn from musical instruments. Straightforward similarities can be found by comparing the frequency characteristics and profiles of elastic displacement within the films to those of sound waves in organ pipes.

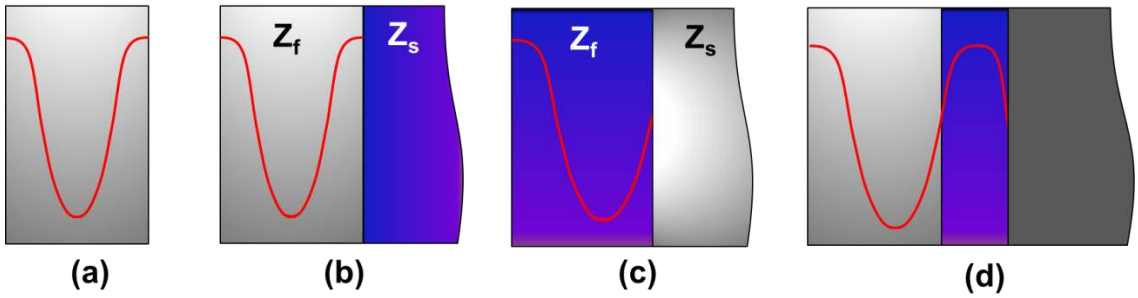

Figure 3-6 Schematics of eigenmode acoustic waves in (a) a free-standing membrane, (b) a "hard" film on a "soft" substrate, (c) a "soft" film on a "hard" substrate, (d) a bi-layer on a substrate.

In our case, since the interfacial CuPc layer is not thick enough to be considered as a semi-infinite supporting medium, we use a transfer matrix approach (similar to the one in Chapter 1) to model the elastic behavior of an Al/CuPc bilayer on a Si substrate (Figure 3-6(d)). The resonant frequencies of such a system turn out to satisfy the following equation:

$$\begin{aligned} &r_{\mathrm{Al/CuPc}} \exp\left(-2j\omega_m \frac{d_{\mathrm{Al}}}{v_{\mathrm{Al}}}\right) + r_{\mathrm{CuPc/Si}} \exp\left[-2j\omega_m \left(\frac{d_{\mathrm{Al}}}{v_{\mathrm{Al}}} + \frac{d_{\mathrm{CuPc}}}{v_{\mathrm{CuPc}}}\right)\right] \\ &-r_{\mathrm{Al/CuPc}} r_{\mathrm{CuPc/Si}} \exp\left(-2j\omega_m \frac{d_{\mathrm{CuPc}}}{v_{\mathrm{CuPc}}}\right) - 1 = 0 \end{aligned} \tag{3.1}$$

where ω_m is the quantized angular frequency of the m^{th} resonant mode, $r_{Al/CuPc}$ and $r_{CuPc/Si}$ are the acoustic reflection coefficients at the Al/CuPc and CuPc/Si interfaces, respectively, and d_{CuPc} and d_{Al} are the thicknesses of the respective films. By definition, $r_{Al/CuPc} = (\rho_{Al}v_{Al}-\rho_{CuPc}v_{CuPc})/(\rho_{Al}v_{Al}+\rho_{CuPc}v_{CuPc})$ and $r_{CuPc/Si} = (\rho_{CuPc}v_{CuPc}-\rho_{Si}v_{Si})/(\rho_{CuPc}v_{CuPc}+\rho_{Si}v_{Si})$, where the assumed densities and sound velocities are ρ_{Al} = 2700 kg/m^3, ρ_{CuPc} = 1600 kg/m^3, and v_{Al} = 6420 m/s [17]. While there are no literature data available for the speed of sound in CuPc, well-characterized organic materials such as PMMA (poly(methyl methacrylate)) are reported to have values in the range of 2500 - 3000 m/s [72]. Here we allow v_{CuPc} to be the sole fitting parameter in what follows, deriving a value of 3000 ± 200 m/s. Measured resonant frequencies for the samples are plotted as blue circles in Figure 3-7, while calculated mode frequencies based on Eq. (3.1) are plotted as red lines. With no CuPc at the interface, the calculated resonant frequencies correspond to the odd order modes of the 200nm Al film, as expected for the Al/Si structure ($Z_{Al}/Z_{Si} < 1$). The addition of the CuPc layer ($Z_{Al}/Z_{CuPc} > 1$) shifts the resonant frequencies toward the even order modes of the Al film (f_{Al}, black dashed lines), which is captured by the measurement as well.

The Fourier spectra of acoustic transients are further lined up with calculated mode frequencies and illustrated in Figure 3-8. For certain CuPc thicknesses (at which the solid red line crosses the dashed black line), the resonant modes of the Al/CuPc bilayer line up with f_{Al}. At these thicknesses, the CuPc layer acts as a quarter-wavelength ($\lambda/4$) resonant reflector, greatly increasing the amplitude of the measured mode. Resembling a Fabry-Pérot etalon in a laser cavity, the CuPc film thereby selects one or several modes from the relatively broadband comb of resonances excited by the

femtosecond laser pulse. This mode control can be observed in the time domain as well: in Figure 3-4, for example, 18 nm and 50 nm CuPc films select the 2nd and 1st mode respectively, and the selected mode then dominates the ringing of the resonator after the first ~ 250 ps.

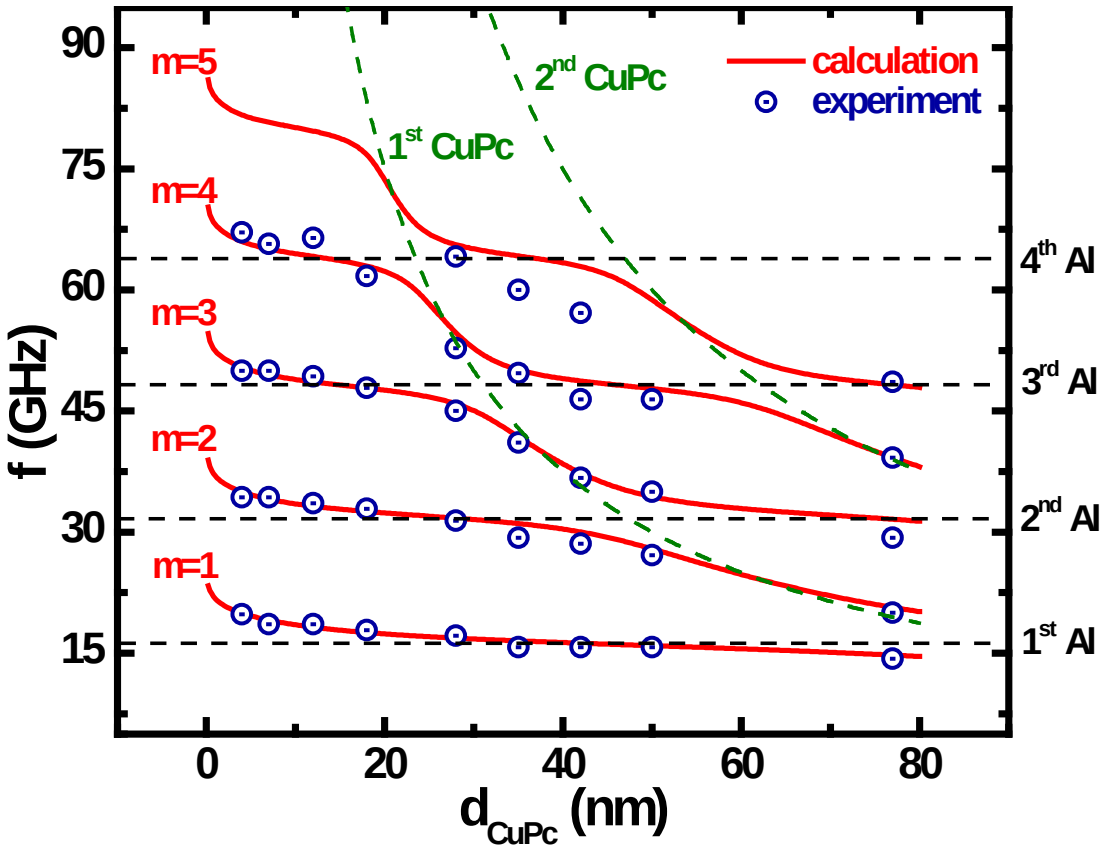

Figure 3-7 Measured and calculated resonant frequencies of Al/CuPc films on Si. Dashed lines represent the natural frequencies of a free-standing 200 nm thick Al film (black) and a free-standing CuPc film (green). All measured points have an error of ± 0.7 GHz which is caused by the finite temporal range of the acoustic transients [46].

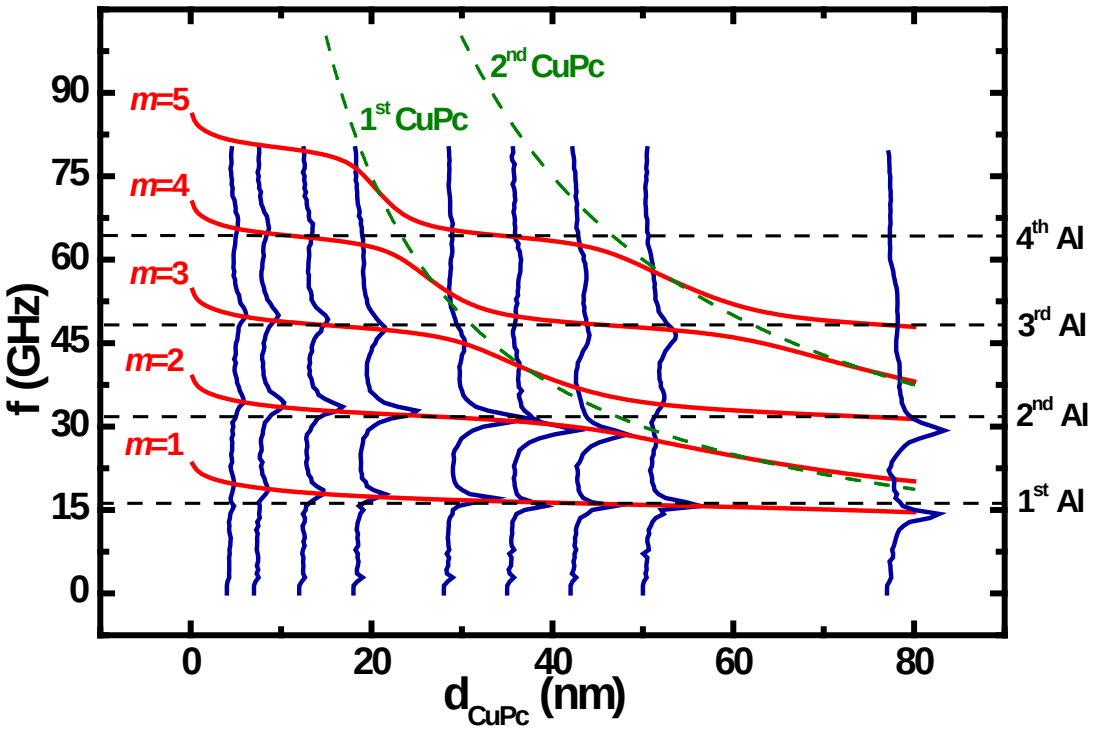

Figure 3-8 FFT of acoustic transients (blue curves) lined up with calculated resonant mode frequencies (red curves) [46].

A transfer matrix method is used to calculate the acoustic reflectivity of a CuPc film sandwiched between an Al film and a Si substrate (Figure 3-7).

$$R_{\mathrm{Al/CuPc/Si}} = \frac{\left(r_{\mathrm{Al/CuPc}} + r_{\mathrm{CuPc/Si}}\right)^2 - 4r_{\mathrm{Al/CuPc}}r_{\mathrm{CuPc/Si}}\sin^2\left(\frac{\pi}{2}\frac{d_{\mathrm{CuPc}}}{\lambda_{\mathrm{CuPc}}}\right)}{\left(1 + r_{\mathrm{Al/CuPc}}r_{\mathrm{CuPc/Si}}\right)^2 - 4r_{\mathrm{Al/CuPc}}r_{\mathrm{CuPc/Si}}\sin^2\left(\frac{\pi}{2}\frac{d_{\mathrm{CuPc}}}{\lambda_{\mathrm{CuPc}}}\right)} \tag{3.2}$$

where λ_{CuPc} is the wavelength of the acoustic wave in CuPc, and λ_{CuPc} is smaller than λ_{Al} since wavelength scales with the speed of sound. Figure 3-9 compares the measured FFT magnitude of each mode to the calculated CuPc film reflectivity, demonstrating that the layer selectively confines certain modes within the cavity through acoustic interference. For example, when $d_{\mathrm{CuPc}}/\lambda_{\mathrm{CuPc}}$ equals 0.25 or 0.5, the CuPc layer acts as a quarter-

wavelength or half-wavelength coating, respectively. The fact that the amplitudes of modes are observed to grow at the beginning with increasing CuPc thickness suggests that effects of surface and bulk attenuation are insignificant compared to the effect of coherent reflection at the cavity boundaries. The time-domain data (Figure 3-4) also shows that the ringing lasts longer as the CuPc thickness increases, indicating a higher quality factor *Q*.

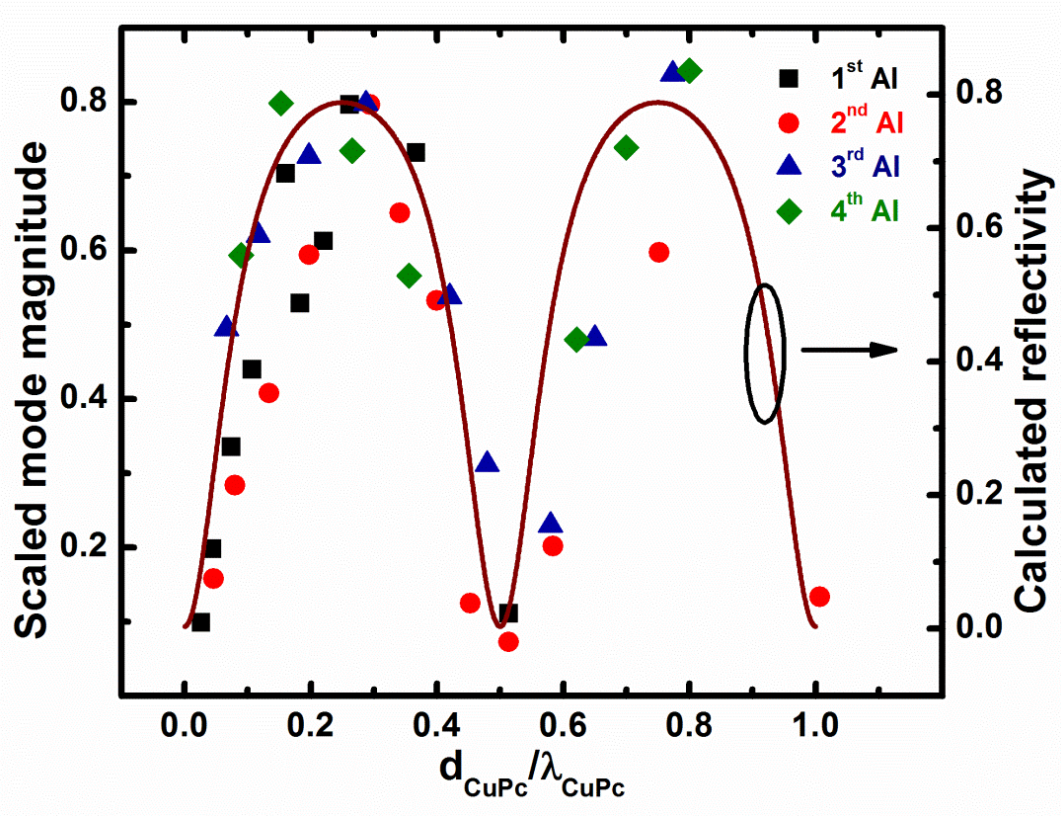

Figure 3-9 Measured magnitudes for modes (scattered dots) in the vicinity of the corresponding free-standing Al film resonances versus the ratio of CuPc film thickness to the mode wavelength in CuPc. Also shown is the acoustic reflectivity of the CuPc film calculated using Eq. (3.2). Note that each series (1st Al, 2nd Al, etc.) is scaled by its maximum magnitude because the initial energy distribution in each mode from laser pulse excitation, which could set a baseline for each mode, is not readily accessible [46].

3.3.2 FDTD calculation

To demonstrate the role of the CuPc layer as an acoustic etalon, we employ a finite-difference time-domain (FDTD) method to compute the displacement field of each resonant mode within the Al/CuPc bilayer (Figure 3-10). In this technique, we keep constant-amplitude stress at the Al film surface, oscillating the surface position at a certain frequency, and we then calculate the corresponding standing wave at this frequency that remains when all transients have decayed to zero. We finally sweep a wide range of frequency to generate the map of displacement distribution.

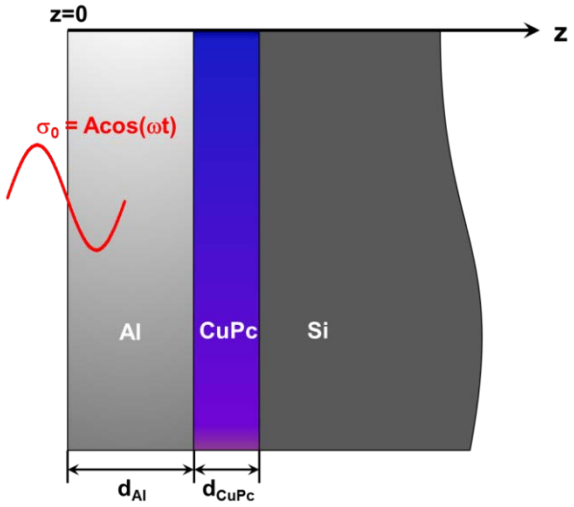

Figure 3-10 Al/CuPc/Si structure for FDTD simulation.

The general governing equation for acoustic wave propagation in an isotropic elastic medium (*i*) is given by Eq. (1.2); in our one-dimensional case (along the direction normal to the film plane, *z*) this can be simplified to:

$$\frac{\partial^2 u_i}{\partial t^2} = v_i^2 \frac{\partial^2 u_i}{\partial z^2} \tag{3.3}$$

The constant-amplitude stress at the Al surface at angular frequency ω is given by:

$$\sigma_{Al}\Big|_{z=0} = \rho_{Al} v_{Al}^2 \frac{du_{Al}}{dz}\Big|_{z=0} = A\cos(\omega t) \tag{3.4}$$

where for simulation purposes, the amplitude of the sinusoidal stress is assumed to be 1 MPa, which is a realistic value for laser-excited stress in Al. The boundary conditions that require continuous displacement and stress at the Al/CuPc and CuPc/Si interfaces are:

$$u_{Al}\Big|_{z=d_{Al}} = u_{CuPc}\Big|_{z=d_{Al}} \tag{3.5}$$

$$u_{CuPc}\Big|_{z=d_{Al}+d_{CuPc}} = u_{Si}\Big|_{z=d_{Al}+d_{CuPc}} \tag{3.6}$$

$$\rho_{Al} v_{Al}^2 \frac{\partial u_{Al}}{\partial z}\Big|_{z=d_{Al}} = \rho_{CuPc} v_{CuPc}^2 \frac{\partial u_{CuPc}}{\partial z}\Big|_{z=d_{Al}} \tag{3.7}$$

$$\rho_{CuPc} v_{CuPc}^2 \frac{\partial u_{CuPc}}{\partial z}\Big|_{z=d_{Al}+d_{CuPc}} = \rho_{Si} v_{Si}^2 \frac{\partial u_{Si}}{\partial z}\Big|_{z=d_{Al}+d_{CuPc}} \tag{3.8}$$

For the thick Si substrate that can be viewed as semi-infinite, a non-reflecting boundary condition for the acoustic wave is employed at a certain depth δ_{Si} into Si (this depth does not have a strict value as long as the simulation converges; here we use δ_{Si} = 50 μm) [73]:

$$\left(\frac{\partial u_{Si}}{\partial t} - v_{Si}\frac{\partial u_{Si}}{\partial z}\right)\Big|_{z=d_{Al}+d_{CuPc}+\delta_{Si}} = 0 \tag{3.9}$$

Figure 3-11 plots displacement profiles of the standing waves in the frequency range of 10 – 55 GHz for cavities with four different CuPc thicknesses. We can identify all resonant modes by tracing the frequencies for which the amplitude of the standing wave is locally maximized. We find that the resonant frequencies identified by this FDTD method are identical to the values obtained from Eq. (3.2), which partially validates the FDTD simulation. The contour plots show that acoustic modes occur near the even-order natural frequencies of Al (16 GHz, 32 GHz, 48 GHz, etc.) in samples with

CuPc (Figure 3-11(b)-(d)) and near the odd-order natural frequencies of Al (24 GHz, 40 GHz, etc.) in samples without CuPc (Figure 3-11(a)). The mode strengths in Figure 3-11(a) are reduced by the low impedance mismatch between Al and Si. In Figure 3-4 the resonances near the even order modes appear as 17.9, 32.9, 47.9, and 61.7 GHz (m = 1, 2, 3, 4) in the 18 nm CuPc sample; 15.7, 35.0, 46.4, and 58.9 GHz (m = 1, 3, 4, 5) in the 50 nm CuPc sample; and 14.3, 29.3, and 48.6 GHz (m = 1, 3, 5) in the 77 nm CuPc sample (all values +/- 0.7 GHz). At these resonances, the acoustic energy is rather evenly distributed in the Al and CuPc films, and the CuPc layer selects modes of the Al resonator through constructive or destructive interference.

In Figure 3-11(c) and Figure 3-11(d) we have predicted additional resonant modes between adjacent natural resonances of the Al membrane (for example, 28 GHz for the 50 nm CuPc sample, and 20 GHz and 38 GHz for the 77 nm CuPc sample). These frequencies are close to the Fabry-Pérot resonances of the CuPc layer itself, and at these modes of the cavity, the acoustic energy is primarily confined within the CuPc etalon rather than in Al. Figure 3-5 also confirms the presence of these additional modes, where a peak at 27.9 GHz (m = 2) is observed in the 50 nm CuPc sample and two lesser peaks near 20 GHz (m = 2) and 39 GHz (m = 4) are weakly visible in the 77 nm CuPc sample. Figure 3-12 gives a more intuitive illustration of the instantaneous displacement profile.

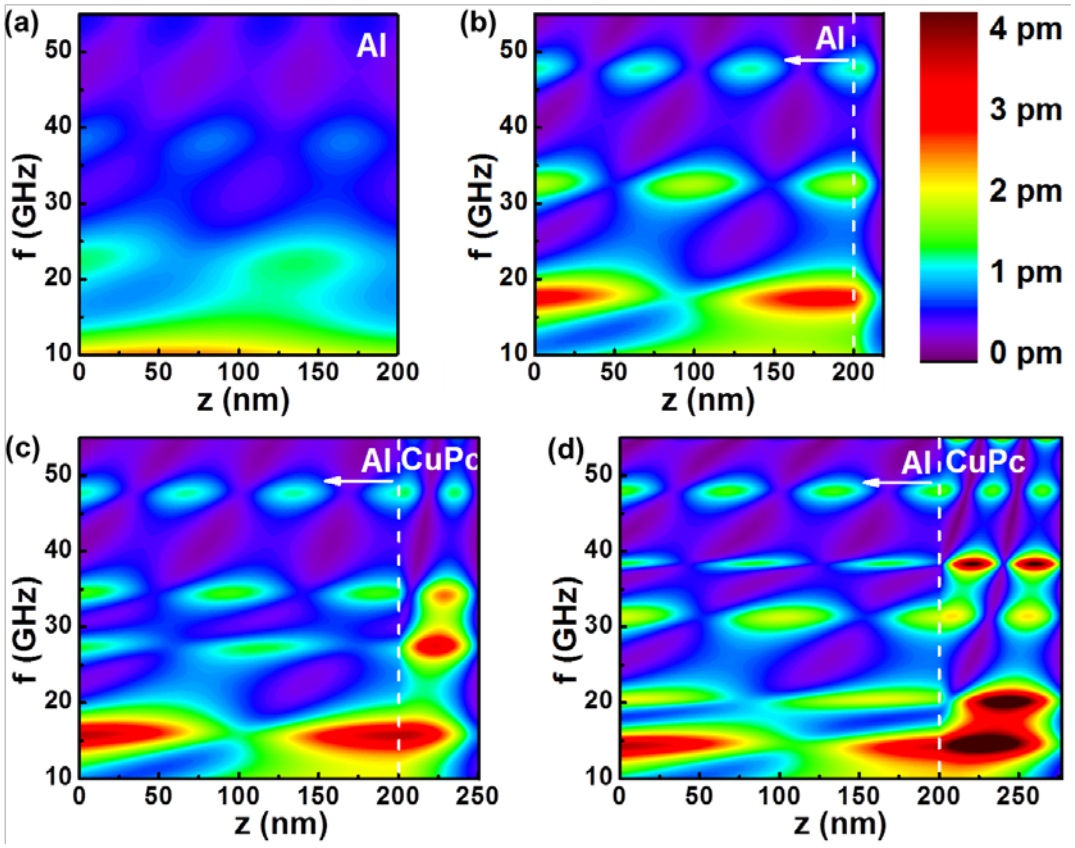

Figure 3-11 Calculated displacement contours for (a) no CuPc layer, (b) 18 nm CuPc layer, (c) 50 nm CuPc layer, and (d) 77 nm CuPc layer. Colorbar unit: picometer (pm), 10^{-12} m [46].

For an optical etalon placed within the cavity of a solid state laser, a similar buildup of circulating energy occurs within the etalon at its Fabry-Pérot resonances; the etalon can be tilted so that cavity modes adjacent to these resonances are reflected out of the cavity, thus achieving mode selection (Figure 3-1). Like its optical analog, the CuPc-based acoustic etalon selects the modes at its Fabry-Pérot resonances, acting as a bandpass filter for acoustic waves near these frequencies and thereby allowing a standing wave at these frequencies to develop in the cavity defined by the air/Al and CuPc/Si interfaces. In this way the etalon introduces its own resonances into the spectrum of the membrane resonator; for modes far away from these "etalon" resonances, the acoustic

energy is rather evenly distributed in the Al and CuPc films, and the CuPc layer selects modes of the Al transducer by promoting constructive or destructive interference of these modes.

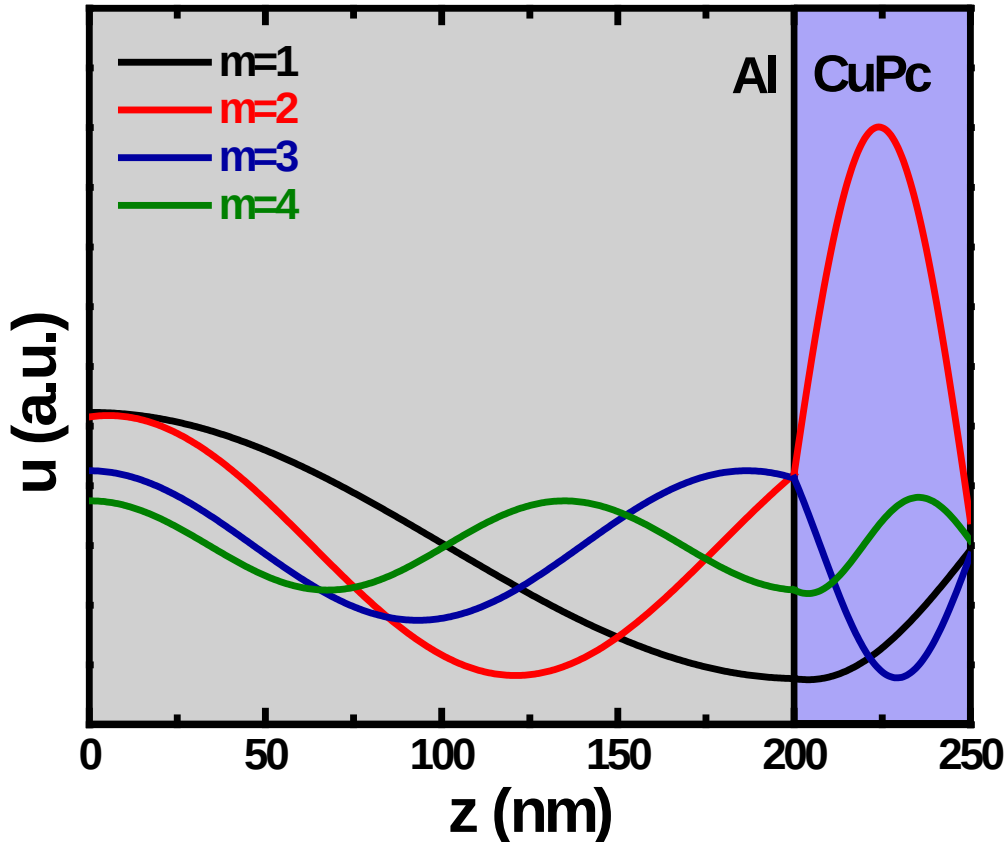

Figure 3-12 Calculated instantaneous displacement profiles of different modes in the 50 nm CuPc sample.

3.3.3 "Dual" resonators

We further investigate the roles of acoustic etalons in coherent control of resonant acoustic spectra by including multiple resonator and etalon films. As illustrated in Figure 3-13, Sample A is the same 50 nm CuPc sample as shown in Figure 3-5. Sample B has a thin Al resonator on top of a 50 nm CuPc etalon; the fundamental resonance is shifted to 31.2 GHz, for which the 50 nm etalon is not reflective, and hence the mode leaks out of

the cavity and does not appear in the spectrum. Sample C uses both a thin Al resonator and a thin etalon, causing the reflection band of the etalon to include the fundamental resonance of the resonator, and the mode therefore again appears in the spectrum. Sample D uses a thick Al resonator, a thin Al resonator, and two thick etalons. The fundamental resonance of the thin Al layer falls outside the reflection band of the thick etalon (as in Sample B), so it does not appear. Meanwhile, the thin Al film is close to half the thickness of the top thick Al film and thus acts as a resonant reflector. The mode of the thick Al resonator is therefore strengthened compared to Sample A, as it sits on three quarter-wave reflectors. Sample E uses two thick Al resonators of slightly different thickness and two thick etalons as well. In this case each etalon acts as a resonant reflector for the fundamental mode of each corresponding Al film, so the two resonators are both activated, with two peaks present in the spectrum that correspond to their resonant modes. In this sample the acoustic spectrum of a coupled oscillator system is controlled. It is worth noting that the modes of both the top and buried resonators are present while the measurement only probes the top Al surface. We need a significantly more sophisticated model to fully understand the acoustic response of such dual-resonator samples. We preliminarily attribute the red shifts observed relative to the natural (unloaded) Al film resonances in Samples D and E to mass loading by the relatively heavy buried Al layer.

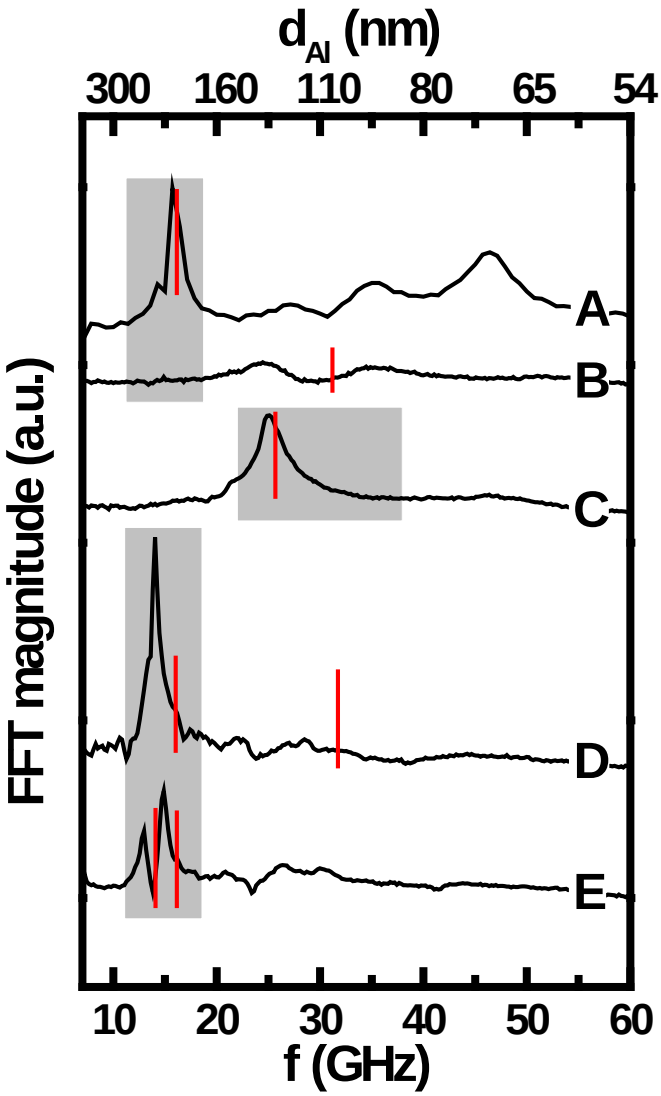

Figure 3-13 Fourier spectra of acoustic transients for Samples A-E with the following layer structures from top to bottom grown on Si substrates: A) 200nm Al / 50nm CuPc; B) 103nm Al / 50nm CuPc; C) 125nm Al / 25nm CuPc; D) 200nm Al / 50nm CuPc / 103nm Al / 50nm CuPc; E) 200nm Al / 50nm CuPc / 222nm Al / 50nm CuPc. The bottom x-axis shows the fundamental resonant frequency for a free-standing Al film of the thickness given on the top x-axis. The short red lines indicate the actual Al thicknesses in each sample. The shaded regions indicate the reflection band of the CuPc etalon(s) in each sample, which we define as the frequency range for which the etalon's acoustic reflectivity is above 0.75 [46].

3.4 Conclusion

By inserting a compliant supporting layer at the interface between a metal transducer and a stiff substrate, we have formed a supported membrane resonator that allows multiple harmonic modes to persist simultaneously. The acoustic dynamics of such a system differ fundamentally from the echo behavior typically observed in optical pump-probe measurements of thin films [54,61,64]. Since the compliant organic layer forms part of the acoustic cavity, its thickness can be varied to promote constructive or destructive interference of the membrane's resonant modes, thereby permitting coherent control and mode selection analogous to an optical etalon in a laser cavity. To our knowledge this has been the first experimental demonstration of a thin film acoustic etalon.

Furthermore, we have demonstrated strong confinement of acoustic energy afforded by the etalon at its own resonances. Given a sufficiently broadband input, the acoustic etalon can add these resonances to the system. If we include multiple resonators and etalons within a layer stack, significant control over the acoustic dynamics of the system can be achieved, which supports future investigations of coupled high-frequency acoustic oscillators, stimulated emission of phonons, acoustic mode switching, and the elastic properties of thin films.

Chapter 4

Perturbation analysis of the effect of interface roughness on acoustic phonon transport

As mentioned in Chapter 1 and demonstrated in Chapter 3, layered thin film structures have the capability to manipulate the transport of acoustic phonons [9-11]. This affords numerous possibilities for applications in coherent acoustic phonon generation [74,75] and heat management [76-78].

Unlike photons, acoustic phonons relevant for terahertz (THz) acoustic devices and thermal transport have wavelengths of the order of a few nanometers. For this reason, interface roughness even on the atomic scale is expected to have much more significant impact on acoustic phonon transport than it does for light propagation at optical wavelengths.

4.1 Previous work

The interface roughness effect on wave scattering has been theoretically and experimentally investigated in numerous contexts, including visible and infrared light [79], X-ray radiation [80], etc. In regard to heat transfer at rough interfaces, a parameter referred to as specularity [77,81-83] has been employed to interpolate between

the acoustic mismatch model (AMM) and the diffuse mismatch model (DMM) [19]. AMM and DMM are the two primary classic models for thermal boundary conductance, and define limits to phonon boundary scattering that are fully specular and fully diffuse, respectively. An alternative treatment is to divide a rough interface into multiple flat facets (e.g., a fractal structure) and assume specular scattering at each facet [84]. Neither of these methods accounts for phonon mode conversion at the interface, limiting the calculations to each individual phonon polarization. Recently more complex computational tools such as molecular dynamics [85] and Green's function formulations [86] have been used to calculate phonon scattering at rough interfaces or nanostructured surfaces. Nevertheless, these tools are restricted to certain roughness profiles that may be unrealistic due to computational limitations. In addition, none of the approaches mentioned above can conveniently separate the specular and diffuse parts of scattered (transmitted and reflected) phonons, which are of critical importance to acoustic devices as well as interfacial heat transfer applications.

In addition to the above techniques, analytical perturbation analyses have been used to characterize modified boundary conditions at rough interfaces and model the effects of such fluctuations in interface positions. A rough interface is described by statistical parameters such as the out-of-plane root-mean-square (RMS) roughness (which represents the standard deviation of interface height), and the in-plane correlation length (which for a polycrystalline material interface can be considered as a representation of the average grain size). In this approach it is relatively straightforward to include phonon mode conversion and separate the specular and diffuse components. Ref. 87 calculated the effect of surface roughness on phonon transport at a copper/helium interface with a

first-order boundary perturbation method. Ref. 88 extended this model to estimate the contribution of surface roughness to the thermal boundary conductance at this same interface. The boundary perturbation approach was later applied to acoustic wave scattering at rough interfaces in stratified elastic media, the ice-water boundary being one example [89]. For acoustic waves, however, the solid-fluid interface investigated in these models is fundamentally different from a solid-solid interface; for example, fluidic media do not support transverse waves as solids do.

In this work we extend the boundary perturbation analysis to a rough solid-solid interface [90]. Given a longitudinal or transverse wave incident at a particular angle on an interface with a specified roughness profile, the angular distribution of waves emitted by the interface is predicted. The phonon mode conversion and loss of coherence are calculated in a straightforward way. In addition, interface evanescent modes are predicted.

4.2 Perturbation method for a solid-solid interface

The mathematical model presented below is an extension of perturbation analysis [89] to rough solid-solid interfaces, and is based on the following assumptions: (1) acoustic phonons can be mathematically treated as plane waves (see Chapter 1), (2) the two solids in contact to form the interface are elastic and isotropic, (3) the scattering is elastic so no anharmonic effects occur at the interface, and (4) all scattering occurs in the plane of incidence for simplicity (yet can be further extended to three-dimensional cases). Therefore, the model applies to GHz or THz acoustic phonon devices and heat transfer at low temperatures.

Acoustic waves have three different modes (polarizations): longitudinally polarized waves that are commonly referred to as "L" waves, transverse (shear) waves polarized in the plane of incidence (shear vertical or "SV" waves), and transverse waves polarized normal to the plane of incidence (shear horizontal or "SH" waves). These modes can couple with each other under certain circumstances, for example, at an oblique angle of incidence or at a nanostructured interface. The boundary conditions for acoustic plane waves require continuity of displacement and stress, which are in general more complex than those for electromagnetic waves because of the mode coupling between the three polarizations. Phonon reflection and transmission can then be derived from such boundary conditions.

Here we employ the wave potential for mathematical derivations instead of the displacement used in Chapter 1 (the advantages of this approach will be later apparent). The total acoustic phonon wave potential ψ contains the information of both the amplitude and phase of a plane wave propagating in different directions on either side of the interface, and can be decomposed into [89]:

$$\psi = \langle \psi \rangle + s \tag{4.1}$$

Here $\langle \psi \rangle$ is the mean field, representing the specular part of transmitted or reflected energy; its direction of propagation obeys Snell's law. s is the quasi-diffuse field, representing the energy component scattered from the interface roughness; its directional distribution depends on wavelength, roughness profile, and the acoustic impedances of both materials. The term "quasi-diffuse" is used to indicate that the directional distribution of the field is not random. A schematic of wave scattering with an L wave incident at a rough interface is illustrated in Figure 4-1.

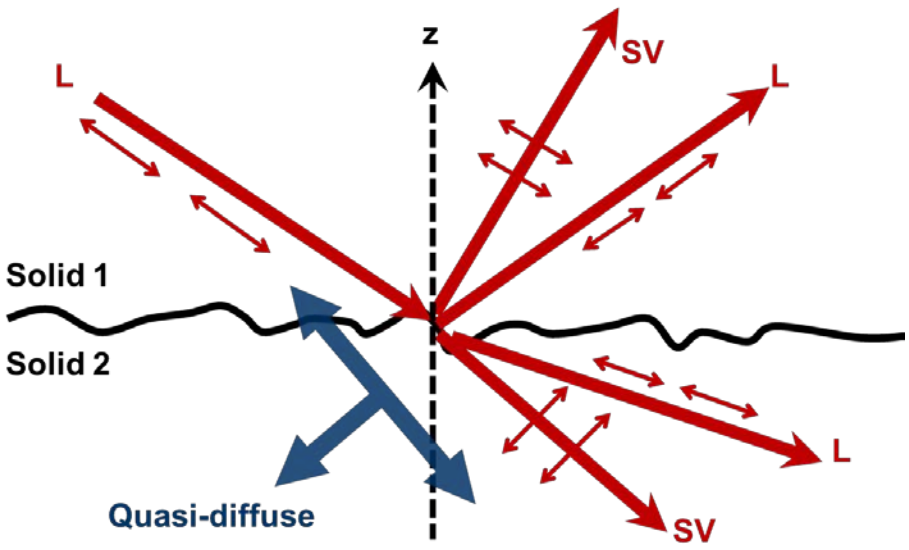

Figure 4-1 Outgoing wave components including (specular) reflected L and SV modes, (specular) transmitted L and SV modes, and quasi-diffuse field, with an L mode incident at a rough interface.

The total wave potential can be Fourier transformed to an integral form in terms of the in-plane wavevector **k**, which represents the component of the total wavevector that lies in the interface plane:

$$\psi = \frac{1}{2\pi}\int d^2\mathbf{k} e^{-j\mathbf{k}\cdot\mathbf{r}}\left[\tilde{\psi}^-(\mathbf{k})e^{-\alpha z} + \tilde{\psi}^+(\mathbf{k})e^{\alpha z}\right] \tag{4.2}$$

where **r** is the position vector, $\alpha = \sqrt{k^2 - K_m^2}$ is the out-of-plane wavenumber with k=|**k**| being the in-plane wavenumber, and K_m is the total wavenumber of a specific mode (L, SV, or SH). $\tilde{\psi}^-(\mathbf{k})$ and $\tilde{\psi}^+(\mathbf{k})$ are potentials of plane waves moving toward the -z and +z directions, respectively, and z is the axis normal to the interface plane.

The scattered component *s* is zero for a flat interface, and the boundary condition for the wave potential can then be expressed as:

$$\tilde{B}(\mathbf{k})\tilde{\psi}^{\mp}(\mathbf{k}) = 0 \tag{4.3}$$

where $\tilde{B}(\mathbf{k})$ is the solid-solid boundary condition matrix obtained by matching the out-of-plane and in-plane components of displacements and stresses. $\tilde{\psi}^{\mp}(\mathbf{k})$ is a vector that contains the wave potentials of different modes traveling in both -z and +z directions. When the incident wave is ain L or SV mode, L-SV mode coupling can occur at the interface, and the relevant wave potential vector can be expanded as:

$$\tilde{\psi}^{\mp}_{L-SV}(\mathbf{k}) = \left[\tilde{\psi}^{-}_{L,1} \quad \tilde{\psi}^{-}_{SV,1} \quad \tilde{\psi}^{+}_{L,1} \quad \tilde{\psi}^{+}_{SV,1} \quad \tilde{\psi}^{-}_{L,2} \quad \tilde{\psi}^{-}_{SV,2} \quad \tilde{\psi}^{+}_{L,2} \quad \tilde{\psi}^{+}_{SV,2}\right]^{T} \tag{4.4}$$

The L-SV boundary operator that couples an input L or SV wave into an output of L and SV waves is given by

$$\tilde{B}_{L-SV}(\mathbf{k}) = \begin{bmatrix} -\alpha_{L,1} & k & \alpha_{L,1} & k & \alpha_{L,2} & -k & -\alpha_{L,2} & -k \\ -jk & j\alpha_{SV,1} & -jk & -j\alpha_{SV,1} & jk & -j\alpha_{SV,2} & jk & j\alpha_{SV,2} \\ \mu_1\left(2k^2 - K^2_{SV,1}\right) & -2\mu_1 k\alpha_{SV,1} & \mu_1\left(2k^2 - K^2_{SV,1}\right) & 2\mu_1 k\alpha_{SV,1} & -\mu_2\left(2k^2 - K^2_{SV,2}\right) & 2\mu_2 k\alpha_{SV,2} & -\mu_2\left(2k^2 - K^2_{SV,2}\right) & -2\mu_2 k\alpha_{SV,2} \\ 2j\mu_1 k\alpha_{L,1} & -j\mu_1\left(2k^2 - K^2_{SV,1}\right) & -2j\mu_1 k\alpha_{L,1} & -j\mu_1\left(2k^2 - K^2_{SV,1}\right) & -2j\mu_2 k\alpha_{L,2} & j\mu_2\left(2k^2 - K^2_{SV,2}\right) & 2j\mu_2 k\alpha_{L,2} & j\mu_2\left(2k^2 - K^2_{SV,2}\right) \end{bmatrix} \tag{4.5}$$

The subscripts L and SV denote the wave mode, and 1 and 2 refer to the two solid media on either side of the interface. $\alpha_L = \sqrt{k^2 - K_L^2}$ and $\alpha_{SV} = \sqrt{k^2 - K_{SV}^2}$ represent the complex out-of-plane wavenumbers of the L and SV modes, respectively, and μ is the shear modulus. Each column in the matrix of $\tilde{B}_{L-SV}(\mathbf{k})$ consists of the coefficients of a specific wave potential listed in Equation (4.4). Columns 1-4 correspond to material 1 and columns 5-8 correspond to material 2. The matrix elements are derived from boundary continuity equations of the normal displacement, tangential displacement, normal stress, and tangential stress, respectively. Similarly, the boundary operator for an

incident SH mode (which does not couple to L or SV modes for a 2D roughness profile) can be obtained:

$$\tilde{B}_{SH}(\mathbf{k}) = \begin{bmatrix} k & k & -k & -k \\ -2\mu_1 k\alpha_{SH,1} & 2\mu_1 k\alpha_{SH,1} & 2\mu_2 k\alpha_{SH,2} & -2\mu_2 k\alpha_{SH,2} \end{bmatrix} \tag{4.6}$$

The interface roughness can be treated as a perturbation of both height and slope (or angle) to the boundary condition for a perfectly flat interface. The perturbed boundary condition is then given by [89]:

$$\left(\tilde{B}(\mathbf{k}) + \frac{\sigma^2}{2}\frac{\partial^2}{\partial z^2}\tilde{B}(\mathbf{k}) + I_1(\mathbf{k}) + I_2(\mathbf{k}) \right) \left\langle \tilde{\psi}^{\mp}(\mathbf{k}) \right\rangle = 0 \tag{4.7}$$

where σ is the RMS roughness and $I_1(\mathbf{k})$ and $I_2(\mathbf{k})$ are integrals over $\mathbf{q}$, which is the in-plane wavevector of the outgoing wave. The integral forms are given by [89]:

$$I_1(\mathbf{k}) = -\frac{\sigma^2}{2\pi}\int d^2\mathbf{q} P(\mathbf{q}-\mathbf{k}) \frac{\partial \tilde{B}(\mathbf{q})}{\partial z} \times \tilde{B}^{-1}(\mathbf{q}) \left(\frac{\partial \tilde{B}(\mathbf{k})}{\partial z} - j(\mathbf{q}-\mathbf{k}) \cdot \tilde{b}(\mathbf{k}) \right) \tag{4.8}$$

$$I_2(\mathbf{k}) = -\frac{\sigma^2}{2\pi}\int d^2\mathbf{q} P(\mathbf{q}-\mathbf{k}) \cdot j(\mathbf{q}-\mathbf{k}) \cdot \tilde{b}(\mathbf{q}) \times \tilde{B}^{-1}(\mathbf{q}) \left(\frac{\partial \tilde{B}(\mathbf{k})}{\partial z} - j(\mathbf{q}-\mathbf{k}) \cdot \tilde{b}(\mathbf{k}) \right) \tag{4.9}$$

The depth derivatives $\frac{\partial \tilde{B}(\mathbf{k})}{\partial z}$ are obtained by multiplying the columns of the boundary matrix operator $\tilde{B}(\mathbf{k})$ with their corresponding out-of-plane wavenumbers. For example, the first element in the first column of $\frac{\partial \tilde{B}_{L-SV}(\mathbf{k})}{\partial z}$ should be multiplied by $-\alpha_{L,1}$, with the direction of wave propagation reflected in the sign. The second derivatives $\frac{\partial^2 \tilde{B}(\mathbf{k})}{\partial z^2}$ can be subsequently derived in the same way.

P in Equations (4.8) and (4.9) is the Fourier transform of the spatial representation of the interface roughness. For a Gaussian roughness profile, $P(\mathbf{q}) = \sqrt{2\pi} l e^{-q^2 l^2/2}$ where l is the in-plane correlation length. $\tilde{b}(\mathbf{k})$ is the rotation boundary operator, and for L-SV mode coupling:

$$\tilde{b}_{L-SV}(\mathbf{k}) = \begin{bmatrix} jk & -j\alpha_{SV,1} & jk & j\alpha_{SV,1} \\ -\alpha_{L,1} & k & \alpha_{L,1} & k \\ -4j\mu_1 k\alpha_{L,1} & 2j\mu_1\left(2k^2 - K_{SV,1}^2\right) & 4j\mu_1 k\alpha_{L,1} & 2j\mu_1\left(2k^2 - K_{SV,1}^2\right) \\ 2\mu_1\left(2k^2 - K_{L,1}^2\right) & -4\mu_1 k\alpha_{SV,1} & 2\mu_1\left(2k^2 - K_{L,1}^2\right) & 4\mu_1 k\alpha_{SV,1} \end{bmatrix} \\ \begin{bmatrix} -jk & j\alpha_{S,2} & -jk & -j\alpha_{SV,2} \\ \alpha_{L,2} & -k & -\alpha_{L,2} & -k \\ 4j\mu_2 k\alpha_{L,2} & -2j\mu_2\left(2k^2 - K_{SV,2}^2\right) & -4j\mu_2 k\alpha_{L,2} & -2j\mu_2\left(2k^2 - K_{SV,2}^2\right) \\ -2\mu_2\left(2k^2 - K_{L,2}^2\right) & 4\mu_2 k\alpha_{SV,2} & -2\mu_2\left(2k^2 - K_{L,2}^2\right) & -4\mu_2 k\alpha_{SV,2} \end{bmatrix} \tag{4.10}$$

$\tilde{B}(\mathbf{q})$ and $\tilde{b}(\mathbf{q})$ are square matrices that consist of the columns of $\tilde{B}(\mathbf{k})$ and $\tilde{b}(\mathbf{k})$ and correspond to outgoing waves, with $\mathbf{k}$ replaced by $\mathbf{q}$. $\tilde{B}^{-1}(\mathbf{q})$ is simply the inverse of $\tilde{B}(\mathbf{q})$.

It should be noted that the forms given above are generalized. Therefore, for a specific incident wave mode, only components pertaining to the relevant incoming and outgoing modes need to be reserved in the vector $\tilde{\psi}^{\mp}(\mathbf{k})$ as well as in each boundary operator. For example, an incident L wave ($\tilde{\psi}_{L,1}^{-}$) will produce reflected L ($\tilde{\psi}_{L,1}^{+}$), reflected SV ($\tilde{\psi}_{SV,1}^{+}$), transmitted L ($\tilde{\psi}_{L,2}^{-}$), and transmitted SV ($\tilde{\psi}_{SV,2}^{-}$) waves. $\tilde{\psi}_{L-SV}^{\mp}(\mathbf{k})$ in Equation (4.4) will hence reduce to a 4-component vector with elements 2-6, and the matrices in Equations (4.5) and (4.10) will reduce to 4×5 matrices with columns 2-6.

Next we solve Equation (4.7) to obtain the amplitudes of the specular components ($\langle \tilde{\psi}^{\mp}(\mathbf{k}) \rangle$) of outgoing longitudinal and transverse plane waves and hence the specular

transmission and reflection coefficients for a single rough interface. As Equation (4.7) is a generalized formula in terms of the spatial dimension as well as the perturbation, this method can be adapted to any type of interface roughness profile (e.g., Gaussian, sawtooth) by appropriate calculation of $\tilde{B}(\mathbf{k})$, $\tilde{b}(\mathbf{k})$, and P.

In addition to the specular components of reflected/transmitted waves, a quasi-diffuse field that spans a range of in-plane wavevectors **q** is generated from a single mode wave with in-plane wavevector **k** incident on a rough interface. We can use the solved mean (specular) field $\langle \tilde{\psi}^{\mp}(\mathbf{k}) \rangle$ from Equation (4.7) to calculate the expectation value of the power density of this quasi-diffuse field:

$$\langle \tilde{s}(\mathbf{q}) \tilde{s}^{*}(\mathbf{q}) \rangle = \frac{\sigma^2}{2\pi} P(\mathbf{q}-\mathbf{k}) \left| \tilde{B}^{-1}(\mathbf{q}) \left(\frac{\partial \tilde{B}(\mathbf{k})}{\partial z} - j(\mathbf{q}-\mathbf{k}) \cdot \tilde{b}(\mathbf{k}) \right) \langle \tilde{\psi}^{\mp}(\mathbf{k}) \rangle \right|^2 \quad (4.11)$$

4.3 Numerical examples

4.3.1 Ge/Si interfaces

As discussed above, we are able to separately obtain the specular and quasi-diffuse parts of the total wave potential using Equations (4.7) and (4.11). The interface specularity p (see Section 4.1), which represents the probability of specular scattering, is defined by:

$$T = pT_{AMM} + (1-p)T_{DMM} \quad (4.12)$$

In our perturbation analysis p can be obtained by computing the ratio of the specular component of the transmitted energy at a rough interface to the transmitted energy when the interface is flat. Figure 4-2 plots calculated p using the boundary

perturbation formula developed above, along with the prediction of a Green's function method [86]. The specularity p is averaged over incident angle and shown to reduce with increasing angular frequency. This results from the fact that the scattering of acoustic waves is perturbed to a greater extent at wavelengths that approach the roughness length scale (5.4 Å). In general, the boundary perturbation method utilizes the Taylor series expansion of the unperturbed boundary, and in our case is based on a power series in $(\sigma/\lambda)^2$. The model described above (e.g., Equation (4.7)) uses a second-order approximation that is accurate for $\lambda > 6\sigma$ (corresponding to the $\omega < 0.5$ region in the normalized units of Figure 4-2), beyond which higher orders are necessary. One commonly adapted expression for interface specularity was first developed by Ziman and considers the phase difference of phonons resulting from the interface roughness [77,81-83]:

$$p = \exp\left(\frac{-16\pi^2\sigma^2}{\lambda^2}\right) \tag{4.13}$$

p from Equation (4.13) is also displayed in Figure 4-2 for comparison. It is found to differ greatly from the predictions of the boundary perturbation and Green's function approaches, because it assumes normal incidence and does not incorporate phonon mode conversion.

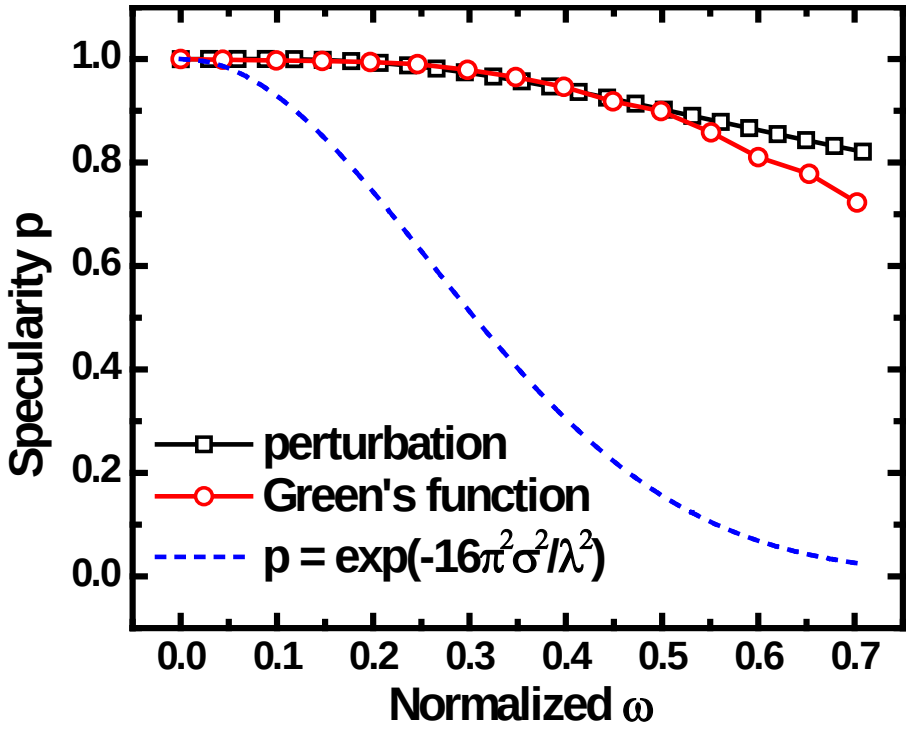

Figure 4-2 Calculated interface specularity for a rough Si/Ge interface using the boundary perturbation approach developed in this chapter and a Green's function method [86]. The angular frequency is normalized by the factor $\sqrt{F/m}$, where F is the force constant associated with the Si-Si bond and m is the atomic mass of Si [86,91]. Also shown is the specularity calculated from the commonly used Equation (4.13) [83]. All three models use the same interface RMS roughness (5.4 Å) [90].

We illustrate the strength of mode conversion and the strong dependence of phonon scattering on incident angle at a rough interface in Figure 4-3, which plots the specular components of the L and SV waves reflected and transmitted when an SV wave is incident on a Ge/Si interface from the Ge side. Here we assume Gaussian roughness with σ = 3 Å in the plane of incidence, and assume densities and longitudinal and transverse wave velocities of 5323 kg/m^3, 4920 m/s, and 3550 m/s for germanium and 2329 kg/m^3, 8430 m/s, and 5845 m/s for silicon, respectively [92]. Analogous to optical scattering, critical angles are present for the transmitted L wave, reflected L wave, and transmitted SV wave, beyond which the wave field cuts off to zero. This is because the

incident SV wave in Ge has the lowest acoustic velocity. The interface roughness reduces the specular reflectivity and transmissivity for each mode at all angles, which has been experimentally observed by picosecond ultrasounics [93]. We note that this specular reduction is significant even for an interface with such atomic-scale roughness, and the effect could be greater given the limit of interface smoothness by current fabrication techniques. This observation has technological implications; for example, interface roughness compromises the efficiency of acoustic devices such as phonon Bragg mirrors/filters and acoustic modulators. In addition, we find that changes in the in-plane correlation length do not significantly impact the degree of reduction in the specular field, which agrees with previous findings [86]. Therefore, a constant value of l = 100 Å is used for the calculations shown in Figure 4-3, Figure 4-4, and Figure 4-5.

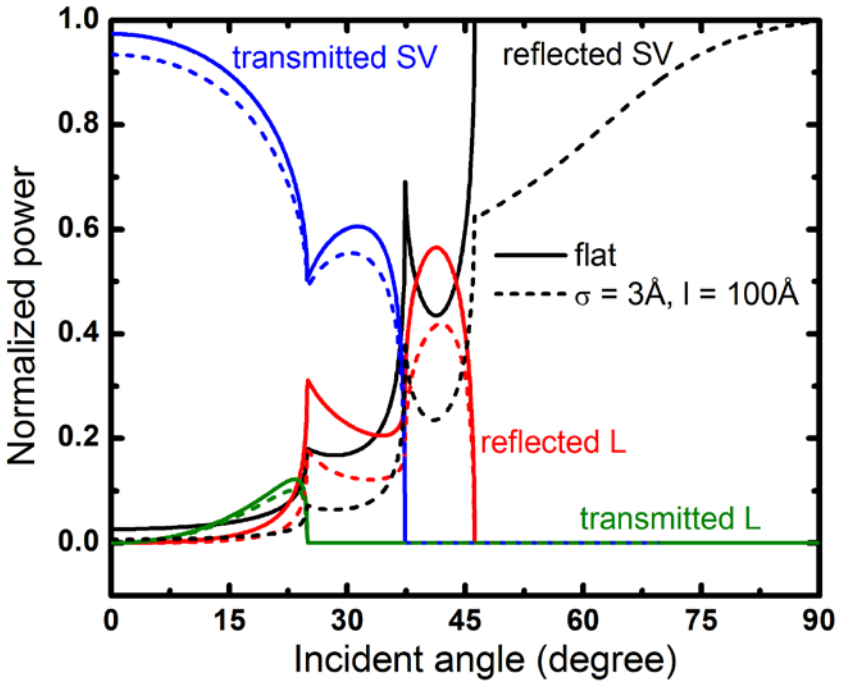

Figure 4-3 Calculated specular reflectivity and transmissivity for flat (solid line) and rough (dashed line) Ge/Si interfaces as a function of incident f = 1 THz SV wave angle (defined with respect to the interface normal). Values are normalized to the power of the incident wave. An RMS roughness of 3 Å and a correlation length of 100 Å are used for the rough interface [90].

While the incident SV mode does not make specular conversions to reflected L, transmitted L, or transmitted SV modes beyond respective critical angles, it does couple to these modes through quasi-diffuse scattering at all angles. Figure 4-4(a) illustrates this coupling, showing the power of the quasi-diffuse field (integrated over all in-plane wavenumbers, or outgoing angles) for the same interface as a function of the incident angle of the SV wave. The emission pattern of the quasi-diffuse wave is illustrated in Figure 4-4(b), which shows its power density as a function of outgoing in-plane wavenumbers from a SV wave incident at 30° on the Ge/Si interface.

As seen in Figure 4-4(b), the field scattered by interface roughness is not entirely diffuse, but rather is centered near the incident in-plane wavenumber with a certain range of spread. A more intuitive picture of this scattering is given by Figure 4-4(c), which shows the actual angular distribution of each scattered mode. The finding that the scattered field is non-randomly distributed in angle has scientific implications for interfacial heat transfer, as the DMM model discussed above assumes that the emission of phonons by interface roughness scattering is angle-independent. To investigate the dependence of the scattered field on physical properties of the interface, we allow the material density on the incident side (e.g., the Ge density) to be a variable and thus alter its acoustic impedance and show the results in Figure 4-5. In general, the acoustic impedance mismatch is found to strongly affect the amplitude of the quasi-diffuse field distribution and weakly influence its shape and peak in-plane wavenumber. The features in Figure 4-4(b) and Figure 4-5 near 0.745 nm^{-1} and 1.075 nm^{-1} correspond to critical angles for longitudinal and transverse waves in silicon, respectively (similar features appear in Figure 4-6).

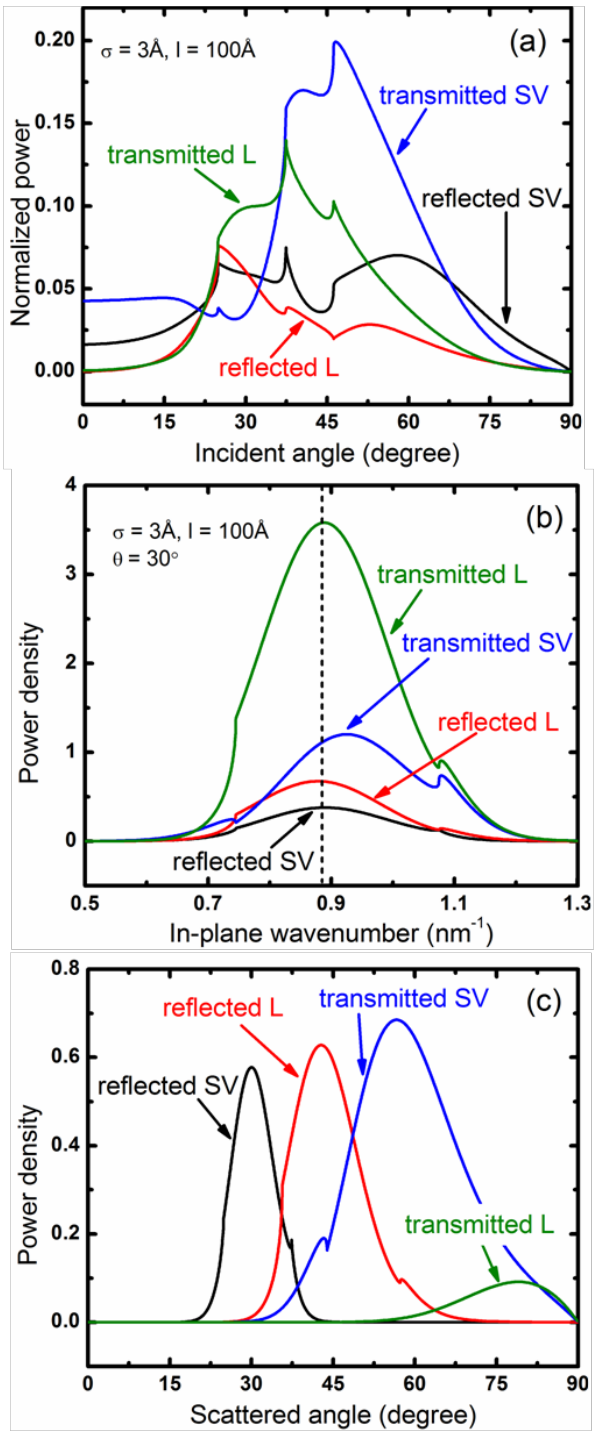

Figure 4-4 (a) Calculated power of the quasi-diffuse field (normalized by the power of the incident SV wave at f = 1 THz) generated by scattering at a rough Ge/Si interface as a function of the incident angle of the SV wave. (b) Calculated power density of the quasi-diffuse field as a function of outgoing in-plane wavenumber. (c) Calculated power density of the quasi-diffuse field as a function of outgoing angle. We assume a 30° incident SV wave for (b) and (c). The dashed line in (b) locates the in-plane wavenumber of the incident wave [90].

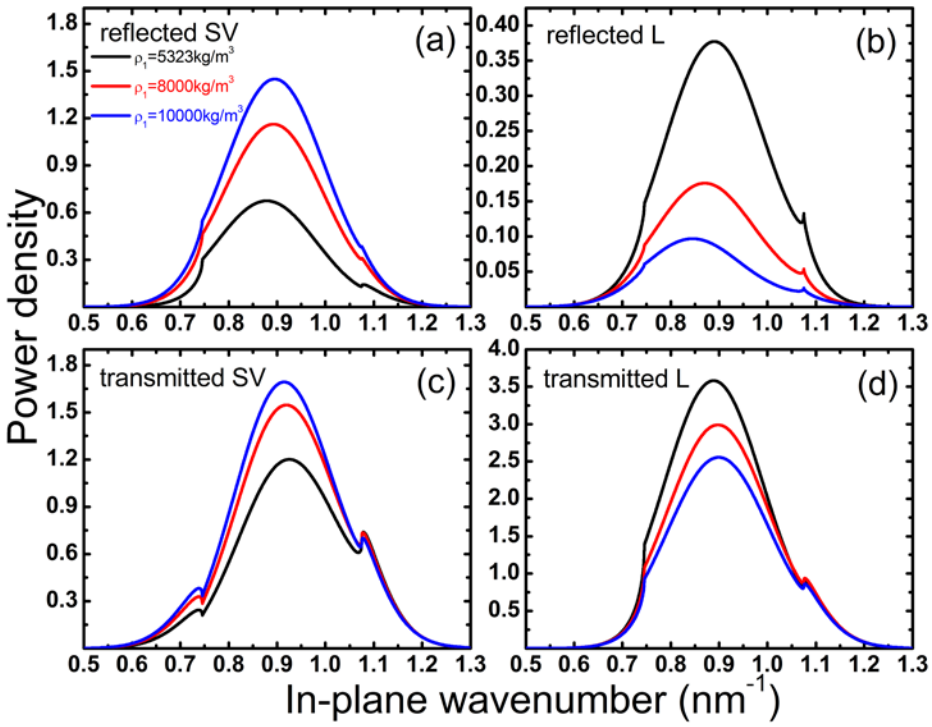

Figure 4-5 Calculated power density of quasi-diffuse field (normalized by the power of the incident 30° SV wave at $f = 1$ THz) generated by scattering at rough interfaces with varied densities of material 1 (Ge), as a function of outgoing in-plane wavenumber: (a) reflected SV mode, (b) reflected L mode, (c) transmitted SV mode, (d) transmitted L mode [90].

4.3.2 Interface modes

In addition to bulk waves that propagate in the solid media, the excitation of interface acoustic waves by roughness can be predicted by the model developed here. Interface modes are supported under a range of combinations of acoustic velocities and material densities [94]. Here we demonstrate interface mode excitation using the material pair of fused silica and yttrium aluminum garnet (YAG) [92], which is commonly used in fiber lasers and fulfills the conditions listed in [94]. As shown in Figure 4-6(a), the incident L wave from the fused silica side couples to a mode near 1.322 nm^{-1} that is greater than the total wavenumber (1.053 nm^{-1}) and thus is evanescent. This mode has an

acoustic phase velocity of 4760 m/s and is known to be an attenuated interface wave mode that leaks energy away from the interface as it propagates along it [94]. Such interface waves have the ability to convert to bulk waves that carry energy and impact interfacial thermal transport properties [95]. Figure 4-6(b) shows that a greater incident angle can lead to stronger coupling or energy conversion of an incident L mode to this interface mode. The link between interface mode characteristics and interface roughness profiles remains under investigation.

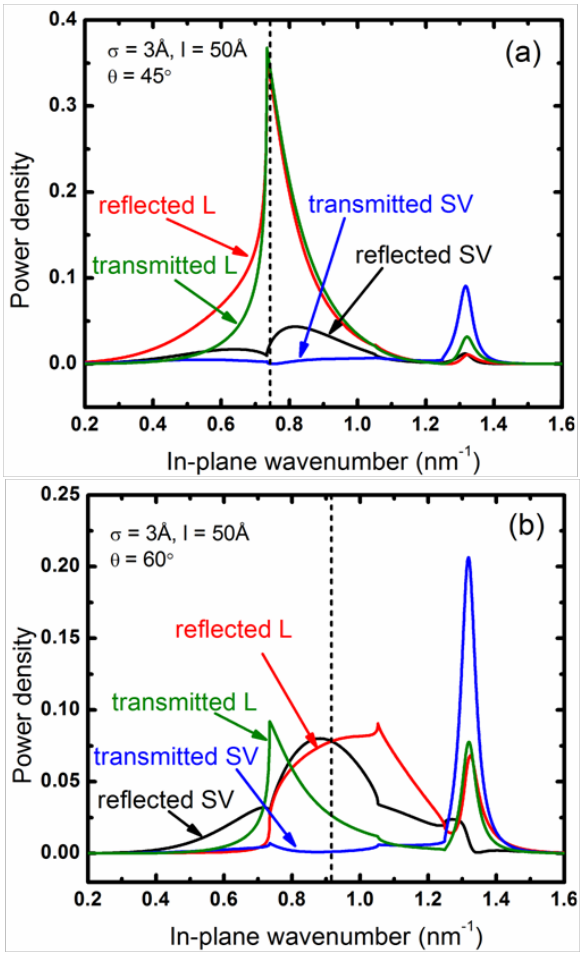

Figure 4-6 Calculated power density of the quasi-diffuse field generated by scattering of an f = 1 THz L wave incident at (a) $\theta = 45°$ and (b) $\theta = 60°$ on a rough fused silica/YAG interface. An RMS roughness of 3 Å and correlation length of 50 Å (which couples more energy to interface modes than the 100 Å correlation length used in previous figures) are assumed. The dashed line indicates the corresponding in-plane wavenumber of the incident L wave [90].

4.4 Superlattices

This perturbation approach has advantages in that it can be readily extended to multilayer thin films. In this section we develop an approach that couples boundary perturbation methods and transfer matrices to model the transport of phonons at rough interfaces in superlattices, predicting the effects of roughness geometry and incident phonon angle on phonon mode conversion and loss of coherence as well as providing quantitative analysis of the relative contributions of acoustic impedance contrast and interface flatness to superlattice reflectivity. This work has important scientific and technological implications in coherent phonon generation, stimulated phonon emission, nanoscale heat transfer, and acoustic filter applications.

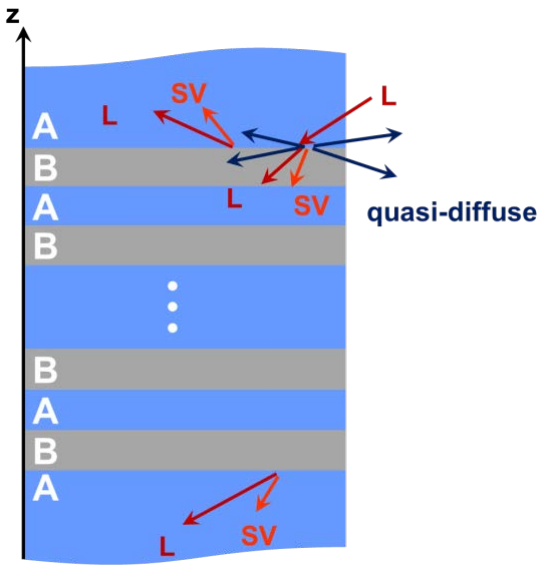

Figure 4-7 Schematic of acoustic phonon scattering with an incident L wave in a superlattice with rough interfaces.

We adopt a transfer matrix approach that takes into account coherent phonon phase and calculate the phonon transport in a roughened superlattice structure of the form $(A/B)_N$. Figure 4-7 shows schematics of the modeling system and the acoustic wave

scattering in this structure. Here we consider L-SV mode coupling and write the mean (specular) phonon field within each layer i in terms of four components:

$$\left\langle \tilde{\psi}_i^{\mp}(\mathbf{k}) \right\rangle = \begin{bmatrix} \left\langle \tilde{\psi}_{L,i}^{-}(\mathbf{k}) \right\rangle \\ \left\langle \tilde{\psi}_{SV,i}^{-}(\mathbf{k}) \right\rangle \\ \left\langle \tilde{\psi}_{L,i}^{+}(\mathbf{k}) \right\rangle \\ \left\langle \tilde{\psi}_{SV,i}^{+}(\mathbf{k}) \right\rangle \end{bmatrix} \tag{4.14}$$

In Section 4.3 we obtained the reflection and transmission properties of a single rough interface; we can now explicitly rewrite the fields immediately on either side of the interface between layers i and i+1 in terms of a 4×4 interface transfer matrix $T_{\text{int},i;i+1}$:

$$\left\langle \tilde{\psi}_{i+1}^{\mp}(\mathbf{k}) \right\rangle = T_{\text{int},i\to i+1} \left\langle \tilde{\psi}_i^{\mp}(\mathbf{k}) \right\rangle \tag{4.15}$$

Similarly, the field can be calculated after it has propagated through layer i with thickness d_i according to a propagation matrix $T_{\text{prop},i}$:

$$\left\langle \tilde{\psi}_{i,d_i}^{\mp}(\mathbf{k}) \right\rangle = T_{\text{prop},i} \left\langle \tilde{\psi}_{i,0}^{\mp}(\mathbf{k}) \right\rangle \tag{4.16}$$

where

$$T_{\text{prop},i} = \begin{bmatrix} e^{-\alpha_{L,i}d_i - jkd_i\tan(\theta_{L,i})} & & & \\ & e^{-\alpha_{SV,i}d_i - jkd_i\tan(\theta_{SV,i})} & & \\ & & e^{\alpha_{L,i}d_i - jkd_i\tan(\theta_{L,i})} & \\ & & & e^{\alpha_{SV,i}d_i - jkd_i\tan(\theta_{SV,i})} \end{bmatrix} \tag{4.17}$$

and $\theta_{L,i}$ and $\theta_{SV,i}$ are the incident angles of L and SV waves.

The mean phonon field after propagating through one period of the superlattice (layers i and i+1) is then given by:

$$\left\langle \tilde{\psi}_{i+2}^{\mp}(\mathbf{k}) \right\rangle = T_{\text{period}} \left\langle \tilde{\psi}_i^{\mp}(\mathbf{k}) \right\rangle \tag{4.18}$$

where the transfer matrix for one period of unit is:

$$T_{\text{period}} = T_{\text{int},i+1\to i+2} T_{\text{prop},i+1} T_{\text{int},i\to i+1} T_{\text{prop},i} \tag{4.19}$$

For a unit amplitude L wave with in-plane wavevector $\mathbf{k}$ incident on the superlattice, the acoustic field in the first layer can be written as

$$\left\langle \tilde{\psi}_1^{\mp}(\mathbf{k}) \right\rangle = \begin{bmatrix} 1 \\ 0 \\ \left\langle \tilde{\psi}_{L,1}^{+}(\mathbf{k}) \right\rangle \\ \left\langle \tilde{\psi}_{SV,1}^{+}(\mathbf{k}) \right\rangle \end{bmatrix} \tag{4.20}$$

and the acoustic field in the last layer is then

$$\left\langle \tilde{\psi}_{2N+1}^{\mp}(\mathbf{k}) \right\rangle = \begin{bmatrix} \left\langle \tilde{\psi}_{L,2N+1}^{-}(\mathbf{k}) \right\rangle \\ \left\langle \tilde{\psi}_{SV,2N+1}^{-}(\mathbf{k}) \right\rangle \\ 0 \\ 0 \end{bmatrix} \tag{4.21}$$

These two fields are related by the transfer matrices as

$$\left\langle \tilde{\psi}_{2N+1}^{\mp}(\mathbf{k}) \right\rangle = T_{\text{period}}^{N} \left\langle \tilde{\psi}_1^{\mp}(\mathbf{k}) \right\rangle \tag{4.22}$$

Now the four unknown wave amplitudes $\left\langle \tilde{\psi}_{L,1}^{+}(\mathbf{k}) \right\rangle$, $\left\langle \tilde{\psi}_{SV,1}^{+}(\mathbf{k}) \right\rangle$, $\left\langle \tilde{\psi}_{L,2N+1}^{-}(\mathbf{k}) \right\rangle$, $\left\langle \tilde{\psi}_{SV,2N+1}^{-}(\mathbf{k}) \right\rangle$ can be solved to obtain the specular L and SV modes reflected and transmitted by the rough superlattice.

As an example, we consider a superlattice composed of repeated periods of $SrTiO_3$ and $BaTiO_3$ with layer thicknesses of $3\lambda/4$ and $\lambda/4$, respectively. This type of structure has been shown [56,96] to act as an acoustic phonon Bragg reflector with a stop band centered at $f = v/\lambda$, where the wavelength λ and sound velocity v are both material dependent. Assumed values of density and longitudinal and transverse (shear) acoustic velocities are 6020 kg/m^3, 7850 m/s, and 4800 m/s for $SrTiO_3$ and 5130 kg/m^3, 5420 m/s,

and 2400 m/s for $BaTiO_3$ [96,97]. In our simulation, the center frequency of the phonon stop band is chosen to be 1 THz. Correspondingly, the layer thicknesses for $SrTiO_3$ and $BaTiO_3$ are 40.7 Å and 19.7 Å respectively.

Figure 4-8 shows the calculated specular longitudinal phonon (L mode) reflectivity at normal incidence of a 20-period $SrTiO_3/BaTiO_3$ superlattice as a function of frequency for different interface roughnesses. An RMS roughness of 5 Å is predicted to reduce the reflectivity by 44% and furthermore reduce the full width half maximum of the stop band by 42%.

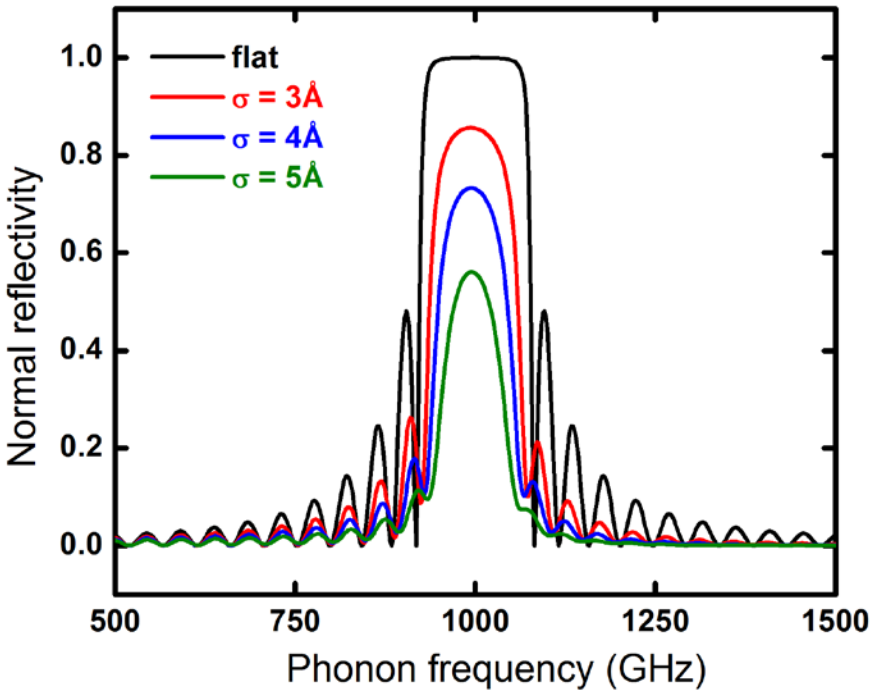

Figure 4-8 Calculated specular longitudinal phonon reflectivity at normal incidence of a 20-period $SrTiO_3/BaTiO_3$ superlattice with flat (black curve) and rough (colored curves) interfaces, as a function of the incident phonon frequency. RMS roughness values of 3 Å, 4 Å, and 5 Å and a correlation length of 100 Å are used, these values being typical of superlattices grown by molecular beam epitaxy [85,96].

As shown in Figure 4-9, the reflectivity at the center of the stop band (1 THz) increases with the number of periods, reaching an asymptotic value after approximately

20 periods. The reduction in reflectivity with interface roughness is closely related to the ratios between the interface roughness length scales and the phonon wavelength, i.e., σ/λ. As mentioned in Section 4.3, the dependence on the in-plane correlation length l is negligible.

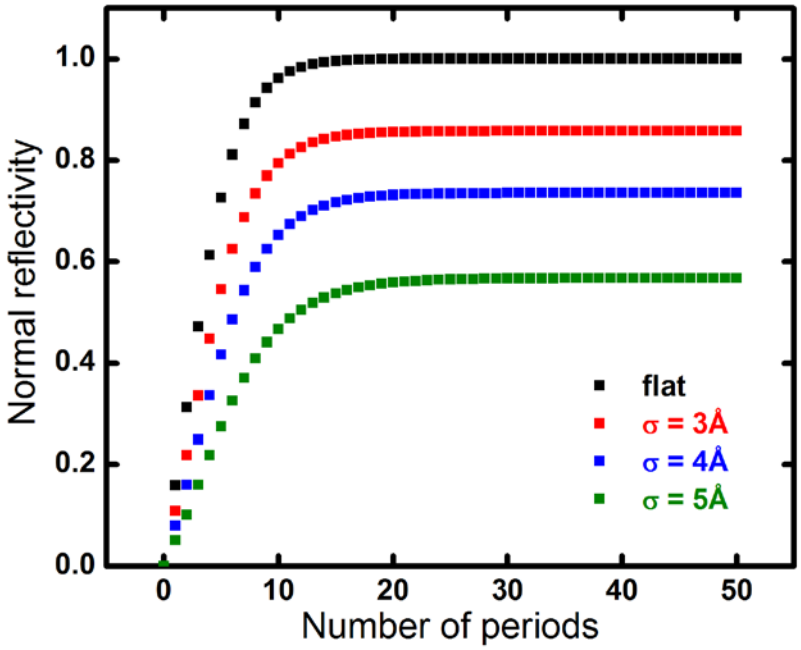

Figure 4-9 Calculated specular longitudinal phonon reflectivity at normal incidence and f = 1THz of a $SrTiO_3/BaTiO_3$ superlattice with flat (black) and rough (colored) interfaces, as a function of the number of superlattice periods.

To illustrate the effect of roughness on mode conversion, Figure 4-10 shows the specular power reflected (in SV and L modes) and transmitted (in SV and L modes) by the $SrTiO_3/BaTiO_3$ superlattice in response to an L wave incident at a particular angle. Phonon interference leads to oscillatory behavior that becomes indistinct for rough interfaces due to a loss of coherence as a result of scattering into a wide range of angles at multiple interfaces. This scattering is further illustrated in Figure 4-11, which shows how the total power of the quasi-diffuse field accumulates as more superlattice periods are

added. The scattered power peaks near 72°, which is consistent with the maximum phonon scattering predicted near 77° for a single rough interface.

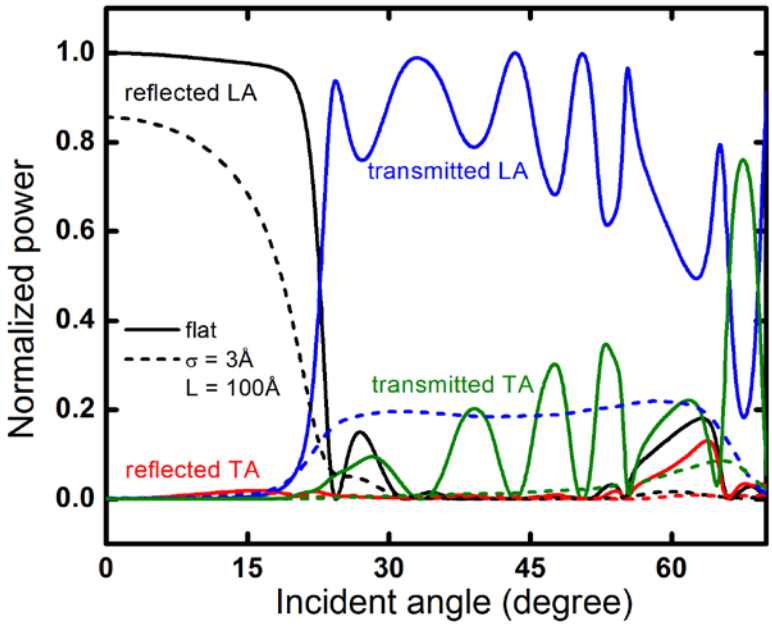

Figure 4-10 Calculated specular phonon reflectivity and transmissivity of flat (solid lines) and rough (dashed lines) 20-period $SrTiO_3/BaTiO_3$ superlattice, as a function of incident angle of the f = 1THz L wave.

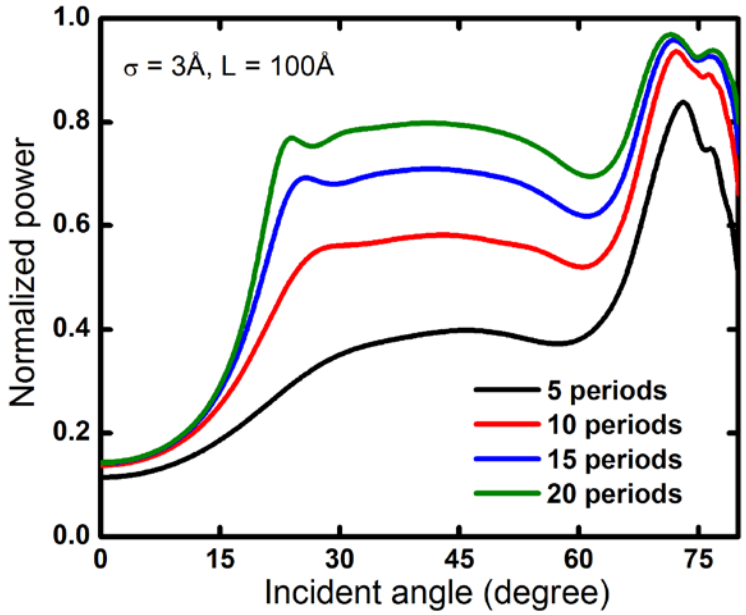

Figure 4-11 Calculated power of the quasi-diffuse field (normalized by that of the incident f = 1THz L mode) generated by scattering in a rough $SrTiO_3/BaTiO_3$ superlattice for different numbers of periods, as a function of L mode incident angle.

Reflection is achieved in a phonon Bragg mirror by a mismatch of the acoustic impedances of the two materials forming the superlattice; in general a high acoustic impedance contrast is desirable for high reflectivity. However, practical concerns that arise in material pairs with high acoustic impedance contrast (such as differences in lattice constant) may lead to increased interfacial roughness during superlattice fabrication. In such circumstances a tradeoff exists between increased reflectivity due to high acoustic contrast and decreased reflectivity due to interfacial roughness. To assess this tradeoff, we vary both parameters and show the effects on specular reflectivity in Figure 4-12. When varying the acoustic impedance contrast $Z_A / Z_B = \rho_A v_A / \rho_B v_B$, we fix the sound velocity ratio v_A / v_B as well as the density of material B (ρ_B) and allow ρ_B to change. For a given interface roughness profile, an optimal acoustic impedance ratio exists which produces maximum phonon reflectivity; this mapping could therefore serve as a quantitative guide to the design of a phonon Bragg mirror.

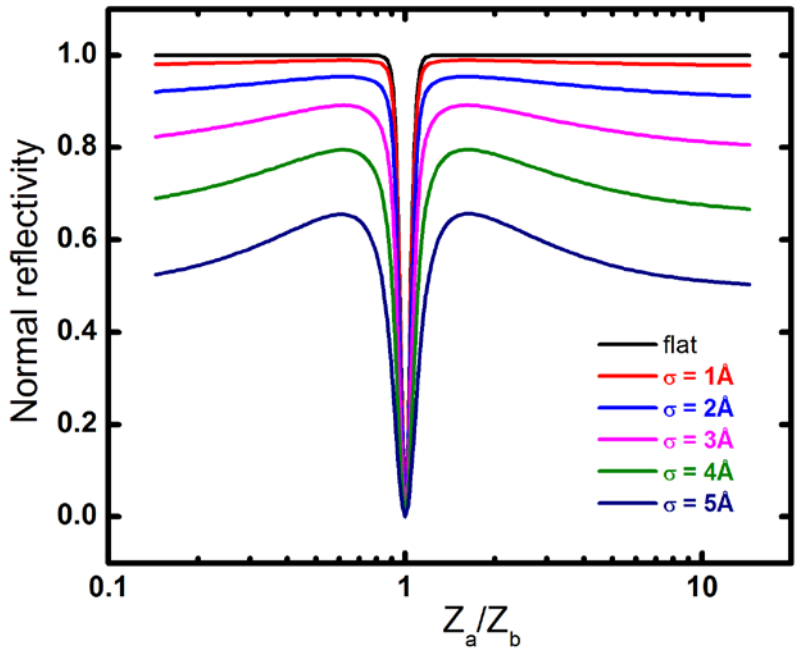

Figure 4-12 Calculated specular normal reflectivity at f = 1THz for a 20-period superlattice over a range of acoustic impedance contrasts and interface RMS roughnesses.

4.5 Conclusion

We have applied a boundary perturbation method to model acoustic wave transport at rough solid-solid interfaces, calculating the effects of interface roughness on mode conversion and scattered angle distribution. The presented method allows straightforward separation of specular and diffuse components that pertain to thermal boundary resistance and the performance of acoustic phonon devices. Furthermore, the effect of acoustic impedance mismatch on the distribution of scattered waves is quantitatively assessed, with this mismatch found to primarily govern the amplitude of the scattered radiation pattern rather than its shape. Interface specularity predictions agree well with a Green's function calculation [86] over the range of wavelengths for which the second-order boundary perturbation method is valid ($\lambda > 6\sigma$).

We further use the model to study the effect of interface roughness on the specular phonon reflectivity/transmissivity of a $SrTiO_3/BaTiO_3$ superlattice, which acts as an acoustic phonon Bragg mirror. Our results show a considerable reduction in phonon reflectivity compared to the case of an ideally flat interface. The boundary perturbation method developed here provides further understanding regarding the role of interface roughness on phonon reflectivity in multilayer thin films, and contributes guidance for the design and fabrication of multilayer acoustic phonon devices.

Chapter 5

Picosecond acoustic characterization of roughened interfaces

The fundamental origin of thermal boundary resistance (TBR) is the reflection and scattering of heat-carrying (primarily acoustic) phonons at an interface. Below 1 K, TBR can be well explained by the acoustic mismatch model (AMM) because interface diffuse scattering is minimal at such low temperatures. However, AMM fails to predict TBR at higher temperatures; this deviation is known as the Kapitza anomaly [98-100]. A quantitative description that takes into account the mechanisms of specular and diffuse scattering at interfaces is essential to the fundamental understanding of the Kapitza anomaly, as well as loss in coherent phonon devices (Chapters 1 and 4). In Chapter 4 we have calculated the effects of interface roughness on coherent phonon transport in thin film layered structures. In this chapter we report some preliminary results of measured coherent phonon reflection as well as thermal conductance at roughened interfaces.

To our knowledge, few measurements have been performed to characterize the effect of interface roughness on phonon scattering. Ref. 101 reported the specular scattering probability of acoustic phonons at a crystal boundary by observing the loss in coherent phonon amplitude during reflection (Figure 5-1). It was found that even atomic-level roughness reduces specular scattering probability significantly. While that study focused on narrowband phonons generated through Brillouin scattering or multiple

quantum wells, here we characterize coherent phonon scattering by taking advantage of the broadband phonon waves generated by ultrafast laser excitation of an Al transducer.

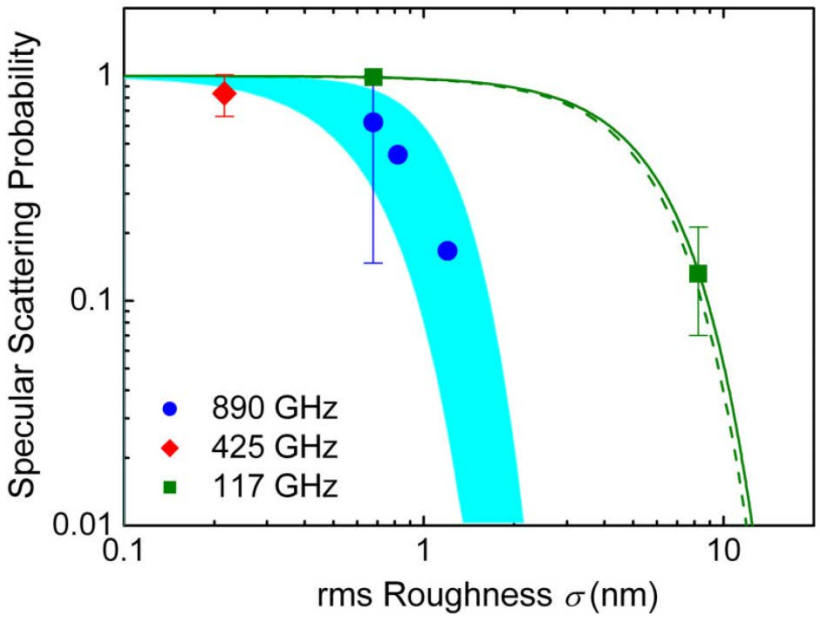

Figure 5-1 Experimentally determined (dots) specular scattering probability as a function of interface roughness at different frequencies. [101] The solid and dashed lines are predictions from a small slope approximation calculation [102].

5.1 Roughened interfaces

We first use chemical etching to roughen the surface of a fused silica glass slide. Figure 5-2 illustrates the sample preparation process. Hydrofluoric (HF) acid is used as the primary etchant. An ultrasonicator is used to enhance the etchant flow and facilitate the etching process. A thin (~ 5 nm) silver layer is deposited prior to the etching step. As chemical (wet) etching is in general an isotropic process, we utilize this deposition of a very thin metal film to form non-uniform islands on the glass surface; this discontinuous layer then serves as a partial etch mask to augment the etching non-uniformity and surface roughness. Three different samples are prepared at room temperature: Sample A

is a plain glass slide (Thermo Scientific) for baseline purposes, Sample B is etched in diluted HF acid (~ 16% concentration in water) for approximately 15 minutes, and Sample C is etched in undiluted HF acid (~ 48% concentration) for only 10 seconds. All three samples are then coated with 100 nm (measured by a crystal monitor) aluminum for optical pump-probe measurements.

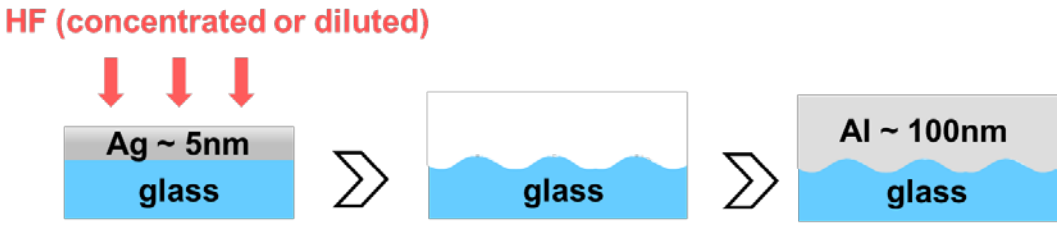

Figure 5-2 Chemical etching of glass and transducer film deposition.

The glass surfaces are characterized using an atomic force microscope (AFM) and the resulting topography images are shown in Figure 5-3. The measured root-mean-square (RMS) roughness values (σ_{RMS}) are listed in Table 5-1.

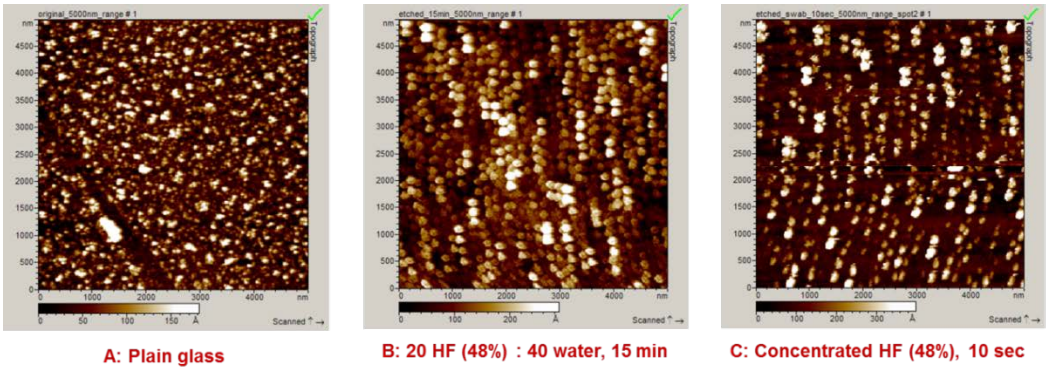

Figure 5-3 AFM tomography of glass samples.

Glass sample	A	B	C
σ_{RMS} (nm)	1.5	5.7	8.8

Table 5-1 RMS roughness for different samples.

The concentrated HF has a much higher etch rate, resulting in a rougher glass surface even with a very short time (10 seconds). Although a more comprehensive study is warranted, we expect that the etching process can be systematically improved. That is, by varying the assisting Ag layer thickness, the HF concentration, and the etch time, a series of samples with different roughnesses can be created. Buffered HF may also lead to more controllable etching.

5.2 Picosecond acoustics

Here we focus our study on the modification of coherent phonon transport properties at such purposely roughened interfaces. The picosecond acoustic transients measured with the ASOPS system (Chapter 2) are shown in Figure 5-4. The acoustic echoes are clearly visible in Figure 5-4(b) (arrow-pointed on curve A). The first echo near 15 ps is due to the electron-excited strain wave at the Al/glass interface traveling to the Al surface [21]. The second echo near 30 ps corresponds to the first round trip of the strain wave generated at the Al surface. In a similar fashion, acoustic echoes from the front-surface and interface excitations are indicated with solid and dashed line arrows, respectively. The interface excitations are relatively weak for several reasons: 1) the laser pulse energy is primarily contained near the front surface; 2) electrons lose energy to the lattice when traveling diffusively across the Al film; and 3) strain generation relies on an elastic discontinuity at the interface, but the acoustic impedance mismatch between Al and glass is relatively small. The acoustic transport properties derived in this study are calculated based on the front-surface generated strain waves.

The acoustic echoes appear to have a nearly anti-symmetric shape, which is induced by the initial strain wave reflecting at the air/Al boundary. Al as a transducer has a positive piezo-optic coefficient, meaning that the optical reflectance increases when Al is heated and expands. When the "positive" strain wave reflects from an interface with a softer (lower acoustic impedance) medium, the reflected wave picks up a phase shift of π. Conversely, there is no phase shift for the wave reflecting from an interface in contact with a harder (higher acoustic impedance) medium. The echo shapes as seen in Figure 5-4(b) can be interpreted by counting the relevant acoustic reflections.

It is worth mentioning that with a constant incident pump laser power, the initial spikes in $\Delta R/R$ due to electron heating have exactly the same height and rise time for all three samples. AFM characterizations also indicate very similar surface morphologies of coated Al films (σ_{RMS} within ±1 nm) on the glass slides. These observations suggest that there is no difference among samples in the optical excitation by the pump pulse or in the optical detection by the probe pulse; the observed changes in $\Delta R/R$ from Samples A to C originate solely from the variations of the acoustic reflection at the Al/glass interface.

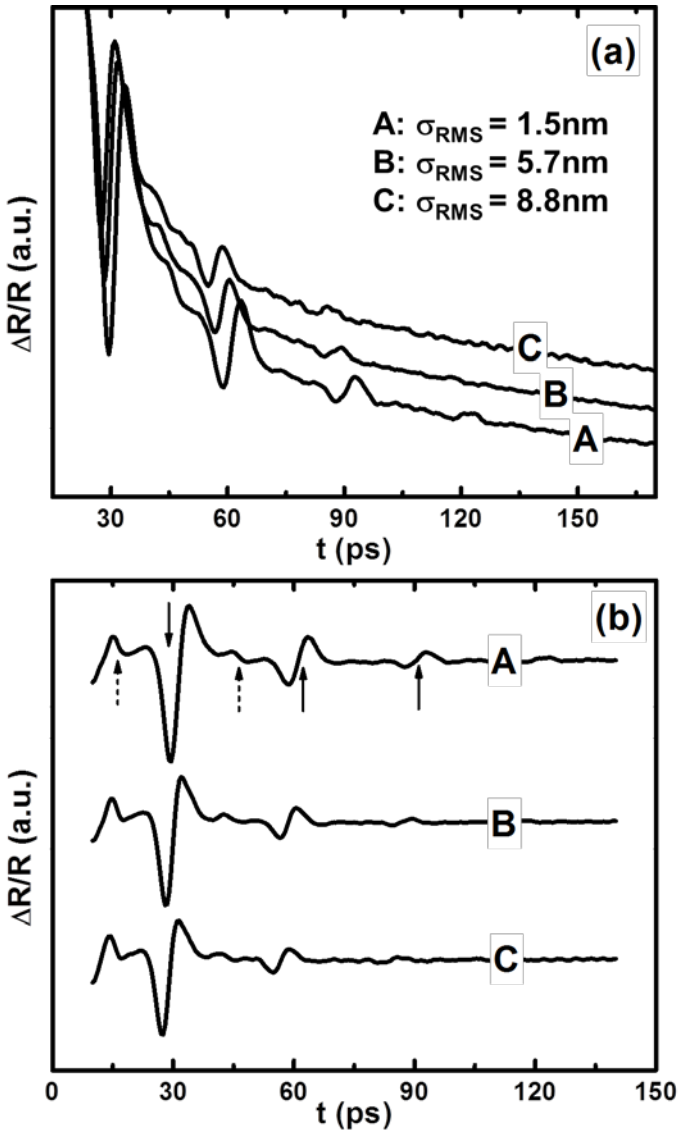

Figure 5-4 Pump-probe signals for Al/glass (a) with and (b) without thermal decay. The solid and dashed arrows in (b) label the positions of echoes from front-side and back-side excitations, respectively.

5.3 Results and discussion

We can obtain the acoustic reflection coefficient (r_{ac}) for different interface roughnesses (σ_{RMS}) by calculating the ratio of the amplitudes of the second and the first acoustic echoes. As shown in Figure 5-5, the errors bars are estimated through the deviations in r_{ac} and σ_{RMS} measured at various spots across the sample surfaces. As the

interface gets rougher, a significant reduction of acoustic reflection is observed. We perform a boundary perturbation calculation as developed in Chapter 4, assuming a dominant phonon wavelength of ~ 60 nm ($2\pi\zeta_{Al}$) [20,103]. The predicted values are apparently lower than the measurement, which suggests that other properties of the interface need to be considered. Due to the lack of data points in Figure 5-5, we turn to the frequency domain to better understand the interactions of acoustic phonons with the interface.

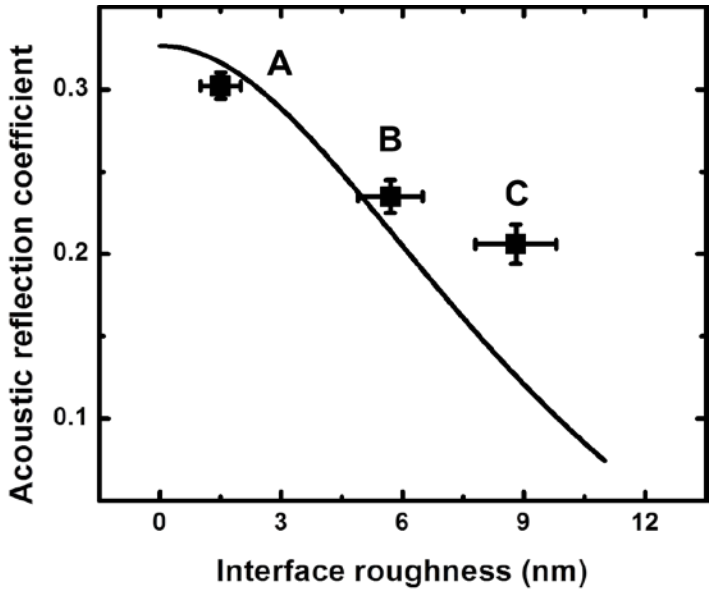

Figure 5-5 Measured (dots) coherent acoustic phonon reflection coefficient and calculated values (line) by the boundary perturbation method.

The initial acoustic strain pulse excited by the laser has spectral content described by [103]:

$$\eta(\omega) \sim \frac{\omega}{\omega^2 + (v/\zeta)^2} \tag{5.1}$$

Assuming a sound velocity v of 6420 m/s and a penetration depth ζ of ~ 10 nm for Al, this spectrum corresponds to a broad band with width up to ~ 200 GHz and a peak

frequency near 100 GHz. We perform a time-frequency analysis by taking the wavelet transforms of the acoustic transients and show the resulting contour plots in Figure 5-6. The high intensity (brightly colored) areas correspond to the first two acoustic echoes near ~ 30 ps and ~ 60 ps, respectively. The spectral range (20 – 200 GHz) and peak location agree well with the initial strain profile predicted by Equation (5.1).

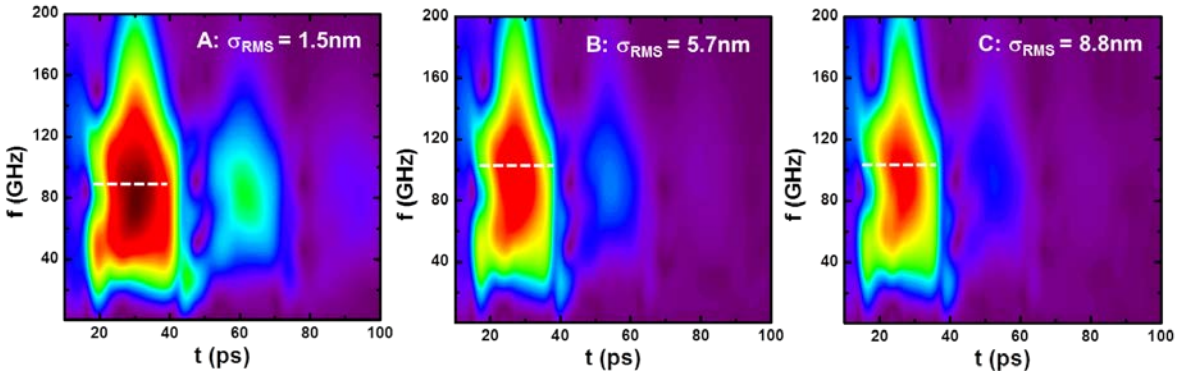

Figure 5-6 Wavelet transforms of acoustic transients of Samples A-C. The dashed white lines indicate the peak frequencies of the echoes.

These contours intuitively illustrate the lowering of coherent phonon energy during reflection at roughened interfaces (reduced intensity from A to C). For quantitative analysis we look at the FFT of each of the first two echoes by vertically slicing the wavelet transform data at the echo times, as shown in Figure 5-7 for Sample A.

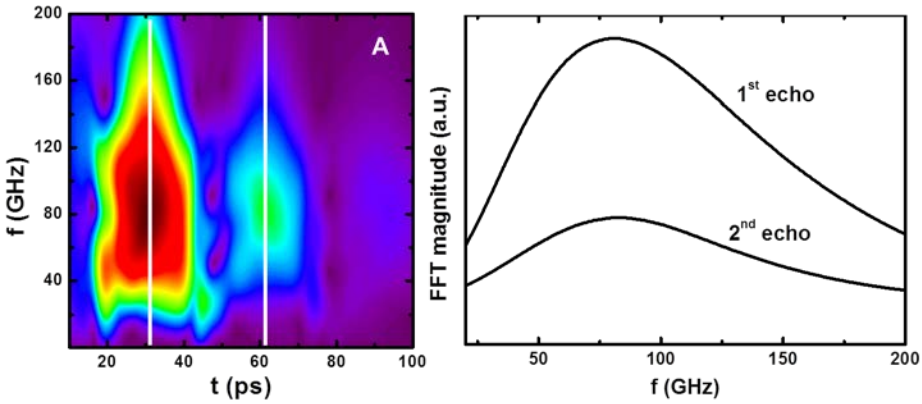

Figure 5-7 (left) Wavelet transform of the acoustic transients and (right) FFT of the first two echoes in Sample A.

The frequency-dependent acoustic reflection coefficient is thus obtained by deriving the two FFT magnitudes, and is plotted in Figure 5-8. Two observations seem unexpected by the perturbation analysis: (1) r_{ac} does not decrease monotonically with increasing frequency for each sample, and (2) the reduction in r_{ac} at high frequencies becomes less significant with roughened interfaces. These facts, together with the deviation in Figure 5-5, are preliminarily attributed to the possible decrease in interface stiffness (or bonding strength) when the interface gets rougher. Imperfect interface bonding (e. g., van der Waals bonding) is believed to act like a low-pass filter in reflecting a greater amount of high frequency phonons [61,68]. In this case, displacement continuity at the interface no longer holds, and a parameter representing interface strength needs to enter the boundary condition. We are in the process of developing a more comprehensive model to account for the effects of both interface roughness and interface stiffness.

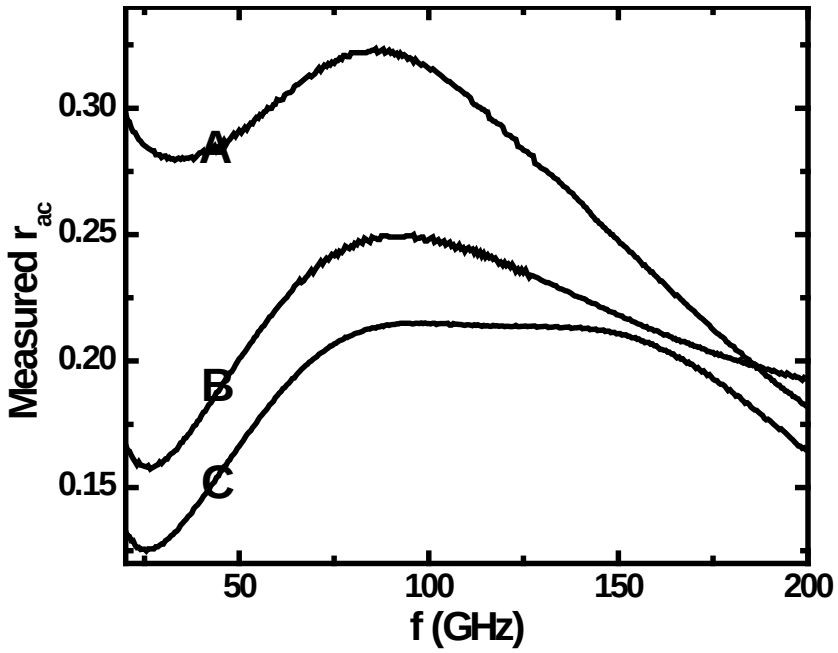

Figure 5-8 Acoustic reflection coefficient as a function of coherent phonon frequency for Samples A-C.

We note that there is a slight variation (up to ~ 6%) in the temporal location of the acoustic echoes between samples. Table 5-2 lists the time interval between echoes as well as the converted Al thickness. The 6% deviation cannot be explained by the positioning of samples during the thermal evaporation of Al, as all glass substrates are carefully placed with an equal lateral distance to the evaporation source. Therefore, we attribute this difference to the reduced sticking coefficient during deposition on a rougher glass surface. This lower sticking coefficient is also expected to relate to the lower interface stiffness for the rougher interface, as implied in Figure 5-8.

Glass sample	A	B	C
$t_{\text{round-trip}}$ (ps)	29.3	28.5	27.5
d_{Al} (nm)	93.9	91.5	88.3

Table 5-2 Round-trip times of acoustic strain pulse and corresponding Al thicknesses.

5.4 Conclusion

We have performed picosecond acoustics measurements to characterize coherent phonon reflection at smooth and roughened Al/glass interfaces. We have utilized the broadband acoustic pulse excited by an ultrafast laser to examine the frequency dependence of phonon transport at a rough interface. The deviations from model predictions indicate that additional features such as interface stiffness may play an important role in coherent and diffuse scattering.

CHAPTER 6

Concluding Remarks

6.1 Summary of present work

The present work aims to understand acoustic phonon transport in thin film nanostructures – in particular, at nanostructured interfaces. Such transport physics plays an important role in a variety of applications, including heat transfer and thermal management, terahertz phononic filters, and high frequency mechanical resonators.

Time-resolved optical pump-probe spectroscopy has been shown to be an effective tool for characterizing acoustic phonon transport in nanostructures. This technique, based on femtosecond lasers, is capable of probing ultrafast phonon and carrier dynamics at short spatial scales, which is difficult by other means. To achieve a wide and variable range of pump-probe time delay, we have utilized an asynchronous optical sampling system that phase-locks the pump and probe lasers with a slight frequency offset. The versatile ASOPS system enables fast scan and data acquisition without the use of a mechanical translation stage and a lock-in amplifier, eliminating alignment errors that often plague a conventional pump-probe setup.

We have developed a numerical model for transient thermoreflectance based on the ASOPS system, taking into account cumulative heating by multiple laser pulses. We have characterized the thermal transport properties of several semiconductor

structures with engineered interfaces, such as copper phthalocyanine (CuPc) thin films, GaAs:N nanocrystals, and Sb_2Te_3 nanostructures formed by laser irradiation. We have shown that nanocrystals or nanochannels formed on the surface of a material inhibit heat transfer by enhanced phonon boundary scattering.

Interfaces between very dissimilar materials have been an emerging subject of interest in numerous studies. An interface between a metal and an organic semiconductor is such an example, especially for phonon transport, as these two types of materials have tremendous differences in elastic modulus, acoustic impedance, and majority heat carrier type (electrons in metals and lattice vibrations in organics). These features have inspired us to construct a supported membrane resonator by inserting a compliant organic (CuPc) film at an Al/Si interface. We have used femtosecond laser pulses to excite multiple GHz coherent acoustic phonon modes in the resulting cavity and demonstrated that the interfacial CuPc film acts as an acoustic etalon to select certain modes out of the broadband excitation, which has scientific implications in understanding coherent acoustic phonon transport in heat conduction and Bragg reflection, as well as in designing high-frequency acoustic resonators.

Interface irregularities or imperfections are in general unavoidable due to material fabrication limits. Interface roughness can greatly influence acoustic phonon transport through scattering. We have developed a boundary perturbation approach to separate the specular and quasi-diffuse components of transmitted and reflected phonon waves. We have quantitatively analyzed the influence of interface roughness on the coupling of different phonon modes, the angular distribution of the quasi-diffuse field, and the excitation of interface evanescent waves. We have estimated the performance of a

coherent phonon reflector with roughened interfaces and proposed novel ideas for the design of such acoustic devices.

Experimental determination of phonon scattering properties has been challenging. We have artificially created interface roughness through chemical etching and have performed picosecond acoustics measurement on the resulting samples. Our data have shown a significant loss of acoustic phonons from their coherent states due to roughness. Frequency analysis has revealed interesting behavior of high frequency phonons that may require further understanding in the context of interface stiffness.

6.2 Suggestions for future work

6.2.1 Coherent mode control by multilayers

In Chapter 3 we have presented initial results of measured coherent confined phonon modes in a double bilayer structure (Figure 3-12). In another set of measurements, we vary the CuPc thickness between the two Al layers and plot FFT spectra of the corresponding acoustic transients in Figure 6-1. A comprehensive model for coherent phonon modes in multilayers is still needed to interpret the behavior illustrated in the figure.

In principle, by including multiple resonators and etalons in an engineered structure, we can achieve coherent control of the structure's acoustic phonon modes. This study will potentially be useful in the contexts of tunable high-frequency acoustic oscillators, stimulated emission of phonons, and acoustic mode switching.

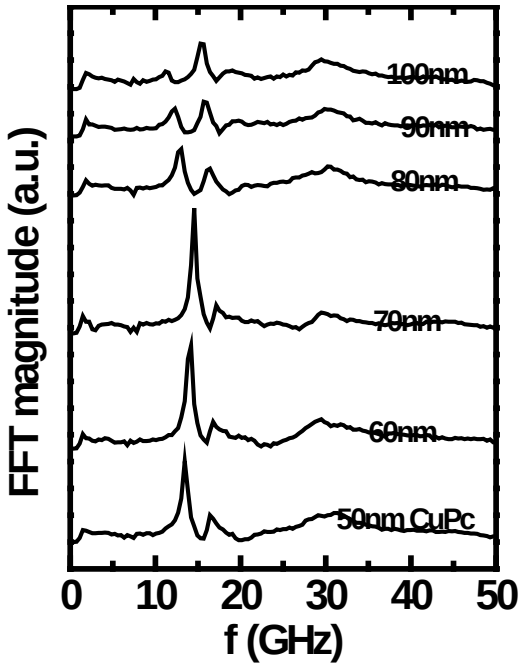

Figure 6-1 Fourier spectra of acoustic transients for samples with a structure of Al (220 nm)/CuPc (varied thickness as shown)/Al (200 nm)/CuPc (50 nm)/Si.

6.2.2 The effect of interface stiffness

In Chapter 5 we have proposed an additional scattering mechanism contributed by interface stiffness. When two materials are imperfectly bonded (e.g., by van der Waals forces), the interface stiffness cannot be considered infinite, and the displacement at the boundary is not continuous. We can approximate the displacement discontinuity by connecting the two materials with a massless spring [61,68]. The interface stiffness is simply the force constant K of the spring, with a unit of kg/m^2-s. The modified boundary condition is then given by:

$$K\left(u_1 - u_2\right)\Big|_{z=z_0} = \sigma_1\Big|_{z=z_0} = \sigma_2\Big|_{z=z_0} \tag{6.1}$$

wherein the stress remains continuous at the interface. Equation (6.1) can be adopted in the transfer matrix calculations presented in Chapters 1 and 4.

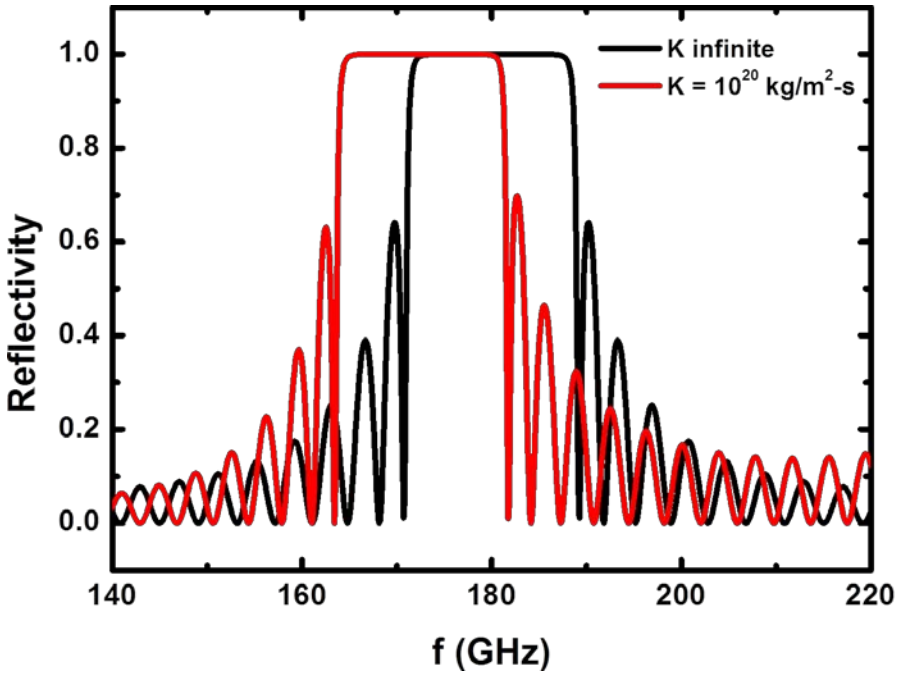

Figure 6-2 Calculated coherent phonon reflectivity of a 20-period Si/Ge superlattice at normal incidence with infinite interface stiffness (black) and finite (red) interface stiffness.

Figure 6-2 plots the coherent phonon reflectivity of a Si/Ge superlattice with different bonding strengths. The finite interface stiffness ($K = 10^{20}$ kg/m^2-s) red-shifts the reflection band to a great extent, and enhances the reflection for frequencies higher than the reflection band. We could potentially demonstrate this by performing picosecond acoustics on superlattices with van der Waals bonded interfaces (for example, metal/organic interfaces). This study would provide design guidelines for coherent phonon filters and enable new approaches for tunable devices.

Bibliography

[1] R. Chen, A. I. Hochbaum, P. Murphy, J. Moore, P. Yang, and A. Majumdar, *Phys. Rev. Lett.* **101**, 105501 (2008).

[2] J. A. Johnson, A. A. Maznev, J. Cuffe, J. K. Eliason, A. J. Minnich,Timothy Kehoe, C. M. Sotomayor Torres, G. Chen, and K. A. Nelson, *Phys. Rev. Lett.* **110**, 025901 (2008).

[3] R. M. Costescu, D. G. Cahill, F. H. Fabreguette, Z. A. Sechrist, and S. M. George, *Science* **303**, 989 (2004).

[4] C. Chiritescu, D. G. Cahill, N. Nguyen, D. Johnson, A. Bodapati, P. Keblinski, and P. Zschack, *Science* **315**, 351 (2007).

[5] G. Pernot, M. Stoffel, I. Savic, F. Pezzoli, P. Chen, G. Savelli, A. Jacquot, J. Schumann, U. Denker, I. Mönch, Ch. Deneke, O. G. Schmidt, J. M. Rampnoux, S.Wang, M. Plissonnier, A. Rastelli, S. Dilhaire, and N. Mingo, *Nat. Mater.* **9**, 491 (2010).

[6] M. N. Luckyanova, J. Garg, K. Esfarjani, A. Jandl, M. T. Bulsara, A. J. Schmidt, A. J. Minnich, S. Chen, M. S. Dresselhaus, Z. Ren, E. A. Fitzgerald, and G. Chen, *Science* **338**, 936 (2012).

[7] S. Tamura, D. C. Hurley, and J. P. Wolfe, *Phys. Rev. B* **38**, 1427 (1988).

[8] M. Maldovan, *Phys. Rev. Lett.* **110**, 025902 (2013).

[9] V. Narayanamurti, H. L. Störmer, M. A. Chin, A. C. Gossard, and W. Wiegmann, *Phys. Rev. Lett.* **43**, 2012 (1979).

[10] D. C. Hurley, S. Tamura, J. P. Wolfe, and H. Morkoc, *Phys. Rev. Lett.* **58**, 2446 (1987).

[11] O. Koblinger, J. Mebert, E. Dittrich, S. Döttinger, W. Eisenmenger, P. V. Santos, and L. Ley, *Phys. Rev. B(R)* **35**, 9372 (1987).

[12] P. V. Santos, L. Ley, J. Mebert, and O. Koblinger, *Phys. Rev. B* **36**, 1306 (R) (1987).

[13] N. D. Lanzillotti-Kimura, B. Perrin, A. Fainstein, B. Jusserand, and A. Lemaître, *Appl. Phys. Lett.* **96**, 053101 (2010).

[14] Y. Ezzahri, S. Grauby, J. M. Rampnoux, H. Michel, G. Pernot, W. Claeys, S. Dilhaire, C. Rossignol, G. Zeng, and A. Shakouri, *Phys. Rev. B* **75**, 195309 (2007).

[15] John Berge and Spartak Gevorgian, *IEEE Trans. Ultrason. Ferroelectr. Freq. Control* **58**, 2768 (2011).

[16] A. Müller, D. Neculoiu, G. Konstantinidis, A. Stavrinidis, D. Vasilache, A. Cismaru, M. Danila, M. Dragoman, G. Deligeorgis, and K. Tsagaraki, *IEEE Electron Device Lett.* **30**, 799 (2009).

[17] B. A. Auld, *Acoustic Fields and Waves in Solids* (Krieger, FL, 1990), Vol. II.

[18] G. Chen, *Nanoscale Energy Transport and Conversion* (Oxford, 2005).

[19] E. T. Swartz and R. O. Pohl, *Rev. Mod. Phys.* **61**, 605 (1989).

[20] O. B. Wright and V. E. Gusev, *IEEE Trans. Ultrason. Ferroelectr. Freq. Control* **42**, 331 (1995).

[21] G. Tas and H. J. Maris, *Phys. Rev. B* **49**, 15046 (1994).

[22] R. J. Stevens, A. N. Smith, P. M. Norris, *J. Heat Transfer* **127**, 315 (2005).

[23] W. S. Capinski and H. J. Maris, *Rev. Sci. Instrum.* **67**, 2720 (1996).

[24] R.M. Cotescu, M.A. Wall, and D.G. Cahill, *Phys. Rev. B* **67**, 054302 (2003).

[25] D.G. Cahill, *Rev. Sci. Instrum*. **75**, 5119 (2004).

[26] A. Bartels, R. Cerna, C. Kistner, A. Thoma, F. Hudert, C. Janke, and T. Dekorsy, *Rev. Sci. Instrum*. **78**, 035107 (2007).

[27] V. A. Stoica, Y.-M. Sheu, D. A. Reis, and R. Clarke, *Opt. Express* **16**, 2323 (2008).

[28] C. Thomsen, H. T. Grahn, H. J. Maris, and J. Tauc, *Phys. Rev. B* **34**, 4129 (1986).

[29] B. Perrin, *Microscale and Nanoscale Heat Transfer*, topics in Applied Physics, S. Voltz, ed., (Springer, Berlin, 2007), **107**, 333.

[30] P. Reddy, K. Castelino, and A. Majumdar, *Appl. Phys. Lett.* **87**, 211908 (2005).

[31] G. Nenna, G. Flaminio, T. Fasolino, C. Minarini, R. Miscioscia, D. Palumbo, and M. Pellegrino, *Macromol. Symp.* **247**, 326 (2007).

[32] V.I. Adamovich, M.S. Weaver, R.C. Kwong, J. J. Brown, *Curr. Appl. Phys.* **5**, 15 (2005).

[33] Roland Steim, Stelios A. Choulis, Pavel Schilinsky, Uli Lemmer, and Christoph J. Brabec, *Appl. Phys. Lett.* **94**, 043304 (2009).

[34] Y. Jin, A. Yadav, K. Sun, H. Sun, K. P. Pipe, and M. Shtein, *Appl. Phys. Lett.* **98**, 093305 (2011).

[35] David G. Cahill, and R. O. Pohl, *Phys. Rev. B* **35**, 4067 (1987).

[36] David G. Cahill, *Rev. Sci. Instrum.* **61**, 802 (1990).

[37] M. J. Assael, S. Botsios, K. Gialou, and I. N. Metaxa, *International Journal of Thermophysics* **26**, 1595 (2005).

[38] N. Kim, B. Domercq, S. Yoo, A. Christensen, B. Kippelen, and S. Grahama, *Appl. Phys. Lett.* **87**, 241908 (2005).

[39] C. L. Choy, Y. W. Wong, G. W. Yang, and T. Kanamto, *Journal of Polymer Science: Part B: Polymer Physics* **37**, 3359 (1999).

[40] A. W. Wood, J. C. Canniff, H. Sun, Y. Q. Wang, K. P. Pipe, and R. S. Goldman, *International Conference on Thermoelectrics*, Traverse City, MI, July 2011.

[41] Y. Li, V. A. Stoica, L. Endicott, G. Wang, H. Sun, K. P. Pipe, C. Uher, and R. Clarke, *Appl. Phys. Lett.* **99**, 121903 (2011).

[42] A. Borowiec and H. K. Haugen, *Appl. Phys. Lett.* **82**, 4462 (2003).

[43] Y. Shimotsuma, P. G. Kazansky, J. Qiu, and K. Hirao, *Phys. Rev. Lett.* **91**, 247405 (2003).

[44] M. Huang, F. Zhao, Y. Cheng, N. Xu, and Z. Xu, *Phys. Rev. B* **79**, 125436 (2009).

[45] Y. Li, V. A. Stoica, L. Endicott, G. Wang, H. Sun, K. P. Pipe, C. Uher, and R. Clarke, *Mat. Res. Soc. Symp. Proc.* **1456**, 177 (2012).

[46] H. Sun, V. A. Stoica, M. Shtein, R. Clarke, and K. P. Pipe, *Phys. Rev. Lett.* **110**, 086109 (2013).

[47] T. Carmon and K. J. Vahala, *Phys. Rev. Lett.* **98**, 123901 (2007).

[48] S. Gröblacher, K. Hammerer, M. R. Vanner, and M. Aspelmeyer, *Nature* **460**, 724 (2009).

[49] V. Juvé, A. Crut, P. Maioli, M. Pellarin, M. Broyer, N. D. Fatti, and F. Vallée, *Nano Lett.* **10**, 1853 (2010).

[50] T. A. Kelf, Y. Tanaka, O. Matsuda, E. M. Larsson, D. S. Sutherland, and O. B. Wright, *Nano Lett.* **11**, 3893 (2011).

[51] D. H. Hurley, R. Lewis, O. B. Wright, and O. Matsuda, *Appl. Phys. Lett.* **93**, 113101 (2008).

[52] C.-K. Sun, Y.-K. Huang, J.-C. Liang, A. Abare, and S. P. DenBaars, *Appl. Phys. Lett.* **78**, 1201 (2001).

[53] G. S. Wiederhecker, A. Brenn, H. L. Fragnito, and P. St. J. Russell, *Phys. Rev. Lett.* **100**, 203903 (2008).

[54] Y. Li, Q. Miao, A. V. Nurmikko, and H. J. Maris, *J. Appl. Phys.* **105**, 083516 (2009).

[55] N. D. Lanzillotti-Kimura, A. Fainstein, A. Huynh, B. Perrin, B. Jusserand, A. Miard, and A. Lemaître, *Phys. Rev. Lett.* **99**, 217405 (2007).

[56] N. D. Lanzillotti-Kimura, A. Fainstein, B. Perrin, B. Jusserand, A. Soukiassian, X. X. Xi, and D. G. Schlom, *Phys. Rev. Lett.* **104**, 187402 (2010).

[57] F. Hudert, A. Bruchhausen, D. Issenmann, O. Schecker, R. Waitz, A. Erbe, E. Scheer, T. Dekorsy, A. Mlayah, and J.-R. Huntzinger, *Phys. Rev. B* **79**, 201307 (R) (2009).

[58] A. Bruchhausen, R. Gebs, F. Hudert, D. Issenmann, G. Klatt, A. Bartels, O. Schecker, R. Waitz, A. Erbe, E. Scheer, J.-R. Huntzinger, A. Mlayah, and T. Dekorsy, *Phys. Rev. Lett.* **106**, 077401 (2011).

[59] P. W. Smith, *Proc. IEEE* **60**, 422 (1972).

[60] W. Koechner, *Solid-State Laser Engineering* (Springer, New York, 2006), 6th ed.

[61] G. A. Antonelli, B. Perrin, B. C. Daly, and D. G. Cahill, *Mater. Res. Soc. Bull.* **31**, 607 (2006).

[62] M. Hettich, A. Bruchhausen, S. Riedel, T. Geldhauser, S. Verleger, D. Issenmann, O. Ristow, R. Chauhan, J. Dual, A. Erbe, E. Scheer, P. Leiderer, and T. Dekorsy, *Appl. Phys. Lett.* **98**, 261908 (2011).

[63] A. V. Akimov, E. S. K. Young, J. S. Sharp, V. Gusev, and A. J. Kent, *Appl. Phys. Lett.* **99**, 021912 (2011).

[64] B. C. Daly, K. Kang, Y. Wang, and D. G. Cahill, *Phys. Rev. B* **80**, 174112 (2009).

[65] C. Mechri, P. Ruello, and V. Gusev, *New J. Phys.* **14**, 023048 (2012).

[66] B. Bonello, G. Louis, and P. Battioni, *Rev. Sci. Instrum.* **74**, 889 (2003).

[67] H. Ogi, M. Fujii, N. Nakamura, T. Yasui, and M. Hirao, *Phys. Rev. Lett.* **98**, 195503 (2007).

[68] G. Tas, J. J. Loomis, H. J. Maris, A. A. Bailes III, and L. E. Seiberling, *Appl. Phys. Lett.* **72**, 2235 (1998).

[69] Jessica M. Torres, Nathan Bakken, Christopher M. Stafford, Jian Li, and Bryan D. Vogt, *Soft Matter* **6**,5783 (2010).

[70] P. A. O'Connell and G. B. McKenna, *Eur. Phys. J. E* **20**, 143 (2006).

[71] J. Groenen, F. Poinsotte, A. Zwick, C. M. Sotomayor Torres, M. Prunnila, and J. Ahopelto, *Phys. Rev. B* **77**, 045420 (2008).

[72] C. J. Morath and H. J. Maris, *Phys. Rev. B* **54**, 203 (1996).

[73] D. Givoli and J. B. Keller, *Wave Motion* **12**, 261 (1990).

[74] N. M. Stanton, R. N. Kini, A. J. Kent, M. Henini, and D. Lehmann, *Phys. Rev. B* **68**, 113302 (2003).

[75] A. Bartels, T. Dekorsy, H. Kurz, and K. Köhler, *Phys. Rev. Lett.* **82**, 1044 (1999).

[76] R. Venkatasubramanian, *Phys. Rev. B* **61**, 3091 (2000).

[77] M. N. Touzelbaev, P. Zhou, R. Venkatasubramanian and K. E. Goodson, *J. Appl. Phys.* **90**, 763 (2001).

[78] S.-M. Lee, David G. Cahill and R. Venkatasubramanian, *Appl. Phys. Lett.* **70**, 2957 (1997).

[79] I. Filinski, Phys. *Status Solidi B* **49**, 577 (1972).

[80] S. A. Stepanov, E. A. Kondrashkina, M. Schmidbauer, R. Köhler, J.-U. Pfeiffer, T. Jach, and A. Yu. Souvorov, *Phys. Rev. B* **54**, 8150 (1996).

[81] J. M. Ziman, *Electrons and Phonons* (Oxford, 1960).

[82] G. Chen, *Phys. Rev. B* **57**, 14958 (1998).

[83] P. M. Norris and P. E. Hopkins, *J. Heat Transfer* **131**, 043207 (2009).

[84] A. Majumdar, *J. Heat Transfer* **113**, 797 (1991).

[85] B. C. Daly, H. J. Maris, K. Imamura and S. Tamura, *Phys. Rev. B* **66**, 024301 (2002).

[86] H. Zhao and J. B. Freund, *J. Appl. Phys.* **105**, 013515 (2009).

[87] A. D. Lapin, *Sov. Phys. Acoust.* **15**, 336 (1970).

[88] N. S. Shiren, *Phys. Rev. Lett.* **47**, 1466 (1981).

[89] W. A. Kuperman, H. Schmidt, *J. Acoust. Soc. Am.* **86**, 1511 (1989).

[90] H. Sun and K. P. Pipe, *J. Appl. Phys.* **111**, 023510 (2012).

[91] S. Tamura, Y. Tanaka, and H. J. Maris, *Phys. Rev. B* **60**, 2627 (1999).

[92] B. A. Auld, *Acoustic Fields and Waves in Solids* (Krieger, FL, 1990), Vol. I.

[93] C.-L. Hsieh, K-H. Lin, S.-B. Wu, C.-C. Pan, J.-I. Chyi, and C.-K. Sun, *Appl. Phys. Lett.* **85**, 4735 (2004).

[94] W. L. Pilant, *Bull. Seism. Soc. Am.* **62**, 285 (1972).

[95] R. E. Peterson and A. C. Anderson, *J. Low. Temp. Phys.* **11**, 639 (1973).

[96] A. Soukiassian, W. Tian, D. A. Tenne, X. X. Xi, D. G. Schlom, N. D. Lanzillotti-Kimura, A. Bruchhausen, A. Fainstein, H. P. Sun, X. Q. Pan, A. Cros, and A. Cantarero, *Appl. Phys. Lett.* **90**, 042909 (2007).

[97] H. Kamioka, *Jpn. J. Appl. Phys.* **26**, 1925 (2010).

[98] G. A. Northrop and J. P. Wolfe, *Phys. Rev. Lett.* **52**, 2156 (1984).

[99] J. Weber et al., *Phys. Rev. Lett.* **40**, 1469 (1978).

[100] P. Taborek and D. L. Goodstein, *Phys. Rev. B* **22**, 1550 (1980).

[101] Y.-C. Wen, C.-L. Hsieh, K.-H. Lin, H.-P. Chen, S.-C. Chin, C.-L. Hsiao, Y.-T. Lin, C.-S. Chang, Y.-C. Chang, L.-W. Tu, and C.-K. Sun, *Phys. Rev. Lett.* **103**, 264301 (2009).

[102] S. L. Broschat and E. I. Thorsos, *J. Acoust. Soc. Am.* **101**, 2615 (1997).

[103] H. T. Grahn, H. J. Maris, and J. Tauc, *IEEE J. Quant. Electron.* **25**, 2562 (1989).